EFFECTS OF ISOSTASY ON LARGE-SCALE GEOID SIGNAL

by

Abraham Hofstetter

A dissertation submitted in partial fulfillment

of the requirements for the degree of

Doctor of Philosophy

University of Washington

1987

Approved by _____

(Chairperson of Supervisory Committee)

Program Authorized

to Offer Degree_____Geophysics Program_____

Date_____December 18, 1986_____

Doctoral Dissertation

Signature

_____

Date_____

University of Washington

Abstract

EFFECTS OF ISOSTASY ON LARGE-SCALE GEOID SIGNAL

By Abraham Hofstetter

Chairperson of the Supervisory Committee: Prof. Clive R. B. Lister
Geophysics Program

The geoid anomaly due to the cooling lithosphere is a second-order quantity which is sensitive to the definition of isostasy. We use a combination of Pratt's and Airy's isostatic model which consists of continental or oceanic lithospheres underlain by asthenosphere. On a test planet for the method, there are two ocean ridges along 0° and 180° longitudes and two trenches along 90° and 270° longitudes. The oceanic plates are moving away from the ridge with a velocity of 5cm/yr at the equator. Pressure is assumed constant at the compensation depth, which is itself an equipotential surface. We use the method of rings, in which a set of 18 rings about an arbitrary pole (observation point) cover the whole earth. This method allows the anomaly source depth to be taken into account. Changes in the geoidal surface height both above and below any one ring induce mass changes due to infilling with seawater and mantle material, respectively.

These mass changes cause further changes in the geoidal height over and below all the other rings, and the interaction can be solved by linear simultaneous equations. The final geoid is a product of seven second-order effects. The direct dipole effect due to density differences in the cooling lithosphere (Lister, 1982) produces a geoidal elevation of up to 11m and -11m over the ridge and the trench, respectively. The direct mass effect (Vening Meinesz, 1946), due to the fact that a column on a sphere is pie-shaped, produces a geoidal elevation of up to 12m and -11m over the ridge and the trench, respectively. The final geoidal elevation, due to the direct and indirect effects, is up to 26m and -26m over the ridge and the trench, respectively, because the dipole and the mass effects tend to cancel each other at the reference surface.

The earth's surface is divided into 36x18 spherical trapezoids (10°x10°), and age or topographic height is assigned to each trapezoid containing oceanic lithosphere or continent, respectively. Over most of the earth, the direct dipole effect is dominant relative to the direct mass effect. The lithospheric geoid is poorly correlated with the observed geoid due to large and deep mantle mass anomalies.

TABLE OF CONTENTS

LIST OF FIGURES

ACKNOWLEDGMENTS

I consider myself fortunate to have the opportunity to interact with Prof. Clive Lister. His stimulating and challenging ideas deepened my interest in the field of gravitational potential and plate tectonics. I wish to thank him for sharing his knowledge and experience with me, and for helping and assisting me through the project.

Many heart-felt thanks to my wife Gaby, who supported, encouraged, and stuck by me through the long process of graduate school of hardship. She never failed to be with me whenever I needed her. Thank you Gaby.

I wish to express my sincere gratitude to my parents who backed me up, cared about, and supported me professionally and morally since my early start at school long time ago. I deeply regret that my mother is no longer here to share this moment with me. I thank all the members of my family (including all the in-laws) who encouraged me and crossed their fingers wishing me luck all those years.

I wish to thank the members of my committee, Professors J. Booker, B. Lewis, and A. Schultz for helpful discussions and comments through various steps of this project. Special thanks to Prof. B. Lewis for providing the computing facilities, which are needed very much in this

To my wife Gaby

CHAPTER ONE - INTRODUCTION

1. OVERVIEW OF PLATE TECTONICS

A major breakthrough in understanding of global geophysical and geological processes of the earth occurred during the 1960's when the "Plate Tectonics" theory became generally accepted. Plate tectonics is a model in which the outermost shell of the earth is divided into a number of thin, rigid plates, each moving as a distinct unit. The plates are in motion with respect to one another, with relative velocities of the order of a few tens of millimeters per year. Most volcanic eruptions, earthquakes, and mountain building events occur near plate boundaries. Many studies have established this new idea, and here we mention just a few classic early papers: Benioff (1954), Dietz (1961), Vine and Matthews (1963), Bullard (1964), Bullard et al. (1965), Wilson (1965), Sykes (1966), Oliver and Isacks (1967), Sykes (1967), Heirtzler et al. (1968), LePichon (1968), Oxburgh and Turcotte (1968), Isacks et al. (1968), Vine (1968), Cox (1969), Dewey and Bird (1970), and Kaula (1970).

The surface of the earth is composed of ocean basins and continents. Some parts of the continents are older than 10^9 years; the oldest part is about 3.8×10^9 years. The continent is gravitationally

stable because it is slightly lighter than the mantle beneath it, with a thickness of up to about 70 km. At present continental basement cratons are not being added to, which means that our knowledge of the creation process is very limited.

The oldest part of the ocean is about 200 my old. Oceanic plates are comprised of relatively cool rocks with an average elastic thickness of about 100 km. This thin shell or skin is called the oceanic lithosphere, and it is underlain by a hotter asthenosphere. Both the oceanic and the continental lithospheres are considered rigid because they are cool; as a result the interiors of the plates do not deform significantly as they move about the surface of the earth. On the other hand, the asthenosphere is considered to be hot enough to be able to deform freely; therefore the lithosphere "rides" over the asthenosphere with little resistance.

Plates are continually created and consumed. The spreading lithosphere is formed at an oceanic ridge, a divergent plate boundary, where hot material from underneath ascends to fill the gap created as two or more plates move apart. As the molten rock cools, it becomes rigid and adds new area to an existing plate. This whole process is known as seafloor spreading. Conversely, a complementary process of plate consumption must exist, since the surface area of the earth remains essentially constant. This process, called subduction, occurs at ocean trenches, where two adjacent plates converge, and one plate bends and descends beneath the other into the interior of the earth. Pressure increases with depth and the subducting plate goes through phase transformations at depths similar to those of the surrounding

rocks, whose transition zones are at 420 and 670 km. The phase transformations cause rearrangement of the minerals in more condensed form which results in density change. Between the trench and the ridge there must be a return flow within the mantle, driven by a pressure difference. It is the effect of this mantle flow on the geoid that we hoped to detect.

Away from the ridge axis the rocks of the lithosphere are older and cooler than those close to the ridge. Thermal contraction increases rock density, which causes the cooling lithosphere to subside to deeper levels as it moves away from the ridge axis. Eventually, the lithosphere, gravitationally unstable with respect to the hot asthenosphere beneath, bends and sinks into the asthenosphere because of negative buoyancy.

This general description of plate tectonics is now widely accepted in the scientific community, but there are two main models which attempt to calculate various parameters in the lithosphere, such as seafloor topography and thermal conditions. The first is the "simple plate" model, in which the temperature is assumed to be fixed at a depth on the order of 100 km (Langseth et al., 1966; McKenzie, 1967; Sclater and Francheteau, 1970; Sclater et al., 1975). The new lithosphere is created at the ridge at the same temperature as the bottom boundary. The thickness of the lithosphere is constant and only at some fixed age do the heat flow and depth decrease asymptotically to some constant value. No obvious mechanism is suggested that would maintain the constant temperature at the bottom of the lithosphere, which makes this model somewhat unrealistic. The "simple boundary

layer" is an alternative model, in which the upper mantle cools by conduction and the thickness of the lithosphere increases as the square root of the age (Parker and Oldenburg, 1973). Davis and Lister (1974) used a similar model to show that the seafloor topography increases as the square root of the age. The agreement between this model and observations of depth versus age is remarkably good, up to an age of 100 my.

Both models predict similar behavior of heat flow and geoid height for young lithosphere; they differ, however, for ages of more than 100 my, i.e. when cooling has penetrated through all or most of the lithosphere. At present, the controversial issue is whether the deviation of seafloor topography from those values predicted by the boundary layer model, using the square root of age, is caused by the appearance of a bottom temperature boundary or by reheating within the lithospheric plate. Parsons and Sclater (1977) extended the empirical age-depth relation for ages of 0 my to 80 my (Sclater et al., 1971, 1975) to ages of 0 my to 160 my. They showed that seafloor topography exponentially approaches a depth of 6400 m, rather than following a linear relationship between depth and square root of age as was observed for young (<80 my) lithosphere (Davis and Lister, 1974). Their conclusion is that the thermal evolution of the lithosphere is best described by the simple plate concept. For the north Pacific the curve of depth versus age predicted by the plate model, except for ages of 110 my to 130 my and greater than 160 my, lies closer to the observed values than that of the boundary layer model (Renkin and Sclater, 1986). Subtraction of the predicted plate model depths from

the observed depths creates a small ramp in the residual depths. In the north Pacific, the ocean floor is generally deeper than predicted values for the young eastern side of the Pacific and shallower for the western side of the Pacific, respectively. On the other hand, other models attempt to explain the flattening of the seafloor by proposing a reheating of the lithosphere: one claims that heat is supplied by radioactive decay of elements in the lithosphere (Forsyth, 1977); others suggest that heat is supplied to the bottom of the lithosphere from shear heating in the asthenosphere (Schubert et al., 1976), or by small scale convection (Richter and Parsons, 1975; Parsons and McKenzie, 1978); still another is that frictional heat is generated, by shallow return flow in the asthenosphere (Schubert et al., 1978). Good candidates for causing seafloor flattening by internal reheating are the volcanic hot spots (Crough, 1978; Heestand and Crough, 1981), which cause anomalously shallow swells, such as in the Hawaiian islands, Bermuda, and Cape Verde.

Thermally-driven convection in the mantle is considered to be the prime cause of plate motions (Langseth et al., 1966; Vine, 1966; Isacks et al., 1968; McKenzie, 1969; Dewey and Bird, 1970; Forsyth, 1977; and many others). However, the geometry and mechanism of the thermal convection is controversial. One can define two main schools of thought. Whole mantle convection has been advocated by Davies (1977, 1984), Elsasser et al. (1979), and Kenyon and Turcotte (1983) who argue that the rise of viscosity with depth is too small to confine convection to shallow depths, and that the entire mantle is roughly uniform since the mean atomic weight is almost constant. In

addition, recent observations of very deep earthquakes of at least 900-1000 km (only at Kuril trench; Jordan, 1977; Creager and Jordan, 1984) suggest that the subducting plate penetrates the 670 km discontinuity of seismic velocity that is generally considered to indicate the boundary between the upper and lower mantle.

The second school of thought separates the mantle into two convection systems, the upper mantle cell and the lower mantle cell (Richter, 1973, 1978; Richter and Parsons, 1975; Busse, 1981, 1983; Peltier, 1985). In this model the plates are driven by upper mantle convection, and the 670 km discontinuity delineates a barrier to deeper penetration by subducting plates; therefore it is a constraint on the scale of mantle convection. Common supports of this model are: chemical stratification and geochemical budget models, the existence of dominant mass heterogeneities in the mantle, which have been attributed to the transition zone from 420 to 670 km depth, and the lack of seismicity below 670 km (Anderson, 1979; Jacobsen and Wasserburg, 1980; Richter and McKenzie, 1981; Masters et al., 1982; Woodhouse and Dziewonski, 1984; Jarvis and Peltier, 1986).

So far, we have given a general description of plate tectonics. At present, we cannot directly measure different parameters within the lithosphere or the asthenosphere, such as temperature and density, and we have to use indirect methods in order to gain better understanding. One important approach is the interpretation of gravity and geoid data, as for years many studies attempted to find a correlation between observed geoid and mantle flow, or with seafloor and continental topography. In the next sections, we focus our attention

on the geoid, beginning with a short historical background, and then building a model that describes the geoid over the earth.

2. GRAVITY, GEOID AND THE SHAPE OF THE EARTH

It is a well known fact that a body released close to the earth's surface falls vertically down with an increasing velocity. In the early seventeenth century in a pioneering study, Galileo showed that this rate of change, or the acceleration of gravity, is the same for all bodies at a given point on earth. Newton later formulated the phenomenon of mutual attraction of all masses, using deductions from Kepler's laws on the planets' motions; gravitational acceleration can be viewed as a special case of the universal attraction.

In the case of the earth, the force of attraction is dependent on the earth's mass, the mass of the body, and the distance between their centers. If the earth were a uniform, ideal sphere, a homogeneous and non-rotating planet, then the gravitational acceleration would be the same everywhere at a given distance. In fact, the opposite is true: the acceleration of gravity varies from one place to another, which indicates the presence of anomalous conditions within the earth. It is the aim of geophysics to measure and interpret these variations. Analysis of these gravity anomalies, using physical methods, is a powerful tool for gaining a better insight into the earth's interior.

We define the potential field, at a given point, as the work needed to bring a unit mass from infinity to that point. It is often convenient to describe the gravitational field using the potential, as it is a scalar quantity, in contrast to the attraction force, which is a vector. Thus, the gravitational field can be easily described by surfaces over which the potential is constant, known as equipotential surfaces, and the force vector is everywhere normal to these surfaces. The actual (observed) sea level is an approximate equipotential surface, known as the geoid, on which the gravitational potential is everywhere constant, since the water surface follows an equipotential, except for minor oceanographic effects (e.g. tides, currents, and water masses of varying density). The geoid is a closed and complete surface which corresponds closely to mean sea level over the oceans, and with extension of the same equipotential beneath the continents.

If we allow only radial variations of density in the earth and remove all local irregularities, the residuum is a spheroid, a mathematical figure that represents an ideal equipotential surface. In such a model of the planet, the sea-level varies smoothly from the poles to the equator. Lateral density nonhomogeneities make the real situation much more complicated, because each mass excess (or deficiency) causes warping of the equipotential surface, or geoid, from the spheroid shape (see Figure 1).

Stokes (1849) showed that if there is no mass external to the geoid and g is everywhere known on the geoid, then for a single mass anomaly in a uniform field the warping of the geoid (AB in Figure 1)

Figure 1.   Geoid undulations caused by a mass anomaly.
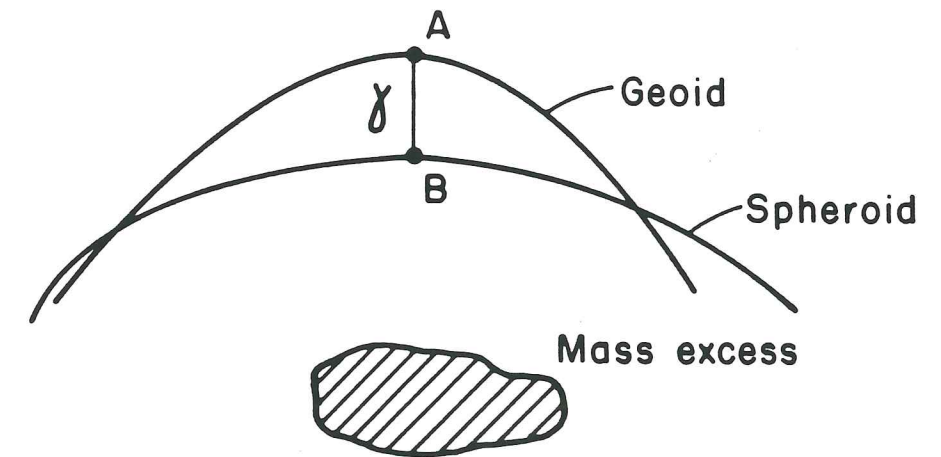
is given by $g\gamma=\Delta U$, where γ is the geoid anomaly, g is the mean value of gravity between A and B, and ΔU is the additional potential. Stokes (1849) also obtained a formula for the geoid when there is an extended region of anomalous mass.

Gravity measurements everywhere are reduced to the geoid and not to the spheroid, so that we need a correction to transfer to the latter. This correction is known as the "indirect effect" (Lambert, 1930; Lambert and Darling, 1936; Chapman and Bodine, 1979). As this is a distortion of the spheroid, a more appropriate name for the gravity observations is the "free geoid anomaly" (Lister, 1982).

3. ISOSTASY

Stability and buoyancy of mountains were discussed as early as the seventeenth century, when it was suggested that mountains "float" or stand up because of the presence of lighter material below. Major conceptual breakthroughs were achieved by Pratt (1855), who calculated the vertical deflection of gravitational acceleration, g, in the vicinity of the Himalayas, and by Airy (1855), who interpreted these computations as a proof of compensation of mountain masses. Airy postulated the existence of a root beneath an elevated area, so the total mass per unit area down to a depth defined as the "compensation" surface is everywhere the same (see Figure 2). Airy "divided" the mountain into two uniform blocks which were, relative to the ambient

Figure 2. Airy's (A) and Pratt's (B) isostatic model.
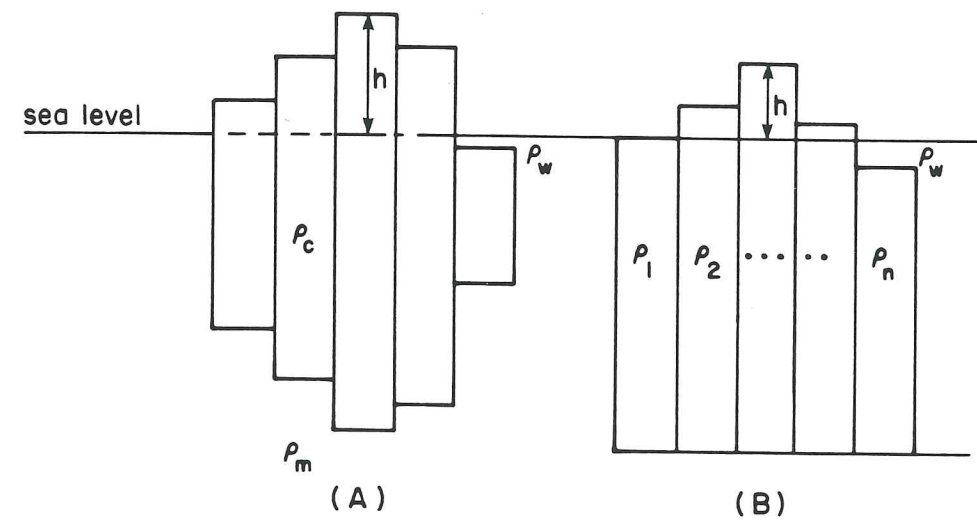
material, denser above and less dense below. Airy also proposed the dipole effect, that close to mountains or elevated areas one gets a positive gravitational attraction, and that below the horizon of the dipole equator there is a diminution of attraction, or negative attraction (this concept was later rigorously developed by Lister in 1982). The difference in the attraction is proportional to the difference of the inverse cube of the distance of the observation point from the center of the two masses. Pratt (1859a, b) agreed with the idea of compensation and that the mass in each column is the same, but disagreed with the mechanism, proposing a different model in which the compensation level occurs at a uniform depth, and the density varies inversely as the topography height (see Figure 2).

It was Dutton (1889) who introduced the term "isostasy" for the first time to describe the compensation condition and a state of hydrostatic stress at some depth in the earth. Airy's and Pratt's models were tested later in order to find the best parameters that minimize the gravity anomaly, such as the density and compensation depth (Hayford and Bowie, 1912; Lambert, 1930; Heiskanen, 1938; Heiskanen and Vening Meinesz, 1958).

It is convenient to think of continents as blocks floating on a "sea of reference rock". As the lithosphere is unable to resist a large vertical shear stress (i.e., to support a substantial accumulation of mass), these blocks may rise or sink in the asthenosphere. The principle of isostasy states that there is a surface in the asthenosphere, that is called the compensation depth surface, on which any vertical column of mass between the surface and

the compensation depth produces the same pressure. The earth is asymmetric and nonhomogeneous, and in order to maintain isostatic equilibrium, on geological times scale, some blocks rise and some sink. This causes a distortion of the earth's surface.

4. RECENT STUDIES OF THE GEOID

A variety of different models of geoid elevation over the earth have been proposed (Haxby and Turcotte, 1978; Sandwell and Schubert, 1980; Chase and McNutt, 1982; Dahlen, 1982; Lister, 1982; Hager, 1983; Haxby, 1983; Hager, 1984; Richards and Hager, 1984; Hager et al., 1985). The geoid anomaly is a second-order quantity caused by variations from the ideal (i.e., equilibrium) state of the earth. One large scale geoid signal results from the cooling of the oceanic lithosphere because of density contrasts within it. Ockendon and Turcotte (1977) and Haxby and Turcotte (1978) showed that the geoid anomaly, γ, is directly related to the dipole moment of the density-depth distribution in isostatically compensated regions

$$\gamma = -\frac{2\pi G}{g} \int z\rho \, dz$$

which is sometimes called the HOT equation, where G is the gravitational constant, g is the acceleration of gravity, ρ is the density change, and z is the depth. Haxby and Turcotte (1978) showed

that the geoid anomaly, based on the boundary layer model (Davis and Lister, 1974), is characterized by a linear age-geoid height relationship for the North Atlantic lithosphere of -0.16 m/my. Sandwell and Schubert (1980) showed that for ages less than 80 my the geoid height decreases almost linearily with age of seafloor, for most of the ocean basins, again in agreement with the boundary layer model. The fact that the seafloor topography flattens for ages greater than 80 my indicates a reduction in the rate of boundary layer thickening.

A major step towards understanding the definition of isostasy was achieved by Dahlen (1982), who pointed out that the geoid anomaly is extremely sensitive to the definition of isostasy that is applied. If we adopt the definition that the pressure is everywhere the same at the compensation level (Heiskanen and Vening Meinesz, p. 133, 1958) then the geoid anomaly is $\gamma = 2\gamma_{HOT}$. If we use the assumption that mass in every conic column is the same, then the geoid anomaly is (Turcotte and McAdoo, 1979)

$$\gamma = \frac{n}{n + 1/2}\gamma_{HOT}$$

where n is the spherical harmonic degree. The geoid anomaly, γ, is smaller than γ_{HOT} for n=2 by 20% and gets asymptotically closer for larger values of n. Dahlen (1982) proposed another approach to utilize an interpretation of the overall pattern of intraplate earthquake mechanisms: that the deviatoric stress is everywhere minimum (Dahlen,

1981). In this case, the geoid anomaly is about 60% larger than γ_{HOT} for n=2 and decreases asymptotically for larger values of n. The two main disadvantages of Dahlen's approach are that topography on the outer surface must be represented by a Dirac delta function, which rules out the self-deformation effect we will consider, and that the acceleration of gravity must be taken constant everywhere. Both of these effects will be discussed in detail in the next chapter.

Another possible cause of geoid anomalies is the convective flow in the mantle resulting from thermal density contrasts. Numerous models attempting to calculate the effect have been proposed, and they are divided between two main categories: whole-mantle convection and layered mantle convection (i.e. Parsons and Daly, 1983; Hager, 1984; Ricard et al., 1984; Richards and Hager, 1984; Jarvis and Peltier, 1986). Pekeris (1935) showed that surface deformation and the gravitational effect of buried density differences causing the mantle flow are opposite in sign. McKenzie et al. (1974) showed that for a convecting fluid with a uniform viscosity, the net gravity anomaly will be positive over an upwelling region, in spite of the higher temperature and lower density there. Correlation of the gravity anomaly and the surface deformation is sensitive to the viscosity structure and depth of convecting layer (McKenzie, 1977). Surface deformation and gravity anomalies may be negative over a rising region if the viscosity is temperature dependent. McKenzie (1977) concluded that a model of static compensation cannot explain the correlation between geoid anomaly and bathymetry; instead one needs some form of

dynamical compensation to support the geoid anomaly and bathymetry. Dziewonski et al. (1977) observed a negative correlation between the long wavelength gravity anomalies observed at the surface and those computed from seismic velocity anomalies at depths greater than 1100 km.

There is common agreement that boundary deformations, especially the upper boundary (earth's surface), have appreciable influence upon the observed geoid or gravity field caused by density contrasts at depth (Runcorn, 1964, 1967; Morgan, 1965a, b; McKenzie, 1977; Parsons and Daly, 1983; Hager, 1984; Ricard et al., 1984; Richards and Hager, 1984; Jarvis and Peltier, 1986). Hager (1984), Richards and Hager (1984), and Hager et al. (1985) showed that boundary deformations due to density contrasts reach equilibrium on the time scale of 10^5 years or less, like the time scale of postglacial rebound (Haskell, 1935; Heiskanen and Vening Meinesz, 1958; Cathles, 1971). As a significant change in the mantle flow pattern occurs in a much longer time scale (10^7 years or more), the former process can be considered as occurring instantaneously. In addition, Hager (1984) and Richards and Hager (1984) showed that variations of viscosity with depth or temperature cause significant magnitude and sign changes of the geoid anomalies. For a given mass density, the geoid anomalies observed due to a whole-mantle convective system are larger than those associated with the layered model.

Recently three-dimensional models of the mantle density using P and surface wave tomography were obtained (Masters et al., 1982; Nakanishi and Anderson, 1983, 1984; Dziewonski, 1984; Nataf et al.,

1984; Woodhouse and Dziewonski, 1984). Attempting to correlate mantle mass heterogeneity with the geoid anomaly has proven to be problematic. Woodhouse and Dziewonski (1984) found a 0.7 correlation between upper mantle structures and the geoid for spherical harmonic degrees 2 and 3. However, including the crustal correction (i.e., correction due to the influence of the density distribution in the crust) results in a smaller correlation of about 0.4. Similar correlations of about 0.4 are observed for degrees 4 to 7, but with a negative sign. Another critical point, also found by Masters et al. (1982), is that the calculated geoid is about five times larger than is observed.

Continents, oceanic ridges and ocean basins are characterized by both geoid highs and lows. Crough (1978), Chase (1979), and Crough and Jurdy (1980) showed that there is a remarkable positive correlation between residual geoid highs and hot spots. Over hotspots we observe broad geoid highs. However, no obvious correlation is seen between continental or seafloor topography and the observed geoid or the residual geoid (i.e., after removing the effect of the cooling oceanic lithosphere and the continents).

So far we have described the recent studies of the geoid. Various models attempt to calculate the lithospheric effect on the geoid and the effect of flow in the mantle. In addition, correlation of the geoid with surface topography or with deep structures has usually appeared doubtful. No model has provided sufficient and conclusive explanation and results that fully describe the geoid over the earth.

A better understanding of the observed geoid anomaly can be achieved only if we carefully take into consideration all the effects that influence the geoid, something that has never been fully executed. The first step is to focus our attention on the calculation of the lithospheric effect on the geoid. This is done in the next sections, using a complete model of the oceanic and continental lithosphere, following Davis and Lister (1974) and Lister (1982). Next is the interpretation of the residual geoid, after the removal of the lithospheric effect. Here we seek to provide an estimate of the importance of mantle flow.

CHAPTER TWO - DEFINITION OF ISOSTASY

Our first step is to give a qualitative definition of isostasy. This provides physical insight into the problem, and also serves as an introduction to the mathematical development that follows.

1. FLAT EARTH

The Heiskanen definition of isostasy (Heiskanen and Vening Meinesz, 1958) states that if the earth were flat there would be columns of variable height which produce a constant pressure at the reference depth (see Figure 3). Assuming that the acceleration, g, due to gravity is constant everywhere, we could calculate the height of the cooling lithosphere for any given density (Davis and Lister, 1974; Parsons and Sclater, 1977).

Haxby and Turcotte (1978) and Lister (1982) have shown that the geoid height is dependent on the first moment of the mass. As a simple

20

Figure 3.   Isostasy on a flat earth.
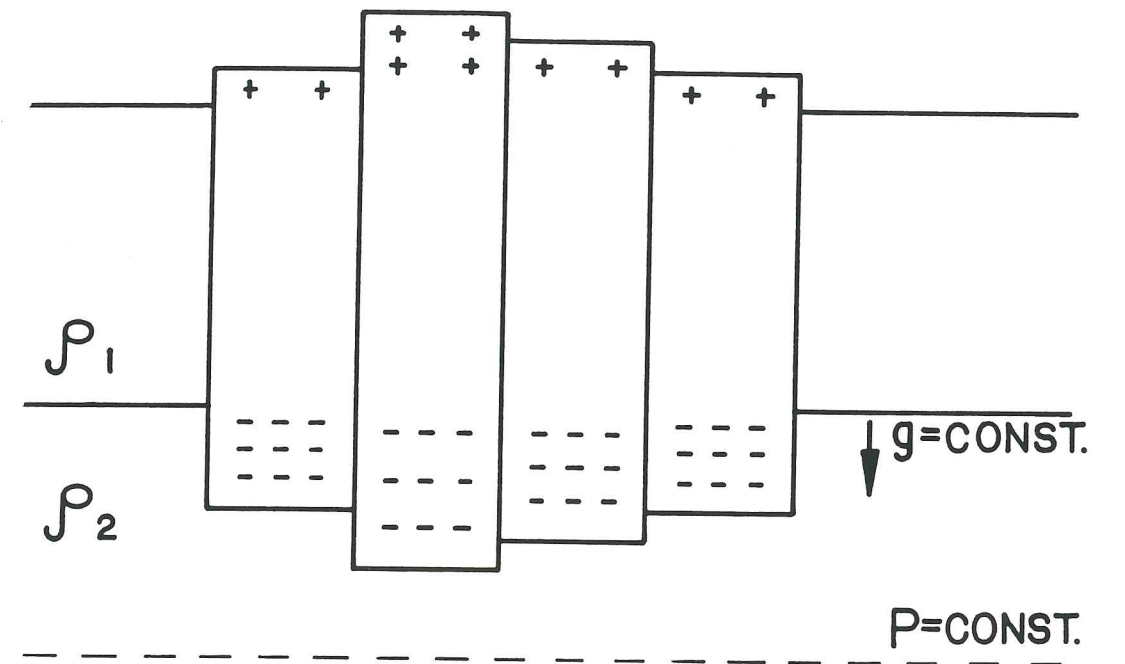
example, the geoid height, Y, over an infinite dipole sheet is

$$Y = \frac{2\pi Gm}{g}$$

where m is the dipole density and G is the gravitational constant. Both the mass redistribution and the thickness of the cooling lithosphere are proportional to $\sqrt{t}$, where t is the age of the cooling lithosphere. This means that the geoid height should be proportional to the age.

2. SPHERICAL EARTH

Since the earth's surface is in reality curved, the situation is more complicated than that just described. For example, a difficulty might arise when one calculates the geoid anomaly due to a sheet of mass dipole (Lister, 1982), as the contribution to the geoid is positive above the equator of the dipole and negative below the equator. In other words, at long wavelengths sphericity is important and the far-field effects, resulting from sphericity and distant density contrasts, bias measurements of geoid slopes.

To obtain the geoid anomaly over a sphere one must calculate all the second-order effects (Dahlen, 1982). Vening Meinesz (1946) pointed out two second-order effects. The first effect is that columns on a sphere are pie-shaped rather than straight-sided. This means that the volume for the density anomaly associated with a positive (upward)

mass moment (see Figure 4) is greater. The second effect is that the acceleration of gravity increases slightly with, depth, producing a similar bias toward mass or volume in the upper layers. Positive topography, or a positive mass dipole, is therefore associated with extra mass in the region, even when the pressure on the reference surface remains constant.

These effects initiate a process which is called self-deformation (Hager, 1983; Haxby, 1983; Ricard et al., 1984). To get a better picture of this process, let us assume that the earth is a perfect sphere in isostatic equilibrium, covered by ocean and underlain by the lithosphere (thickness about 100 km) and the asthenosphere. Let us now introduce a mass dipole to this model,(i.e. an oceanic ridge). The result is a depression of the reference surface and an uplift of the geoid height. Because of the pressure gradient, seawater will flow into the uplift of the geoid along the equipotential surface, to maintain equilibrium. The gravitational potential of the deformed earth is a sum of all the contributions from each point on the earth, but unlike the "old" gravitational potential the "new" potential is not symmetric and equal everywhere. Potential highs indicate excess mass, while lows signal a mass deficiency. The gravitational potential from the added mass will cause a further deformation of the earth; this deformation, in turn, increases the gravitational potential, which leads to an increased deformation of the earth. This process continues until the deformed surface of the earth lies along the equipotential surface. The net result of this process is a redistribution of the earth's mass and a distortion of its shape.

Figure 4.   Isostasy on a spherical earth.
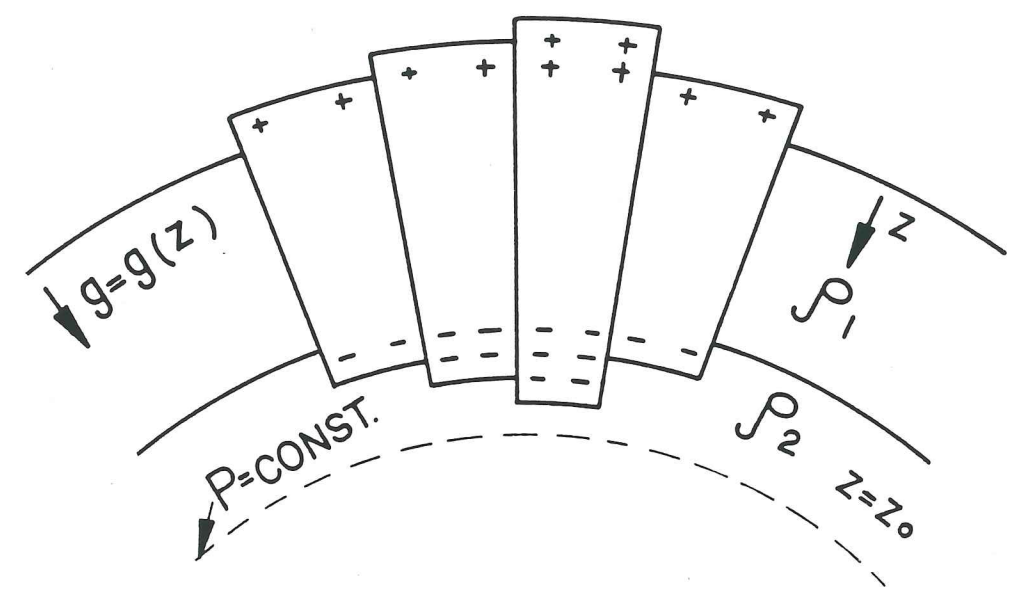
We can point out seven effects that cause the deformation of sea level (see Figure 5). The direct dipole initiates the deformation, while the other effects provide positive or negative contributions, depending on their nature. Pie-column masses tend to add to the total effect as was noted above. The pie-column reference surface effect, pie-column reference self-effect, and ocean surface mass effect are by-products of the first deformation. The increase in the mass will add a positive gravitational potential or an uplift of the geoid. The dipole reference surface effect and the dipole reference surface self-effect produce negative contributions. The surface of constant pressure in fluid equilibrium follows the local equipotential, or geoid surface. This is initiated by the dipole effect, which presses the reference surface downwards. The dipole self-effect produces another negative contribution. The pie-column mass effect, the pie-column mass self-effect, and ocean mass effect tend to lift both the reference surface and the outer geoid upwards.

There are three basic requirements which this process must satisfy. First, the process should be stable; otherwise, increasing amounts of mass would constantly be added to some region of the earth with a corresponding mass subtraction elsewhere, eventually leading to a significant deformation of the spherical earth-which has not been observed. The second requirement is that the process should rapidly converge; slow convergence would mean that any initial deformation will add a large amount of mass at the second step, relative to the initial deformation leading to planetary fission. In reality, this

Figure 5. The self-deformation process. Thick solid lines – initial
surfaces and dashed lines – final surfaces.

FINAL OCEAN
SURFACE

+ DIRECT DIPOLE
- DIPOLE REF. SURFACE
- D. R. SURF. SELF - EFFECT
+ PIE-COLUMN MASS
+ P.C.R.S. EFFECT
+ P.C.R.S. SELF - EFFECT
+ OCEAN SURFACE MASS

OCEAN

EXTRA
MASS

LITHOSPHERE

ASTHENOSPHERE

$P = CONST.$

+ PIE-MASS EFFECT
+ OCEAN MASS EFFECT
+ SELF-MASS EFFECT

- DIPOLE EFFECT
- SELF MASS EFF.
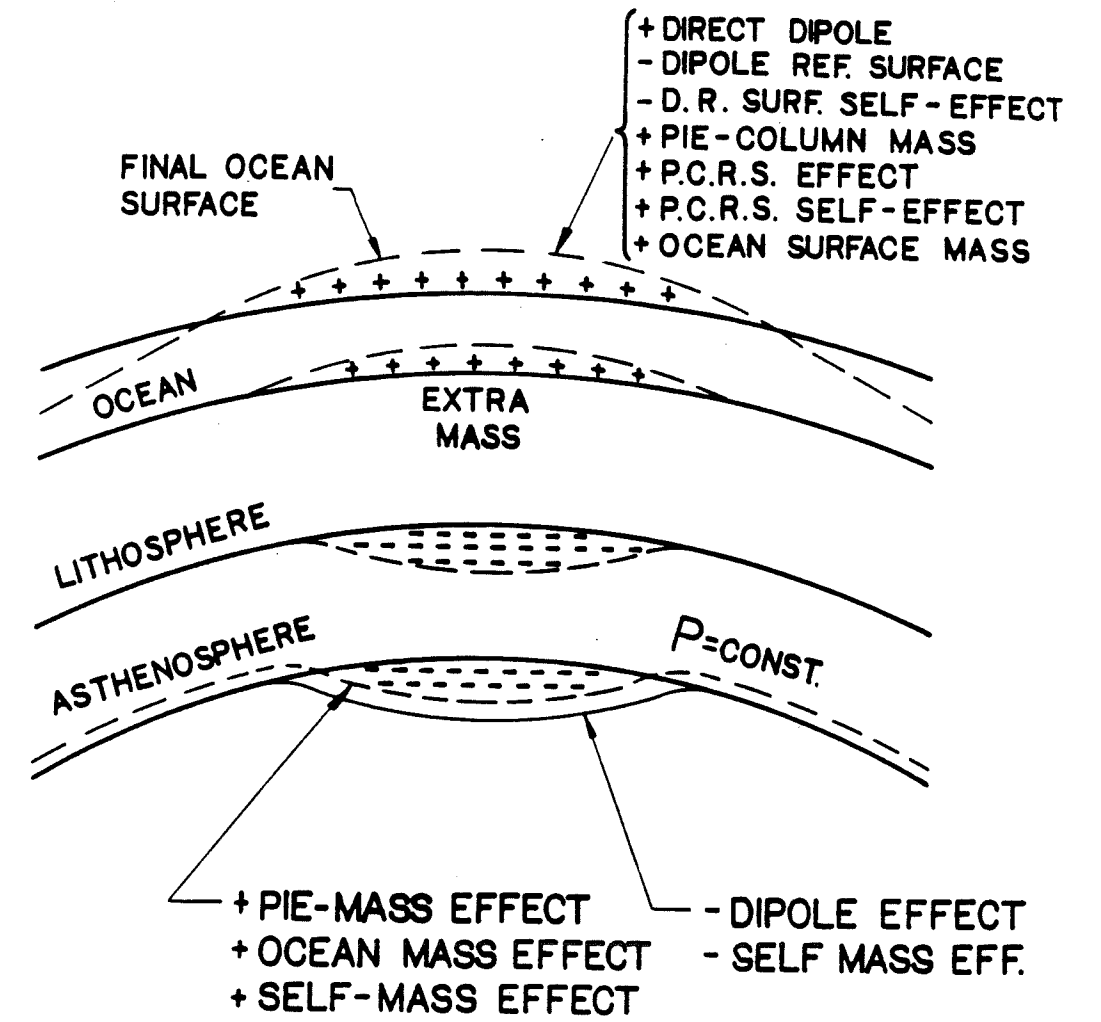
effect is assumed to be a modest correction to the direct geoid anomaly, and therefore fast convergence is expected. The mathematical method, however, goes directly to the equilibrium state by matrix inversion. Finally, we require conservation of mass; only a redistribution of mass is permitted.

CHAPTER THREE - THE EQUATION OF GEOID ANOMALY

We now turn to a rigorous definition of the problem. We assume that the earth is a perfect sphere, and using the conventional spherical coordinates R, Θ, and Φ to denote the location of any point $Q=Q(x,y,z)$ on the earth

$$x = R \sin \Theta \cdot \cos \Phi$$

$$y = R \sin \Theta \cdot \sin \Phi$$

$$z = R \cos \Theta$$

where R is the radius of the earth (6.371×10^6 m), Θ is a latitudinal angle measured from one pole ($0 \le \Theta \le \pi$), and Φ is the longitude ($0 \le \Phi \le 2\pi$). The distance between points i and j is given by r_{ij}

$$r_{ij} = [(x_i - x_j)^2 + (y_i - y_j)^2 + (z_i - z_j)^2]^{1/2}$$

$$= R[(\sin \Theta_i \cdot \cos \Phi_i - \sin \Theta_j \cdot \cos \Phi_j)^2 + (\sin \Theta_i \cdot \sin \Phi_i - \sin \Theta_j \cdot \sin \Phi_j)^2$$

$$+ (\cos \Theta_i - \cos \Theta_j)^2]^{1/2} \quad .$$

If $\phi_i = 0$ then

$$r_{ij} = \sqrt{2} \cdot R \left[1 - \sin \theta_i \cdot \sin \theta_j \cdot \cos \phi_j - \cos \theta_i \cdot \cos \theta_j \right]^{1/2}.$$

Let

$$a = 1 - \cos \theta_i \cdot \cos \theta_j$$

$$d = \sin \theta_i \cdot \sin \theta_j$$

$$X = a - d \cdot \cos \phi_j$$

These definitions yield a new form of r_{ij}

$$r_{ij} = \sqrt{2 \overline{X}} R .\tag{1}$$

Equation 1 represents the distance between two points on a sphere. We next calculate the distance between a point and a surface element. The spherical earth is divided into L rings, with a latitude width of 180/L degrees per ring, starting from the pole. In general, the rings do not follow the earth's coordinates; this means that the pole of our ring system is usually not the north pole or the south pole, but the observation point of interest.

If we add some mass to the j-th ring, the contribution of the j-th ring to the gravitational potential or the geoid height in any other ring i may be calculated. In general, the gravitational potential P_{ij} is written

$$P_{ij} = G \int \frac{dm_j}{r_{ij}} = G \int \frac{\rho dv_j}{r_{ij}} \ .$$

Each value of the matrix P_{ij} is the total contribution that a point in the middle of ring i will "feel" due to ring j, G is the gravitational constant $((6.673\pm0.001)\times10^{-11} Nm^2/kg^2)$, h is the height of the material in ring j, and ρ is the density of the seawater (1030 kg/m^3) or mantle rock (3300 kg/m^3). In order to simplify the calculation of the integral, we assume that the height of the mass, h, is very small compared to r_{ij}; one can integrate over the j-th ring to obtain the inter-ring coefficient

$$P_{ij} = G\rho h \int \frac{ds_j}{r_{ij}} \ ,$$

where s_j is the area of the j-th ring. A surface element, ds_j, in spherical coordinates is

$$ds_j = R^2 \sin \Theta_j \, d\Phi_j \, d\Theta_j$$

where Θ_j is limited by the ring boundaries, $\Theta'_j \leq \Theta_j \leq \Theta''_j$. Thus, each surface element in the j-th ring contributes to the gravitational potential observed in the i-th ring. Using Equation 1, we therefore obtain

$$P_{ij} = G\rho h \int_{\Theta'_j}^{\Theta''_j} \int_0^{2\pi} \frac{R^2 \sin \Theta_j \, d\Phi_j \, d\Theta_j}{\sqrt{2} \sqrt{X} \, R} \; .$$

After some algebra, the gravitational potential matrix, P_{ij}, is found to be

$$P_{ij} = \sqrt{2} GRh\rho \int_{\Theta'_j}^{\Theta''_j} \int_0^{\pi} \frac{\sin \Theta_j \, d\Phi_j d\Theta_j}{\sqrt{X}} \; . \tag{2}$$

The calculated geoid height matrix, Γ_{ij}, that is observed in ring i due to 1 meter of seawater in ring j is

$$\Gamma_{ij} = \frac{P_{ij}}{g} \; , \tag{3}$$

where **g** is the gravitational acceleration (9.8 m/sec²) and the geoid

height is in meters.

CHAPTER FOUR - ESTIMATION OF THE GEOID HEIGHT

The integral in Equations 2 or 3 above cannot be analytically solved for all cases; we must therefore approximate it using numerical means. The overall problem was divided into the following cases:

    a) Influence of a cap on itself.

    b)   "   " a cap on the other cap.

    c)   "   " a ring j on a cap   ,j≠1 and j≠L.

    d)   "   " a cap on a ring j   ,j≠1 and j≠L.

    e)   "   " a ring j on a ring i   ,j≠i and j,i≠1,L.

    f)   "   " a ring j on itself   ,j≠1 and j≠L.

In these calculations, we assume that h is the height of the seawater, R is the radius of earth, G is the gravitational constant, ρ is normalized to the density of seawater, and g is the acceleration of gravity. First, we discuss case (a), which is the influence of a cap on itself (see Figure 6). We assume a spherical cap of angle θ_c. The distance between the pole and incremental ring dθ is

$$2R \sin (\theta/2) \ ,$$

Figure 6. The influence of a cap on itself.
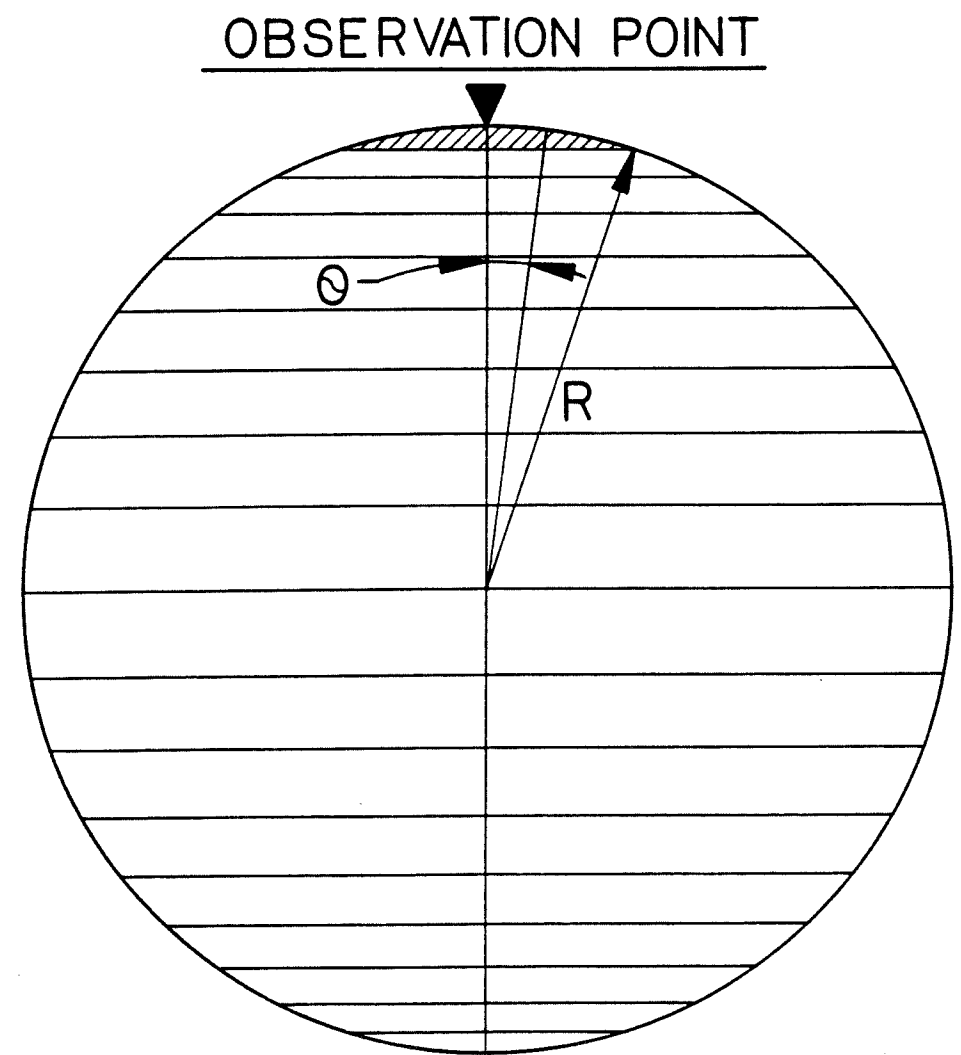
and the mass of this ring is

$$2\pi R^2 \rho h \sin \theta \, d\theta \, .$$

Thus, the contribution to the potential is

$$dP_{1,1} = dP_{L,L} = 2\pi GR\rho h \cos (\theta/2) \, d\theta$$

The geoid anomalies at the poles, $\Gamma_{L,L}$ or $\Gamma_{1,1}$, are

$$\Gamma_{L,L} = \Gamma_{1,1} = \frac{2\pi GR\rho h}{g} \int_0^{\theta_c} \cos (\theta/2) \, d\theta = \frac{4\pi GR\rho h}{g} \sin (\theta_c/2)$$

Case (b), which is the influence of a cap on the other cap (see Figure 7), is similar to case (a). We define $\theta = \pi - \theta_1$, and the range of θ is $\pi - \theta_c \le \theta \le \pi$. Thus, the geoid height observed at the pole due to the other cap is

$$\Gamma_{L,1} = \Gamma_{1,L} = \frac{2\pi GR\rho h}{g} \int_{\pi-\theta_c}^{\pi} \cos (\theta/2) \, d\theta = \frac{4\pi GR\rho h}{g} [1 - \cos (\frac{\theta_c}{2})]$$

Case (c), which is the influence of a ring on a cap, is similar to cases (a) and (b) (see Figure 8). The range of θ is now $\theta_j' \le \theta \le \theta_j''$, for a

Figure 7. The influence of a cap on the other cap.

OBSERVATION POINT
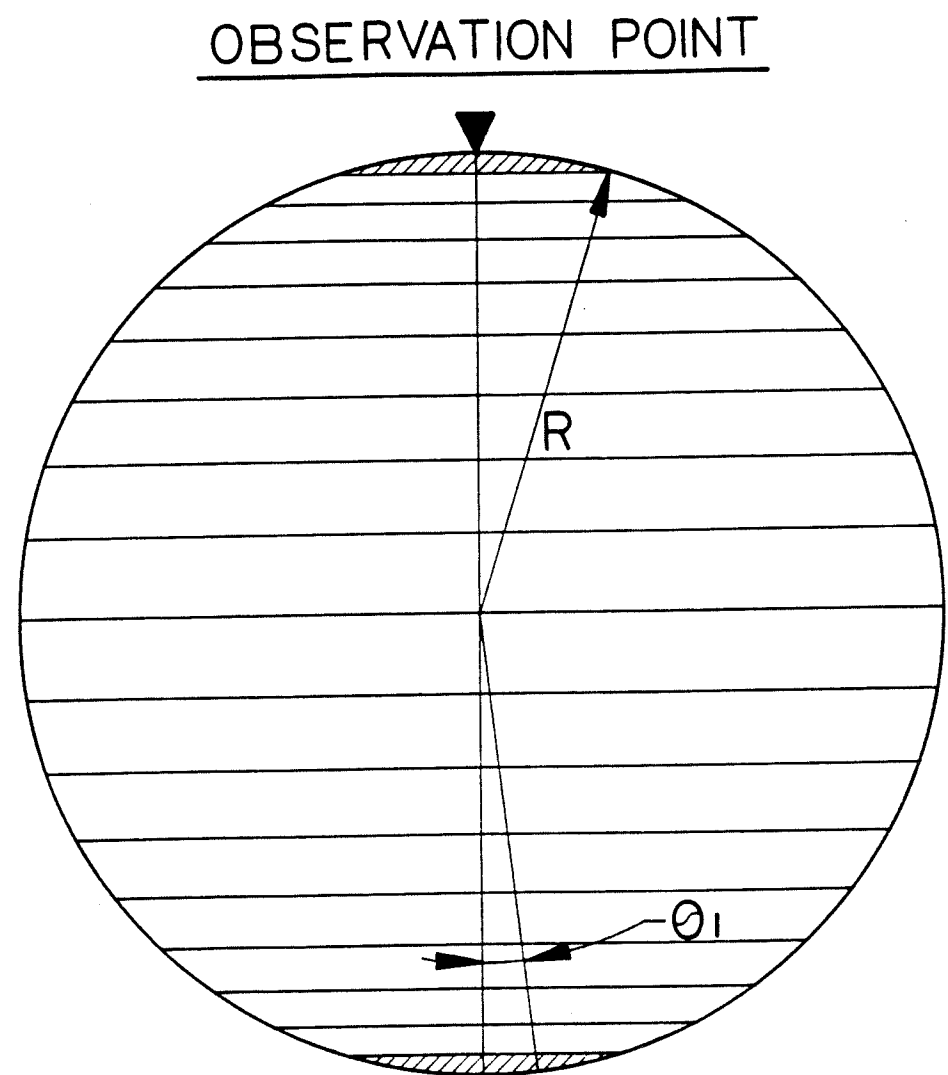
Figure 8.   The influence of a ring on a cap.
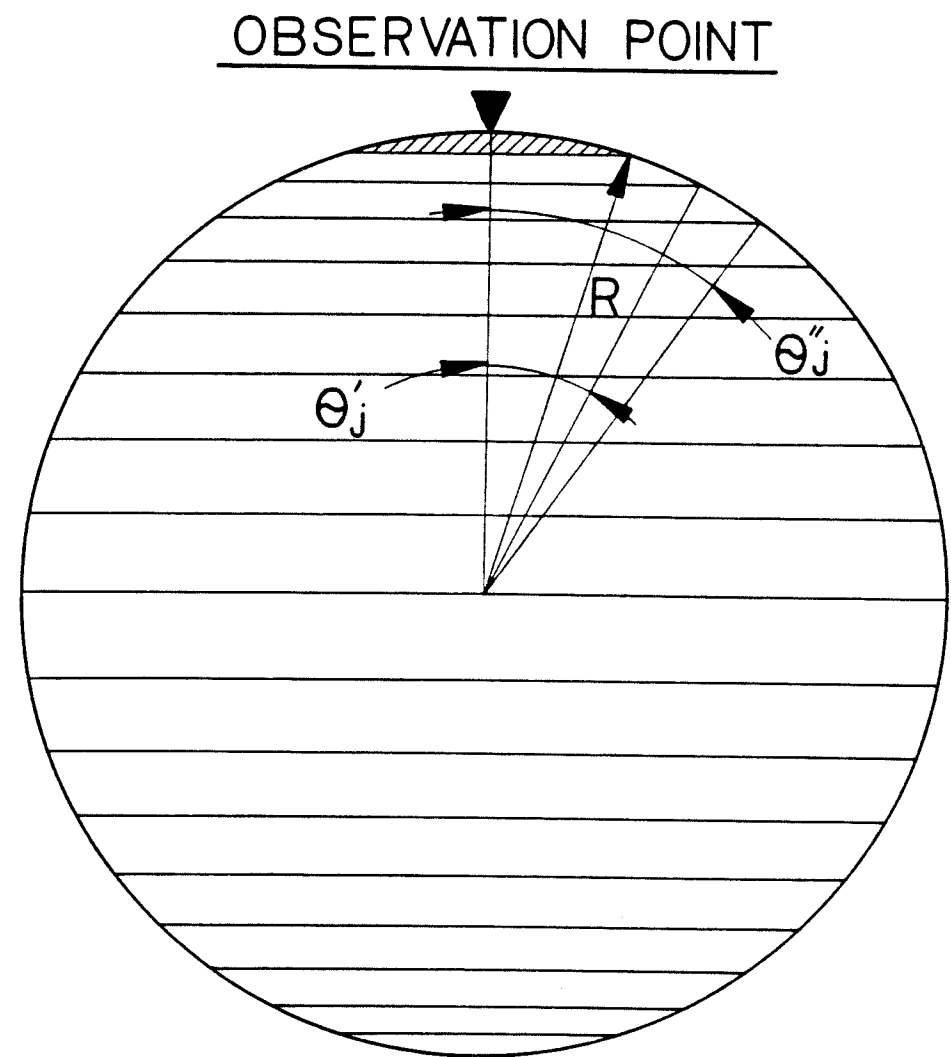
given ring j. The geoid height observed at the pole due to ring j is

$$\Gamma_{1,j} = \Gamma_{L,L-j+1} = \frac{2\pi GR\rho h}{g} \int_{\Theta'_j}^{\Theta''_j} \cos(\Theta/2) \, d\Theta$$

$$= \frac{4\pi GR\rho h}{g} [\sin(\frac{\Theta''_j}{2}) - \sin(\frac{\Theta'_j}{2})] \quad , j=2,3\ldots L-1 \; .$$

This exhausts the cases of circular symmetry that can be solved analytically. We now use Romberg's method, described in Appendix A, to evaluate Equation 2. Cases (d) and (e) do not involve any singular points. We calculate the geoid height in the middle of a ring i, due to the mass in a cap or another ring j. The range of Θ is $0 \leq \Theta \leq \Theta_c$, or $\pi - \Theta_c \leq \Theta \leq \pi$ for the caps, and $\Theta'_j \leq \Theta \leq \Theta''_j$ for ring j. The geoid anomaly for these cases is expressed in Equation 3.

Case (f), which is the influence of a ring on itself (excluding the caps), involves a singular point. This singularity occurs when the distance between two points inside the ring becomes zero, and the integrand in Equation 3 becomes infinite. In order to avoid this problem, we define a small square of 0.1°x0.1° around the singular point; then we can define four separate zones (see Figure 9). The integration was done for each of the zones A, B and C to obtain their contribution to the geoid height. In order to simplify the calculation of the contribution of the square (zone D), a circle with the same area was used. The contribution to the geoid height is $2\pi g b\rho h/g$, where

Figure 9. The influence of a ring on itself.
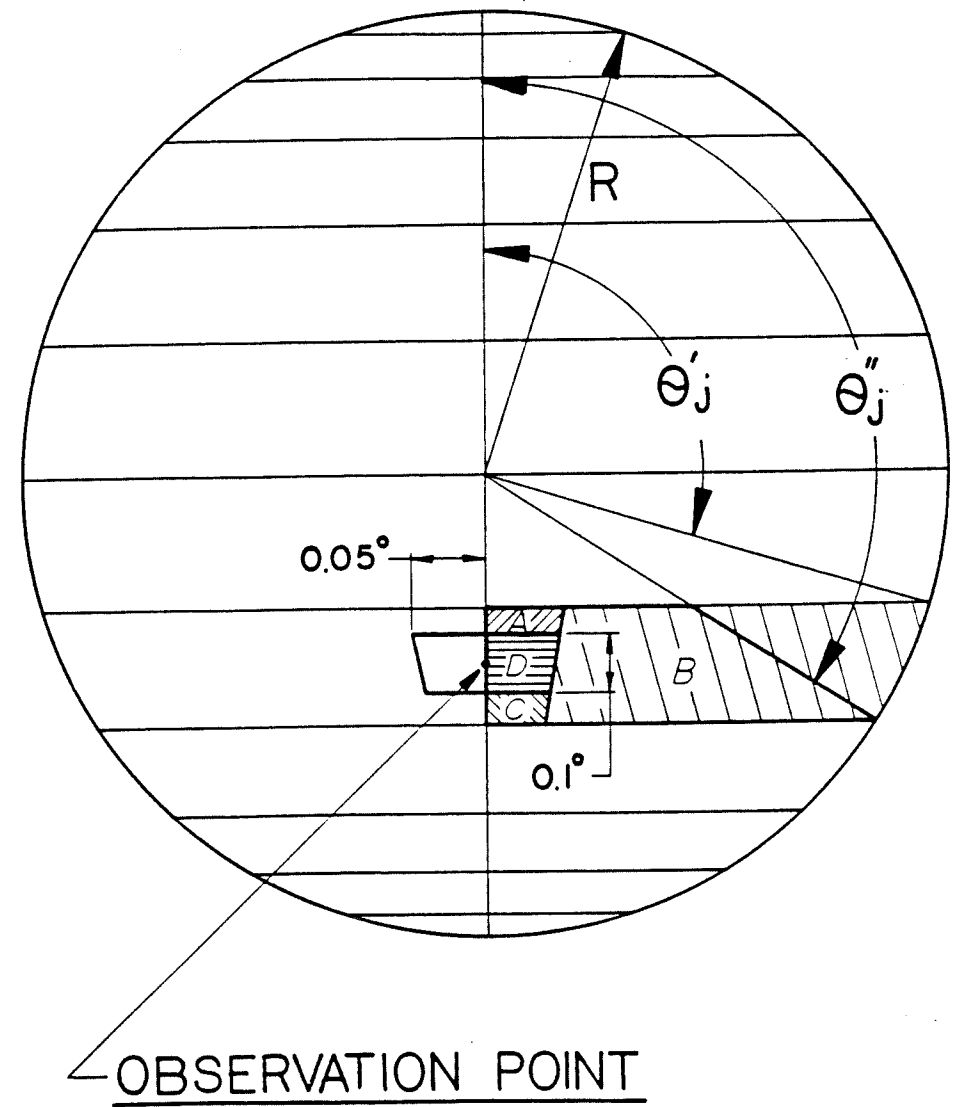
b is the radius of the circle. The total geoid height in this case is the sum of all the four contributions.

CHAPTER FIVE - EXTRACTION OF THE GEOID HEIGHT

Models are considered for 18, 36 and 90 latitudinal rings; the rings are 10, 5 and 2 degrees wide. The relative error of each integration, which gives an estimate of accuracy of the integration, is obtained through division of the error of integration by the value of the integral. For these models, the largest relative errors of the integration are 2×10^{-4}%, 9×10^{-4}% and 2×10^{-3}%, respectively. Normally, the errors are at least an order of magnitude smaller than those just mentioned.

Any deformation of the spherical earth implies the presence of regions of excess mass (geoid highs), and others with mass deficiency (geoid lows). The net change of mass must be zero. The corrected geoid, Γ'_{ji}, observed in ring j due to 1 meter of seawater in ring i, after the redistribution of earth's mass, is

$$\Gamma'_{ji} = \Gamma_{ji} - \frac{\sum_{i=1}^{L} \Gamma_{ji} \cdot S_i}{S_T} \tag{4}$$

where S_T is the area of the earth and S_i is the area of the i-th ring.

Figure 10. The cap of 18 ring model is covered with 1 meter of seawater. Spheres A (dashed line) and B (solid line) are the earth before and after the perturbation, respectively.
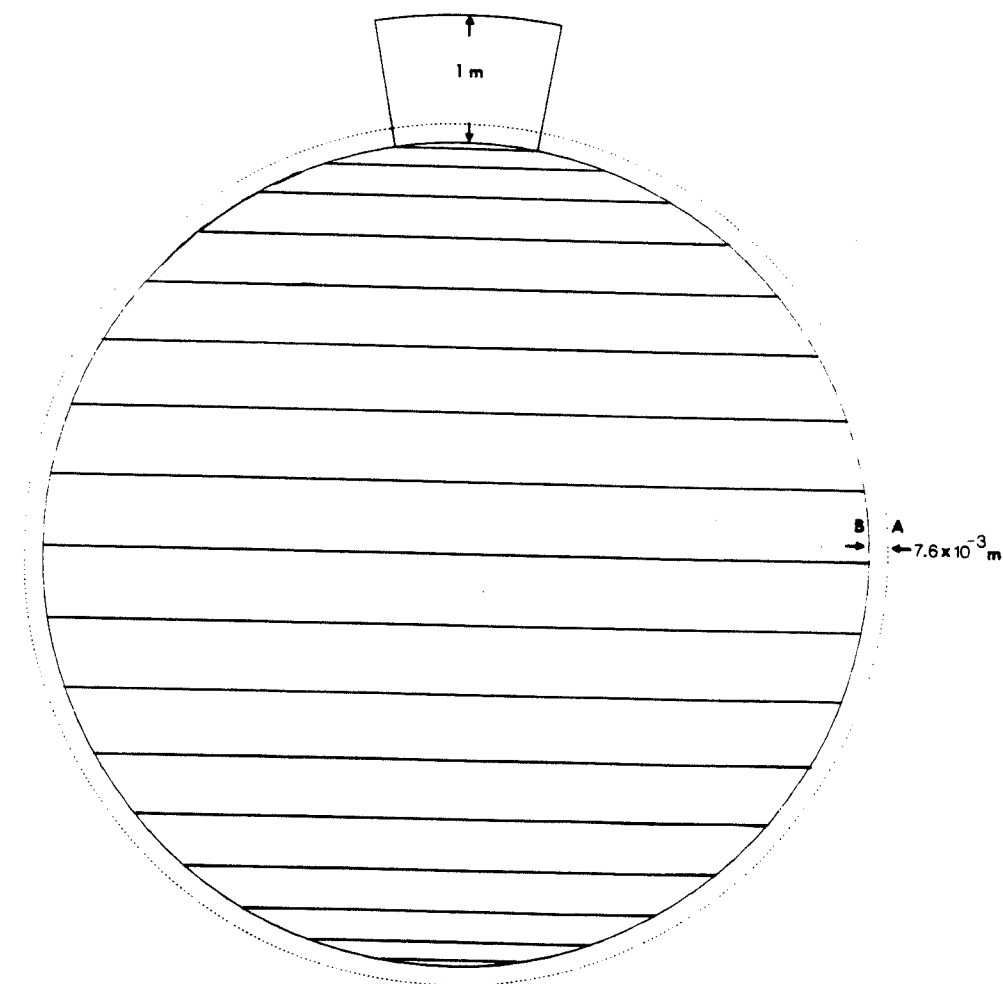
Figure 11. The final shape of the earth for the three models of 18, 36 and 90 latitudinal rings, due to the mass of 1 meter of seawater over the pole (solid heavy line). Spheres A and B are as in the previous figure. 18 ring model - solid line, 36 ring model - long dashed line and 90 ring model - short dashed line.
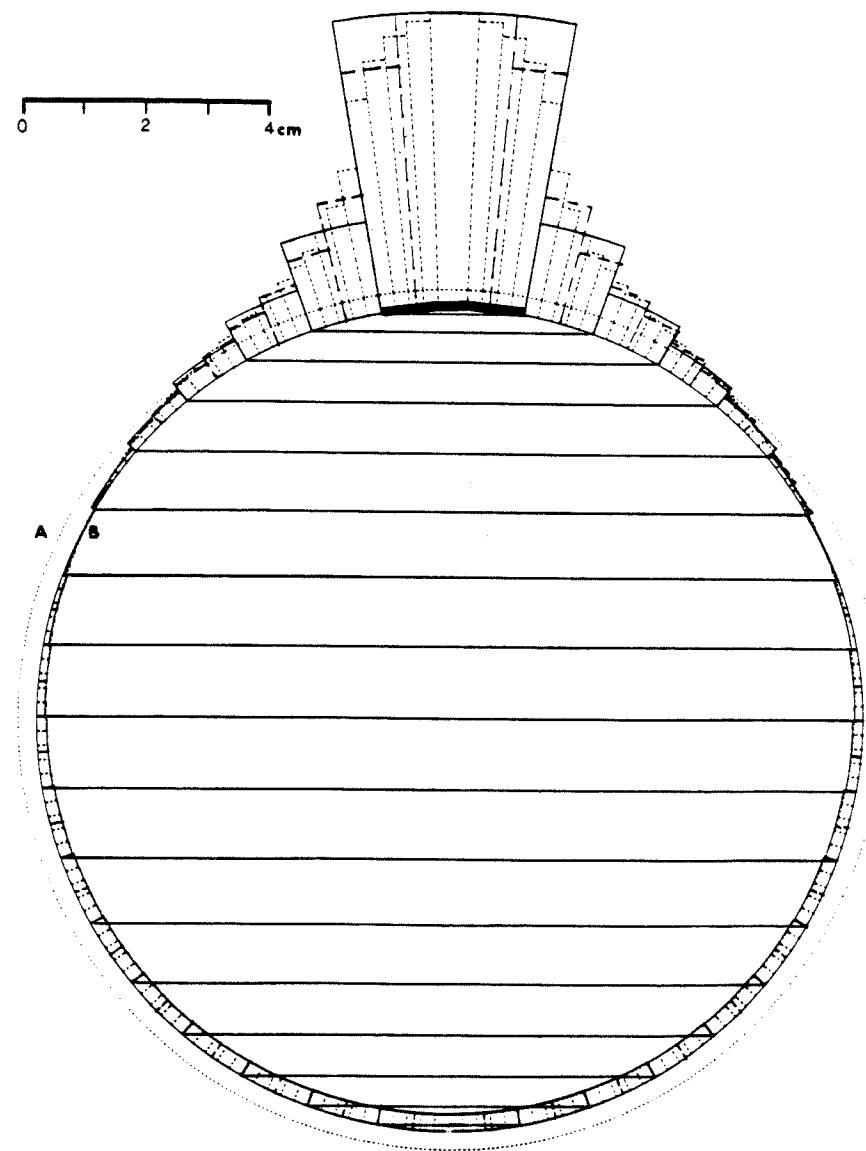
To illustrate the method, a cap equal in size to one ring of the coarsest model was covered by a mass sheet equivalent to 1 meter of seawater (see Figure 10). The redistribution of the mass, due to the addition of seawater in any given ring and subtraction of the same amount from other regions, should not change the total mass of the earth (conservation of mass). This constraint is expressed by the equation

$$\sum_{i=1}^{L} \Gamma'_{ji} \cdot S_i = 0$$

So far we have calculated the geoid height matrix Γ', the geoid height observed in ring i due to 1 meter of seawater in ring j. To avoid any confusion, we will refer to the matrix Γ' in subsequent sections as Γ^{ss}_{ji}. This initial perturbation of mass over a given ring will cause subsequent perturbations in all other rings as well (see Figure 11). As explained above, the earth goes through a self-deformation process until equipotentials and lines of constant pressure coincide. Let γ be the final geoid height matrix that is obtained by using the equation

$$(\gamma + \gamma_0)\Gamma' = \gamma ,$$

this yields

$$\gamma = \gamma_0 \Gamma'(1 - \Gamma')^{-1}, \qquad (5)$$

where γ_0 is the initial topography on the geoid. The deformation is not large for such a small area of initial perturbation, and the low density of seawater; nevertheless, the correction to geoid height at the pole is significant.

Another error inherent in these computations is due to the number of rings in the model; it is clear that the number of rings affects the accuracy of the results. We might expect that the error due to the use of coarse models would converge to some value as the number of rings increases. The initial perturbation at the cap of 10° is over one ring for an 18-ring model, but over two rings for the 36-ring model and over five for the 90-ring model. Using the 36-ring model instead of the 18-ring model changes the results by at most 2.2%; the 90-ring model results in a 3.7% change. It means that the coarse 18-ring model can serve as a reasonable approximation to the earth. If we follow the above procedure and using each time another ring, instead of the cap, we find that the maximum final geoid anomalies are 0.06m, 0.03m, and 0.02m, which are self-effect results of 1 meter of seawater observed at the center of rings 3, 5 and 10 for 18, 36 and 90-ring models, respectively.

Figure 12 illustrates the case of increasing cap size. The abscissa gives the size of the initial perturbation of 1 meter of seawater, a spherical cap centered on the point of observation. Since the added water must come from the rest of the earth, the initial

Figure 12. Increasing cap size. The geoid anomaly is the contribution
in meters due to the mass of 1 meter of seawater over the
cap. 18 ring model - diamonds, 36 ring model - squares and
90 ring model - crosses.
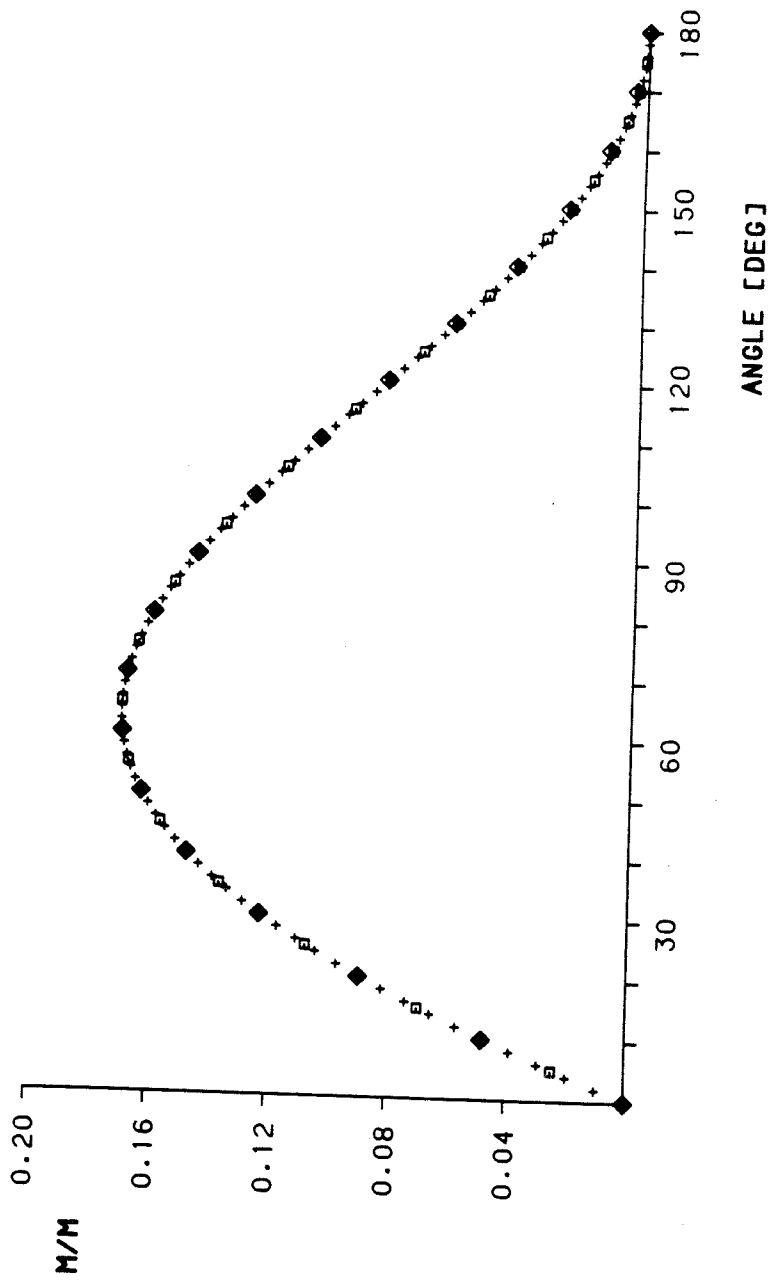
perturbation vector relative to the spherical earth is of the form

$$\tilde{\gamma}_0 = (1-\alpha, 1-\alpha, \ldots, 1-\alpha, -\alpha, -\alpha, \ldots, -\alpha)$$

with

$$\alpha = \frac{\sum\limits_{i=1}^{r} S_i}{S_T}$$

where S_i is the area of the i-th ring, r is the number of rings in the perturbed cap, and S_T is the area of the earth.

Increasing the cap size increases the geoid anomaly until the cap angle reaches $60°$; significantly, this is the size of the Pacific Ocean. Figure 12 shows the excellent agreement between the 18, 36 and 90-ring models.

CHAPTER SIX - DESCRIPTION OF THE TEST MODEL

We assume a simple model of a test planet, that is very similar to the real earth, which is based on the boundary layer model (Davis & Lister, 1974). The planet is composed of an ocean which is underlain by the lithosphere and asthenosphere (see Figure 13). There are no continents in this model. The lithosphere is created at a vertical plane boundary that is fixed at initial temperature T_1. As the lithosphere moves away from the ridge, it cools to unlimited depth. The upper boundary of the lithosphere is kept at temperature T=0. Davis and Lister (1974) showed that the temperature, T, is (using Carslaw & Jaeger, 1959, p. 59, and ignoring lateral heat flow near the origin)

$$T = T_1 \ erf\left(\frac{z}{2\sqrt{\kappa t}}\right)$$

where z is depth, κ is diffusivity, and t is age. Davis and Lister (1974) showed that the seafloor topography, h, is a linear function of

Figure 13. A model of the cooling lithosphere using the boundary layer

model (Davis & Lister, 1974).
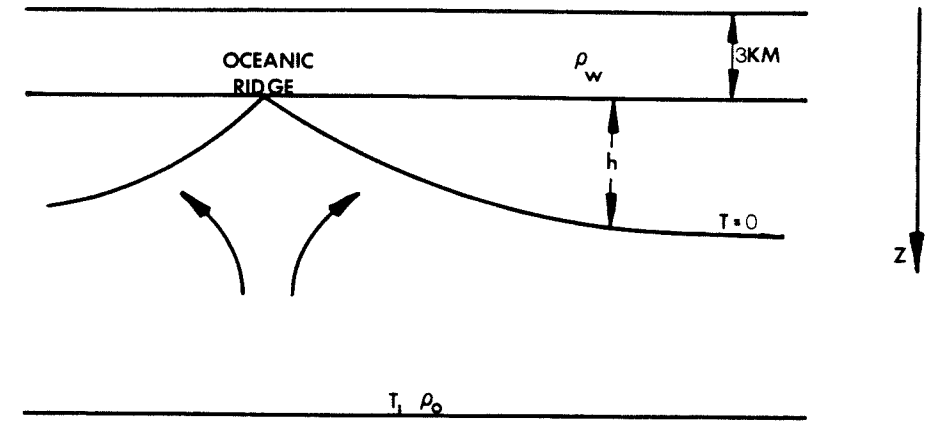
square root of age

$$h = \frac{2}{\sqrt{\pi}} \, T_1 \, \sqrt{\kappa t} \; \alpha \; \frac{\rho_0}{\rho_0 - \rho_w} \; ,$$

where α is thermal expansion coefficient, ρ_0 is initial density, and ρ_w is seawater density. Away from the ridge, the surface of the cooling lithosphere is colder and denser than the lower part of the lithosphere, therefore the density difference causes a mass dipole. This construction of dipole sheets is illustrated in Figure 14. In order to estimate the geoid effect by means of mass dipoles we need to convert the density differences in the cooling lithosphere. Suppose there is a region of dipole layers with the same dipole density, m (see Figure 14A). Inside this region the positive and the negative parts of the dipole layers cancel each other except at the boundaries, which remain positive or negative. The dipole density, m, is constant through this region (see Figure 14B) and the density difference, $\Delta\rho$, has 2 discontinuities at the boundaries (see Figure 14C). This means that we can express the density change, $\Delta\rho$, using the dipole density, m, as

$$\Delta\rho = \frac{\partial m}{\partial z} \; ,$$

where z is depth. In general, we are not interested in the absolute

Figure 14. (A) A region of dipole layers. (B) The dipole density, m,
as a function of depth, z, for the distribution of dipole
layers in (A). (C) The density change, $\Delta\rho$, as a function of
depth, z.
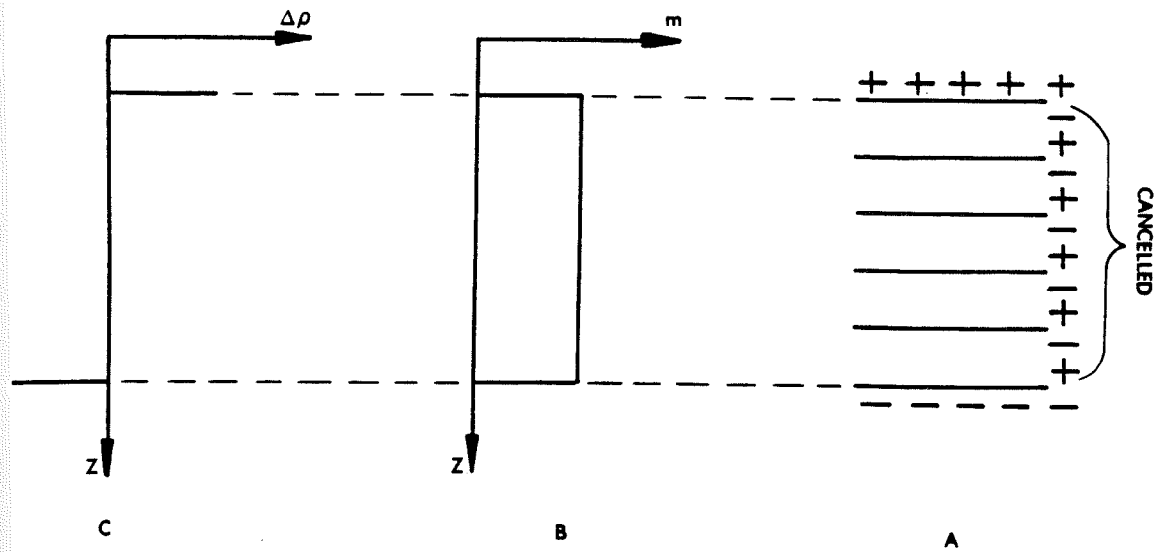
value of the density or the dipole, but in their change relative to some reference which we take to be the oceanic ridge. The density change, $\Delta\rho$, is a function of the temperature, T

$$\Delta\rho = \rho_0\alpha(T_1 - T) = \rho_0\alpha T_1\left[1 - \text{erf}\left(\frac{z}{2\sqrt{\kappa t}}\right)\right] = \rho_0\alpha T_1 \text{ erfc } (p) \qquad (6)$$

where $p = z/2\sqrt{\kappa t}$.

The dipole density, m, is

$$m = \int_p^d \Delta\rho \; dz = 2\sqrt{\kappa t}\alpha T_1\rho_0 \int_p^\infty \text{erfc}(p) \; dp = 2\sqrt{\kappa t}\alpha\rho_0 T_1 \text{ ierfc}(p) \qquad (7)$$

(Lister, 1982) where z is the depth of the bottom of the ocean, and ierfc(p) is the integral error function (Carslaw & Jaeger, 1959, p. 483).

In addition, seawater is displacing the shrinking lithosphere. This causes another set of dipoles because of the density change between the seawater and the lithosphere (see Figure 15). The left side shows the reference density, ρ_0, which is the density of the hot material (see Figure 15A). The model is illustrated in Figure 15B. In the upper part of the model, where seawater is displacing the shrinking lithosphere, the density difference is $\Delta\rho = \rho_0 - \rho_w$, which is

Figure 15. (A) The reference density, ρ_0, of the hot material. (B) Cross section of the model. (C) The dipole density, m, as a function of a dimensionless depth, $y=(z-h)/2\sqrt{\kappa t}$, for the model in (B). (D) The density change, $\Delta\rho$, as a function of a dimensionless depth as in (C).
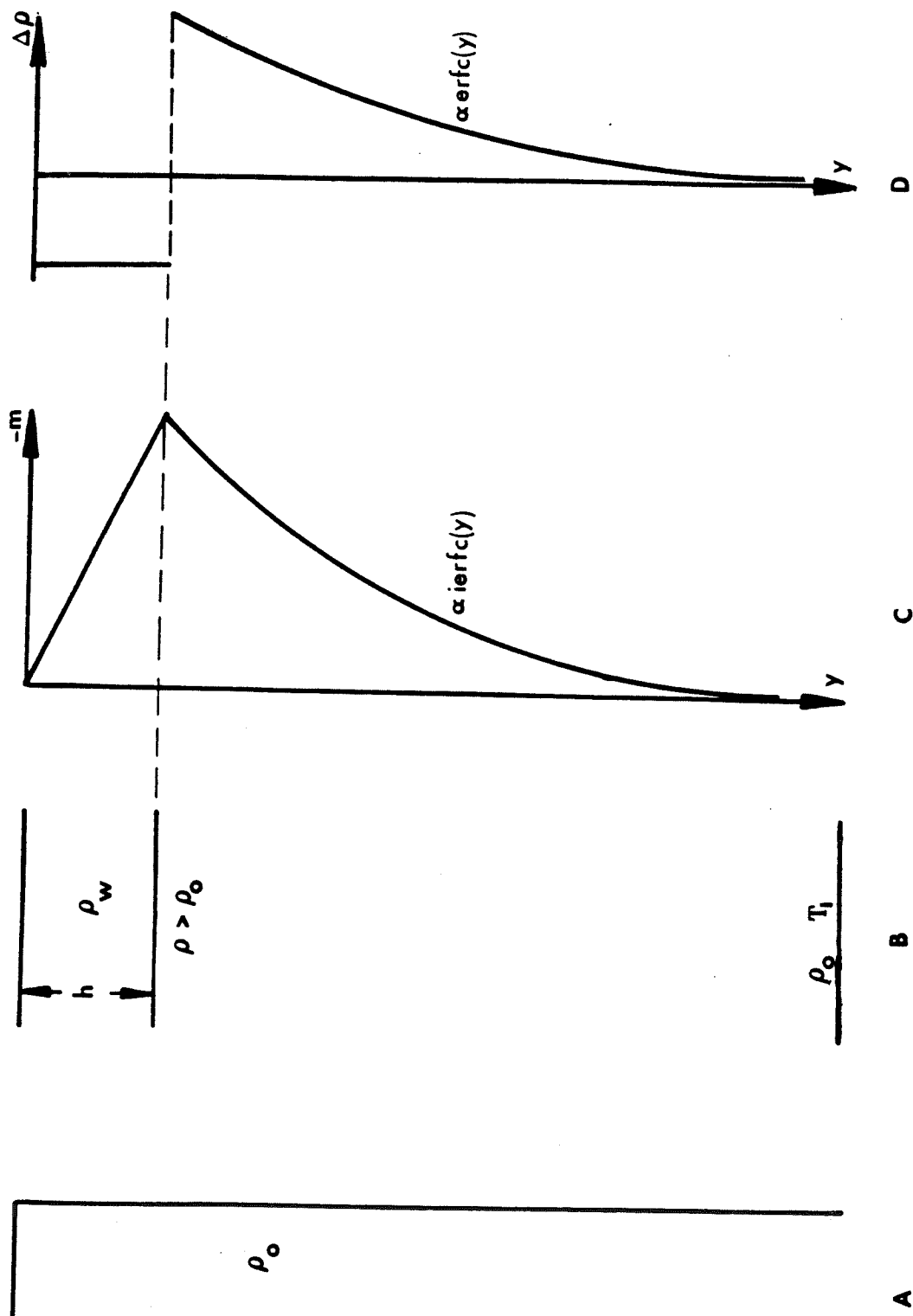
independent of the temperature, T. The dipole density, m, is a function of the depth only

$$m = \int_0^h \Delta\rho \ dz = h \ (\rho_0 - \rho_w) \tag{8}$$

where h is the seafloor topography (see Figure 15C).

We can simplify the calculations significantly, because the thermal dipole everywhere is proportional to $\text{ierfc}[z/2\sqrt{\kappa t}]$, by defining a new dimensionless depth, y (see Figure 15C)

$$y = \frac{(z - h)}{2\sqrt{\kappa t}} \ .$$

The dipole density, m, relative to the ridge crest is, for the upper part where seawater displaced the shrinking lithosphere,

$$m = \int_0^h \Delta\rho \ dz = 2\sqrt{\kappa t} \int_{p_1}^0 \Delta\rho \ dy = -h \ (\rho_0 - \rho_w) \qquad , \ p_1 \leq y \leq 0,$$

where $p_1 = -h/2\sqrt{\kappa t}$. For the lower part, we find that the thermal dipole, m, relative to the ridge crest, is

$$m = -2\sqrt{\kappa t}\alpha\rho_0 T_1 \ \text{ierfc}(y) \qquad , \ 0 \leq y \leq (d-h)/2\sqrt{\kappa t},$$

where d is the reference surface depth. Figure 15D illustrates the density difference as a function of a dimensionless depth, y. In the upper part of the model the density difference is $\Delta\rho=\rho_0-\rho_w$, which is independent of the temperature, T. The lower part of the model is defined in Equation 6.

As a simple model, assume there are two ridges along 0° longitude and along 180° longitude. There are two trenches along 90° longitude and along 270° longitude (see Figure 16). The four plates are moving away from the ridge, each with a velocity of 0.05 m/yr at the equator. The motion of the plates is bounded between latitudes 87°N and 87°S; in other words, there is no motion close to the north and south poles, so that their contributions to the dipole density is assumed to be zero. The longitude, ϕ, of any point is expressed as a function of the cooling lithosphere age, t, $\phi=\omega t$, where ω is the angular velocity; the age along a given longitude is the same. In this model we use κ, α, ρ_0, and T_1 which are 65×10^{-8} m²/sec, 3.1×10^{-5} °C^{-1}, 3300 kg/m³, and 1400°C, respectively (Lister, 1982).

We use the ring method to calculate the dipole effect. For each observation point a set of 18 rings is defined and the observed geoid anomaly, Y_{ij}, is defined as the value at the observation point, i, due to the dipole density at ring j (see Figure 17). Assuming symmetry, we need to calculate the dipole effect only at observation points that are on "one side" of the planet, because we receive the same results for the other side. The coordinates of the observation points are

Figure 16. Geometry of the test model. The ridges are along 0° and
180° longitudes and the trenches are along 90° and 270°
longitudes. The age along a given longitude is the same.
The dots inside each spherical triangle or trapezoid are
the observation points.
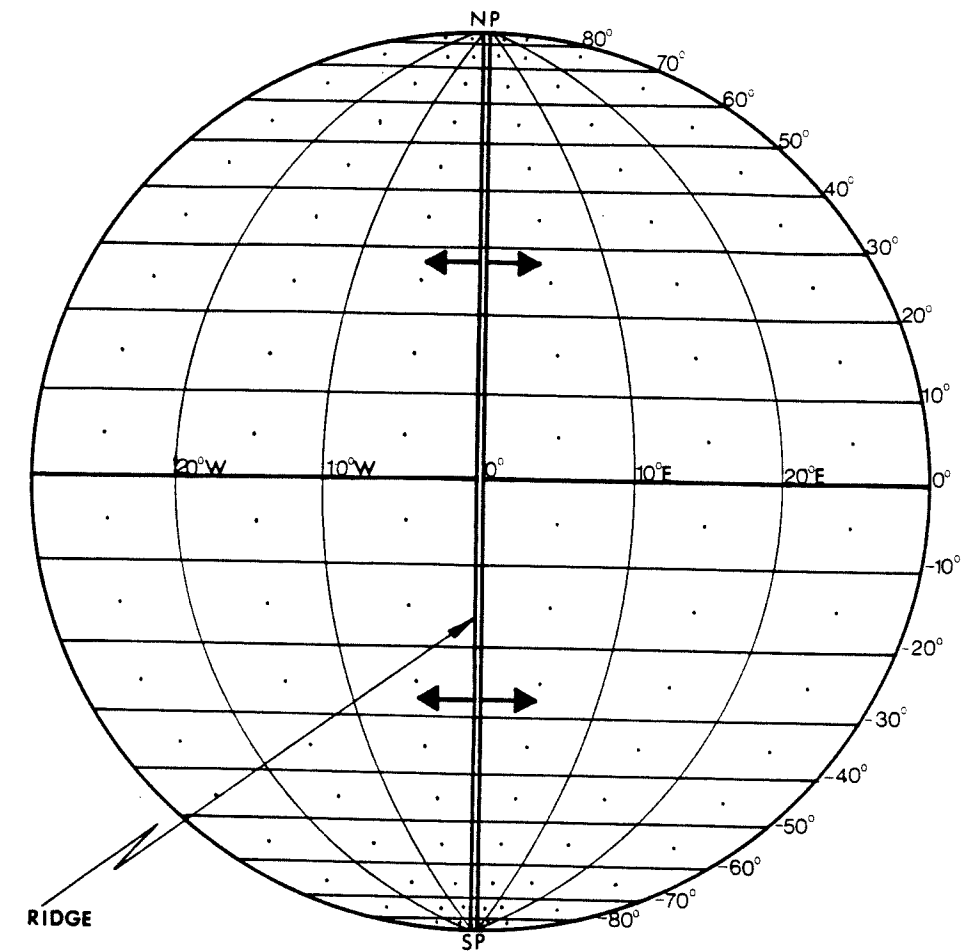
Figure 17. A set of 18 rings which covers the whole test planet is defined for each observation point, O.
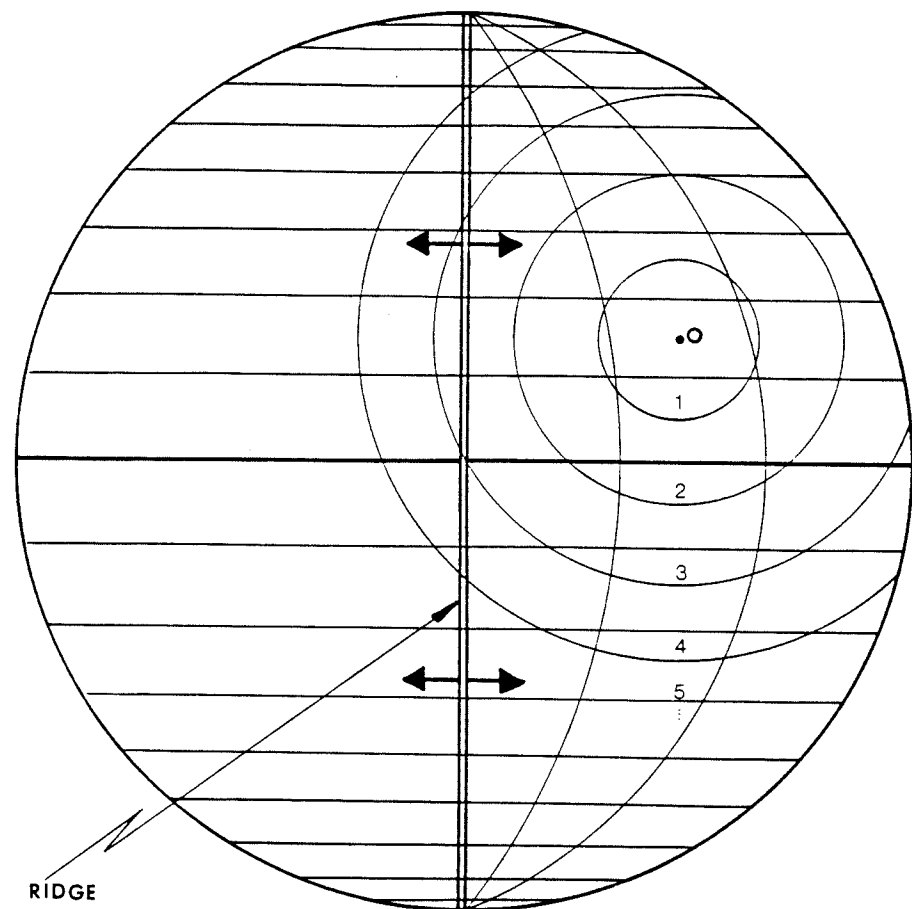
expressed by the equations

$$\Phi = \frac{\pi}{18}(k - \frac{1}{2}) \qquad\qquad , k=1,2,3\ldots.18,$$

and

$$\Theta = \frac{\pi}{18}(n - \frac{1}{2}) \qquad\qquad , n=1,2,3\ldots.18,$$

where Θ is a latitudinal angle measured from the north pole ($0 \leq \Theta \leq \pi$), and Φ is the longitude ($0 \leq \Phi \leq \pi$). Each ring is divided into 36 small spherical triangles or trapezoids (see Figure 18). The dipole density value at each centroid of a given spherical triangle or trapezoid represents the dipole density for the whole triangle or trapezoid. Figure 19 illustrates a cross section of the test planet. For each ring we define 36 columns, with a spherical triangle or a spherical trapezoid base, starting at a depth of 0 km continuing to a depth of 200 km. Each column is divided into 20 bins with a thickness of 10 km each, except for the first and the second bins; the thickness of the first bin is h (km), and the thickness of the second is 10-h (km). Figure 20 illustrates plots of the dipole density, m, with the bins. In a similar way we can plot the density difference, $\Delta\rho$, with the bins.

In the geoid calculation we use the average dipole density, $\bar{m}$, for

Figure 18. Each ring is divided into 36 spherical triangles or trapezoids. O - Observation Point.
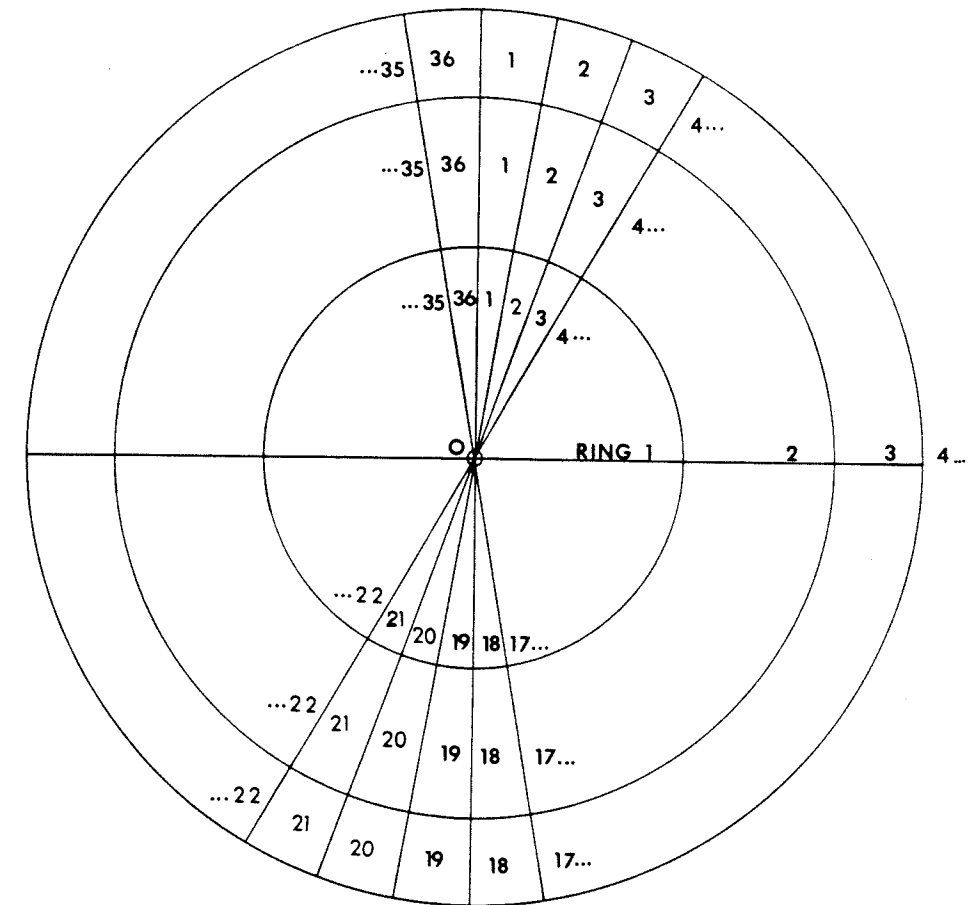
Figure 19. A cross section of the planet that illustrates the ring
method and the division into bins. O - Observation Point, C
- Center of the planet.
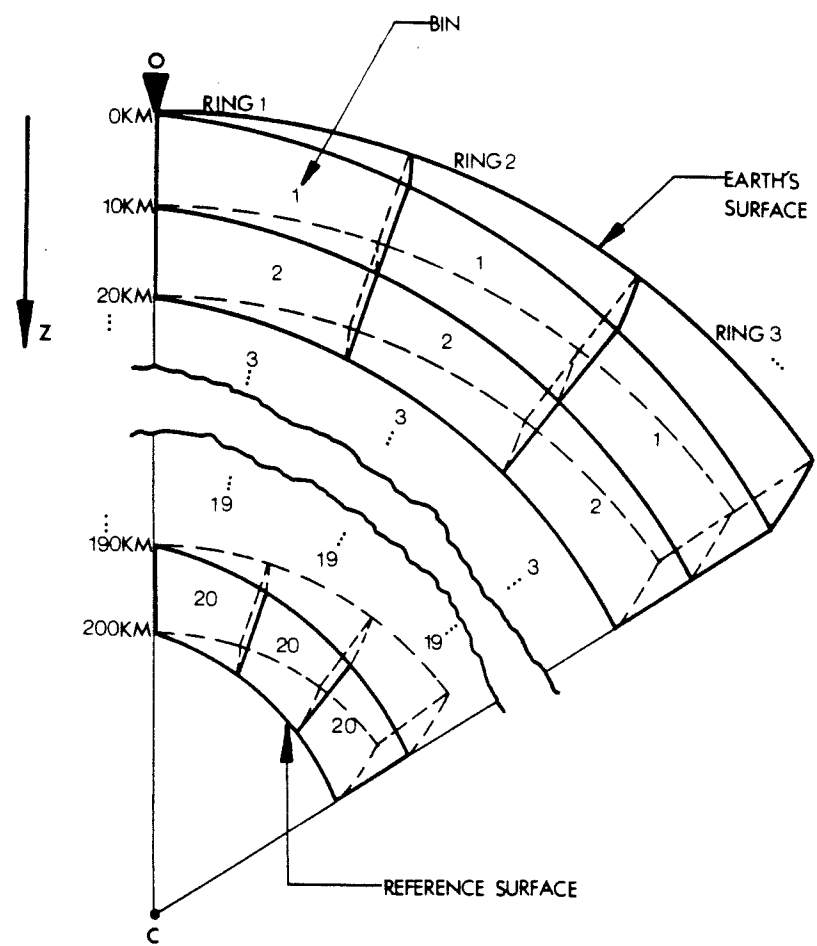
Figure 20. Plots of the bins with the dipole density, m, as function
of depth, z, for a given age.
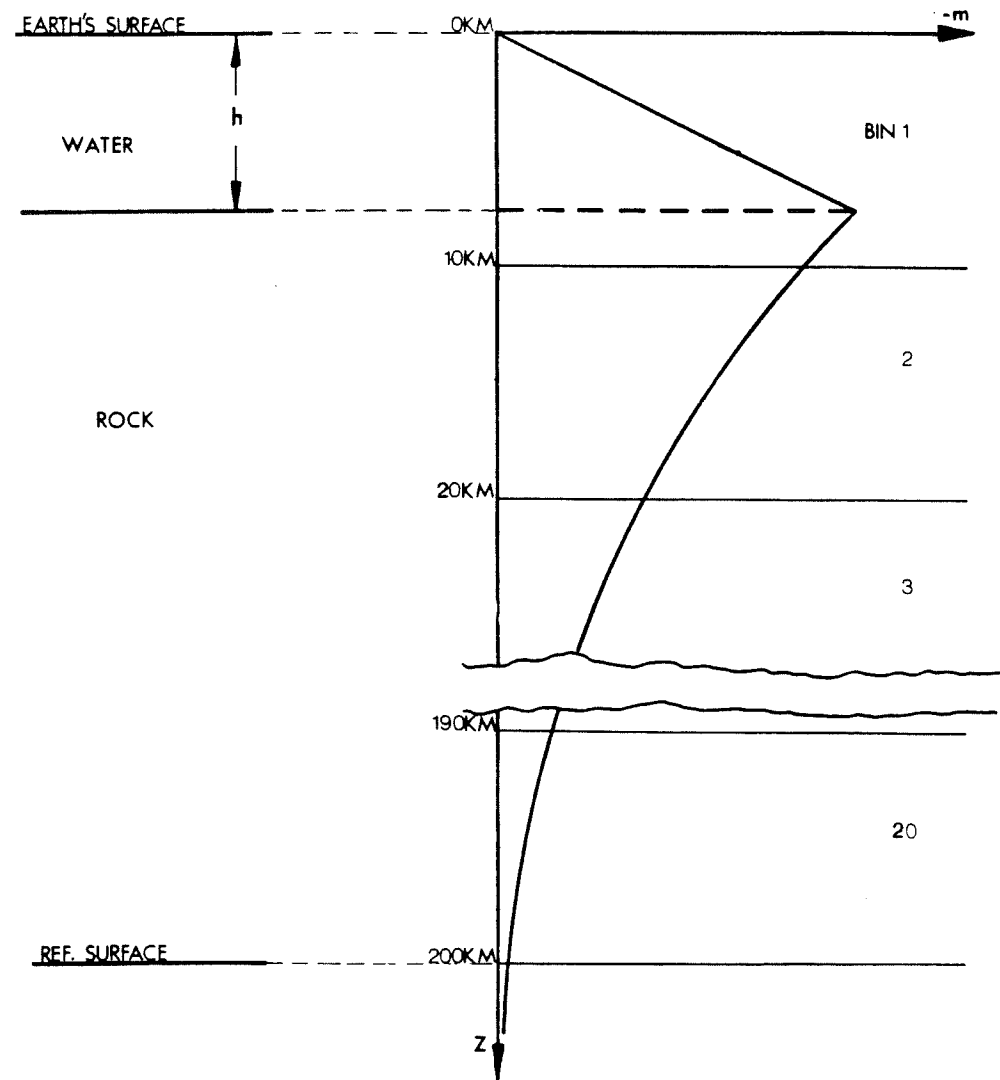
a given bin defined (using Equation 7) as

$$\bar{m} = \frac{1}{\chi} \int m(z)dz = \frac{2\sqrt{\kappa t}\alpha\rho_0 T_1}{\chi} \, i^2 erfc(p) \tag{9}$$

where χ is the thickness of the bin, and $i^2 erfc(p)$ is defined as in Carslaw and Jaeger (1959, p. 484). The dipole density of a given ring is the averaged sum of all the dipole density values of the columns in that ring. Using Equation 6 similarly with Equation 9, we find that the average density change, $\overline{\Delta\rho}$, for a given bin is

$$\overline{\Delta\rho} = \frac{1}{\chi} \int \Delta\rho(z) \, dz = \frac{\alpha\rho_0 T_1}{\chi} \, ierfc(p)$$

where $ierfc(p)$ is the integral error function (Carslaw and Jaeger, 1959, p.483). In order to calculate the density change or the dipole density we need to know the age at the centroid; the method of the age calculation is described in Appendix B.

CHAPTER SEVEN - THE SOURCES OF THE SELF-DEFORMATION EFFECT

Having described the self-deformation process, our next goal is to focus on the causes of this process that creates a large scale geoid anomaly over the test planet. So far, we have assumed that the sources of the geoid anomaly were known. We can identify three effects that create the initial signal over the geoid: the dipole effect (Lister, 1982), the pie-shaped column effect (Vening Meinesz, 1946) and the dependence of the gravitational acceleration on depth (Vening Meinesz, 1946). Although we define three separate components, they all share a common source: the mass dipole due to density differences in the cooling lithosphere (Lister, 1982). The initial geoid anomaly is the sum of these three effects.

7.1 THE DIPOLE EFFECT

The geoid anomaly observed at the planet's surface due to mass dipole at the j-th ring is

$$Y = \int_0^d \int_0^{2\pi} \int_{\theta_j'}^{\theta_j''} \frac{G\bar{m}l(R - z)^2 \sin\theta \, d\theta \, d\phi \, dz}{g(q^2 + 1^2)^{3/2}} \quad , \tag{10}$$

where R is the radius of the test planet, z is the depth, d is the reference surface depth, q is q=R sin θ , l is l=R(1-cos θ)-z, and $\bar{m}$ is the average dipole density, as was defined above (Lister, 1982; see Figure 21A). The range of θ is $\theta_j' \leq \theta \leq \theta_j''$ and the range of ϕ is $0 \leq \phi \leq 2\pi$. Substitution of l and q in Equation 10 yields

$$Y = \int_0^d \int_0^{2\pi} \int_{\theta_j'}^{\theta_j''} \frac{G\bar{m}(z - 2R \sin^2(\theta/2))(R - z)^2 \sin\theta \, d\theta \, d\phi \, d}{gz[z^2 - 4Rz \sin^2(\theta/2) + 4R^2 \sin^2(\theta/2)]^{3/2}} \quad . \tag{11}$$

Observation points above the equator of the dipole "see" a positive contribution to the geoid anomaly, while those below receive a negative contribution (Lister, 1982). Away from the observation point we find that once we pass the equator, the negative contribution tends to reduce the local effect. This means that the local effect is important. Setting z=0 gives an estimate of the far field effects

64

Figure 21. Dipole effect - (A) Geometry for the geoid anomaly observed
          at the planet's surface due to a spherical shell of mass
          dipole. O - observation point. (B) The same as (A) but the
          observation point, O, is at the reference surface.
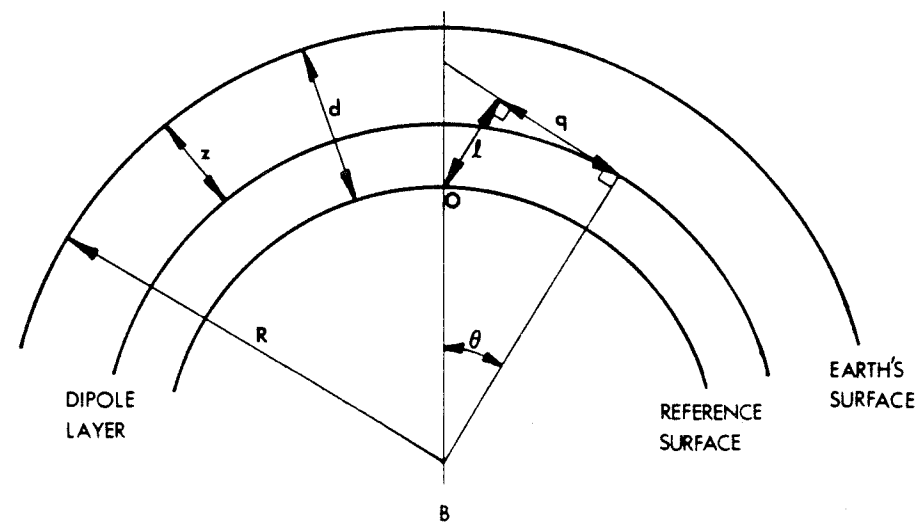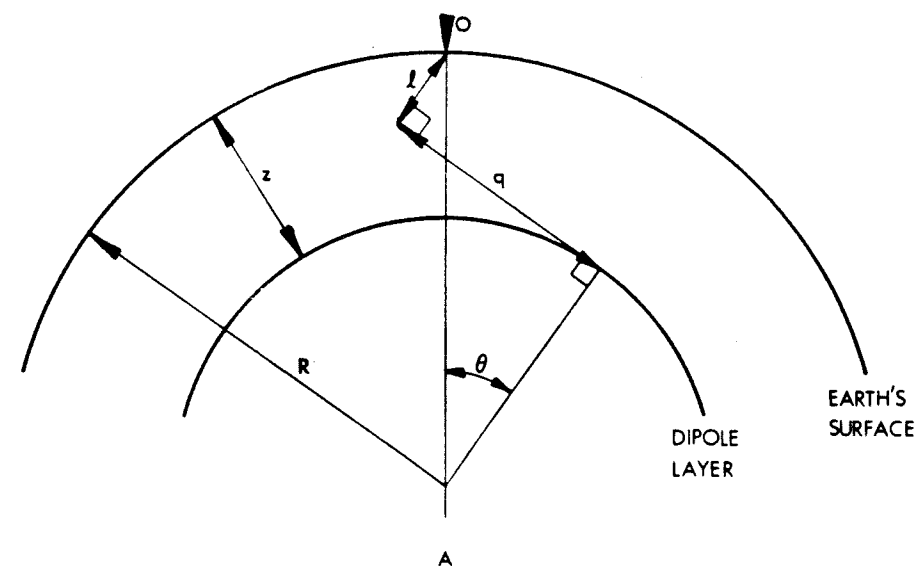
which is a negative summation

$$\gamma = \int_0^{2\pi} \int_{\Theta_j'}^{\Theta_j''} \frac{-G\bar{m}}{2g} \cos(\Theta/2)\ d\Theta\ d\phi = \frac{-2G\bar{m}\pi}{g} \left[\sin\left(\frac{\Theta_j''}{2}\right) - \sin\left(\frac{\Theta_j'}{2}\right)\right] .$$

The geoid anomaly observed at the reference surface due to a ring of mass dipole is (see Figure 21B)

$$\gamma = \int_0^d \int_0^{2\pi} \int_{\Theta_j'}^{\Theta_j''} \frac{G\bar{m}l(R - z)^2 \sin\Theta\ d\Theta\ d\phi\ dz}{g(l^2 + q^2)^{3/2}} \tag{12}$$

where d is the reference surface depth, q is

$$q = (R - d)\sin\Theta ,$$

and l is

$$l = (R - z) - (R - d)\cos\Theta .$$

Substitution of l and q in Equation 12 yields

$$\gamma = \int_0^d \int_0^{2\pi} \int_{\Theta_j'}^{\Theta_j''} \frac{G\bar{m}\left[(R - z) - (R - d)\cos\Theta\right](R - z)^2 \sin\Theta\ d\Theta\ d\phi\ dz}{g[(R - z)^2 + (R - d)^2 - 2(R - z)(R - d)\cos\Theta]^{3/2}} . \tag{13}$$

In this case we are always below the dipole equator, therefore the contribution is always negative.

7.2 THE PIE-SHAPED COLUMN EFFECT (THE ISOSTATIC MASS EFFECT)

Once a mass dipole is introduced, an effect due to the pie shape of each column also contributes to the geoid anomaly. If topography is elevated, and the mass dipole is positive upward, the volume of positive density change is greater than that of negative change. The extra mass that this implies causes a further uplift of the outer geoid, but also an uplift of the reference surface that is opposed to the dipole effect. Figure 15D illustrates the density change, $\Delta\rho$, as a function of depth. The geoid anomaly observed at the planet's surface is

$$\gamma = \frac{G}{g} \int_0^d \int_0^{2\pi} \int_{\theta'_j}^{\theta''_j} \frac{\Delta\rho(R - z)^2 \sin\theta \; d\theta \; d\phi \; dz}{\eta}$$

$$= \frac{G}{g} \int_0^d \int_0^{2\pi} \int_{\theta'_j}^{\theta''_j} \frac{\Delta\rho(R^2 - 2zR + z^2) \sin\theta \; d\theta \; d\phi \; dz}{\eta}$$

where d is the reference surface depth,

$$\eta = (1^2 + q^2)^{1/2},$$

$$1 = R - (R - z) \cos \theta,$$

and

$$q = (R - z) \sin \theta,$$

as shown in Figure 22A. Substitution of 1 and q in the above equation of γ yields

$$\gamma = \int_0^d \int_0^{2\pi} \int_{\theta_j'}^{\theta_j''} \frac{G\Delta\rho(R^2 - 2zR + R^2) \sin \theta \; d\theta \; d\Phi \; dz}{g\left[R^2 - 2R(R - z) \cos \theta + (R - z)^2\right]^{1/2}} . \qquad (14)$$

The first term in the integrand is

$$\frac{G\Delta\rho R^2 \sin \theta}{g\left[R^2 + (R - z)^2 - 2R(R - z) \cos \theta\right]^{1/2}}$$

which is a weak function of z. Close to the observation point where $(z,\theta)=0$ the integrand vanishes. Actually, this term is approximated by $R\int\Delta\rho \; dz$ which is negligible. Since $2zR \gg z^2$ the integral is almost

Figure 22. As Fig. 21 but for the mass sheets induced by the pie-shape
of the columns.
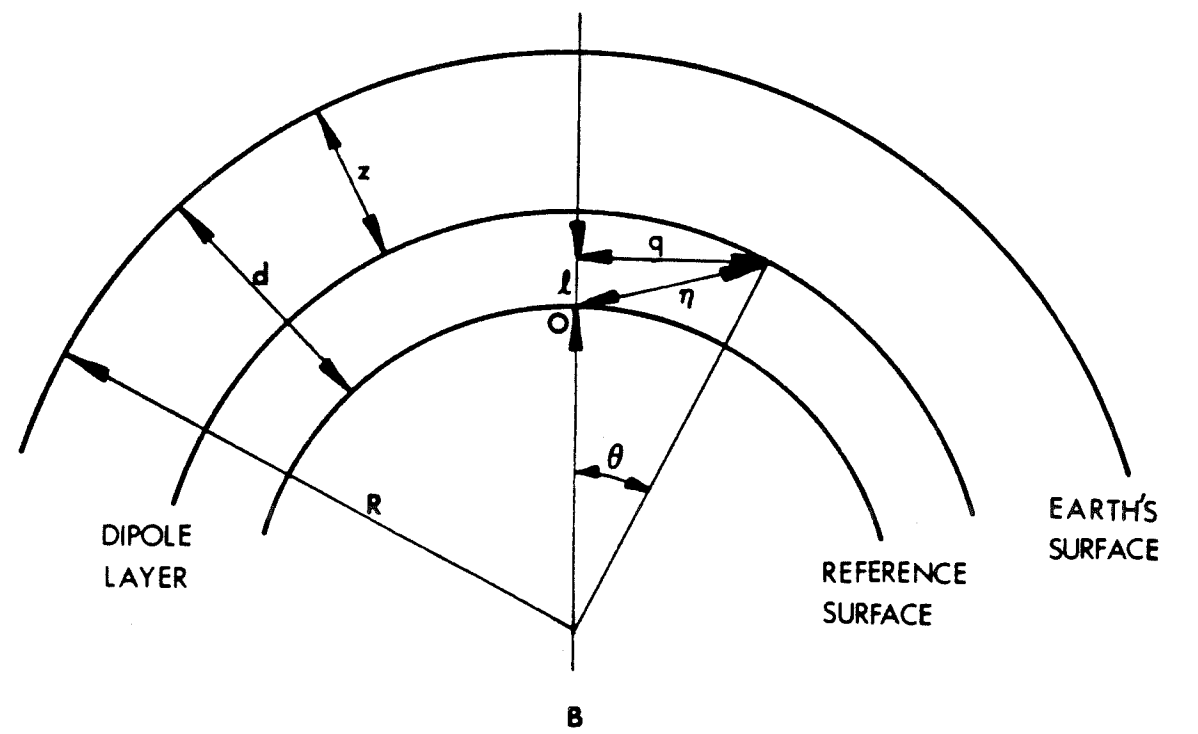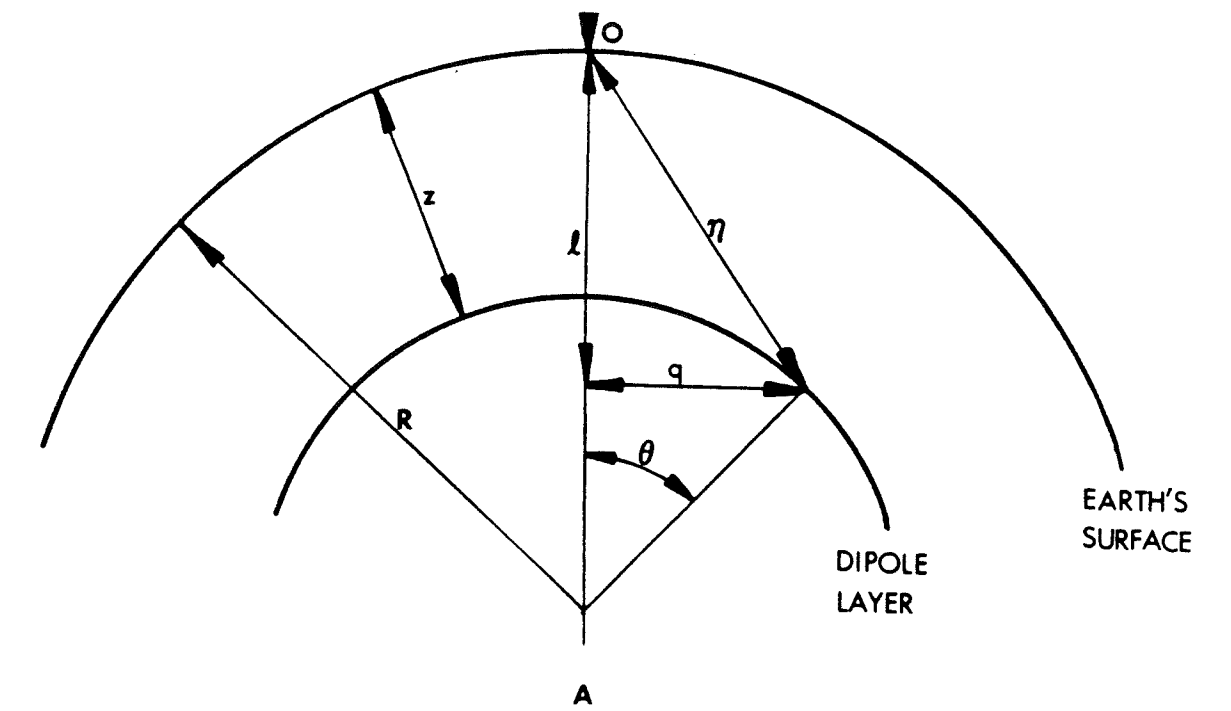
equal to

$$\gamma = \int_0^d \int_0^{2\pi} \int_{\Theta'_j}^{\Theta''_j} \frac{2G\Delta\rho Rz \ \sin\Theta \ d\Theta \ d\phi \ dz}{g\eta} \qquad (15)$$

The term $2z/R$ is the change in the cross section because of sphericity, and the mass gain is

$$\text{mass gain} = \int \frac{2z}{R} \ Wp \ dz$$

The near field effect is of a minor nature, while the far field effect is important. Similarly, we obtain the geoid observed at the reference surface

$$\gamma = \int_0^d \int_0^{2\pi} \int_{\Theta'_j}^{\Theta''_j} \frac{2\Delta\rho GRz \ \sin\Theta \ d\Theta \ d\phi \ dz}{g\eta} \qquad (16)$$

where d is the reference surface depth,

$$\eta = (1^2 + q^2)^{1/2},$$

$$1 = (R - z) \cos\Theta - (R - d),$$

and

$$q = (R - z) \sin \Theta ,$$

as shown in Figure 22B. Substitution of l and q in Equation 16 gives

$$\gamma = \int\limits_{0}^{d} \int\limits_{0}^{2\pi} \int\limits_{\Theta_j'}^{\Theta_j''} \frac{2G\Delta\rho Rz \sin \Theta \, d\Theta \, d\phi \, dz}{g[(R - d)^2 - 2(R - d)(R - z) \cos \Theta + (R - z)^2]^{1/2}} , \quad (17)$$

and again, the far field is important.

7.3 THE DEPENDENCE OF THE GRAVITATIONAL ACCELERATION ON DEPTH

The acceleration of gravity, g, is

$$\frac{GM}{R^2}$$

where M is the mass of the test planet. The gradient of the gravitational acceleration is

$$\frac{\partial g}{\partial R} = \frac{\partial}{\partial R} \frac{GM}{R^2} ,$$

or the relative change of the gradient is

$$\frac{1}{g}\frac{\partial g}{\partial R} = \frac{1}{M}\frac{\partial M}{\partial R} - \frac{2}{R} = \frac{4\pi\rho GR}{g}\frac{1}{R} - \frac{2}{R} = \frac{-0.2}{R}$$

where ρ is the density, 3300 kg/m^3. In other words, g increases with depth at a rate of 0.2/R. This causes the amplitude of compensating deep density changes to be smaller. The mass gain (for positive dipole anomaly) is

$$\int \frac{0.2z}{R}\Delta\rho \ dz \ .$$

The increase of g with depth (gravity effect), using "units of pie-shaped column effect", adds 10% to the latter. Throughout this study the gravity effect (g=g(z)) is included in the pie-shaped column effect.

7.4 THE INDIRECT EFFECTS OF ATTRACTED MASS

The above three sections describe all the effects that appear due to the initial dipole and the sphericity of the test planet. The dipole and the mass effects cause further deformation, that can be considered a by-product of the initial mass separation in the

lithosphere. The final geoid or reference surfaces are calculated using, simultaneously, all the direct and indirect effects. Before presenting the final equations, the different types of indirect effect should be discussed.

There are three categories. The first category includes effects which appear because the initially deformed geoid (direct dipole and mass effects) goes through a self-deformation process. The second category includes similar self-deformation, but for the reference surface. Gravitational attraction from mass at the deformed reference surface causes changes in the geoid. Similarly, changes in the geoid deform the reference surface. These deformations, that occur simultaneously, are included in the third category.

Our initial step is to calculate the first category effects. We use the same observation points described in the test model section. The value of the geoid or the reference surface, the sum of the dipole and the mass effects at the centroid of a given spherical trapezoid or triangle, is assumed to be representative for the whole trapezoid or triangle. For each observation point we can draw a set of 18 rings that cover the whole test planet. Averaging the centroid values in a given ring yields the geoid height assigned to the ring. We can justify this averaging using the following arguments. The geoid at the observation point, due to mass at a given ring, is linearily proportional to the amount of mass involved; it is independent of the distance because the distance from the observation point to the ring is the same everywhere. As the geoid is a scalar quantity we should not worry about the distribution of mass, whether it is equal

everywhere along the ring or concentrated at a few sites. A crucial test for this method is to calculate the geoid at several adjacent observation points. Dramatic changes of the calculated geoid from one observation point to another mean instability, and are strongly dependent on the way we choose the observation point. This test was applied to all the different calculations to be described in this section. All of them, without exception, show that the geoid is independent of the observation point site. Following the method of geoid calculation described in the section on extraction of the geoid height, we can obtain the geoid height after the self-deformation process. Figures 23-25 illustrate the geoid and the reference surface due to the first and second category effects.

Each change of the geoid level causes an observed change at the reference surface that also applies in the opposite direction. We need to calculate these changes simultaneously because they cannot be isolated or separated from one other. The geoid anomaly, Γ_{ij}^{rs}, observed in ring i on the geoid, due to a unit of mass at the j-th ring in the reference surface, is given by

$$\Gamma_{ij}^{rs} = \frac{2G\rho_1}{g} \int_0^\pi \int_{\Theta_j'}^{\Theta_j''} \frac{(R - d)^2 \sin\Theta \; d\Theta \; d\Phi}{r_{ij}} \tag{18}$$

where ρ_1 is the initial density (3300 kg/m³), d is the reference surface depth, g is the gravitational acceleration at the geoid (9.8

Figure 23. Elevation of geoid and reference surface (meters) due to the mass effect on a two ridge, two trench, all oceanic planet - (A) Initial anomaly at the reference surface. (B) The geoid after the self-deformation effect. (C) As (B) but for the reference surface. (D) Final geoid.
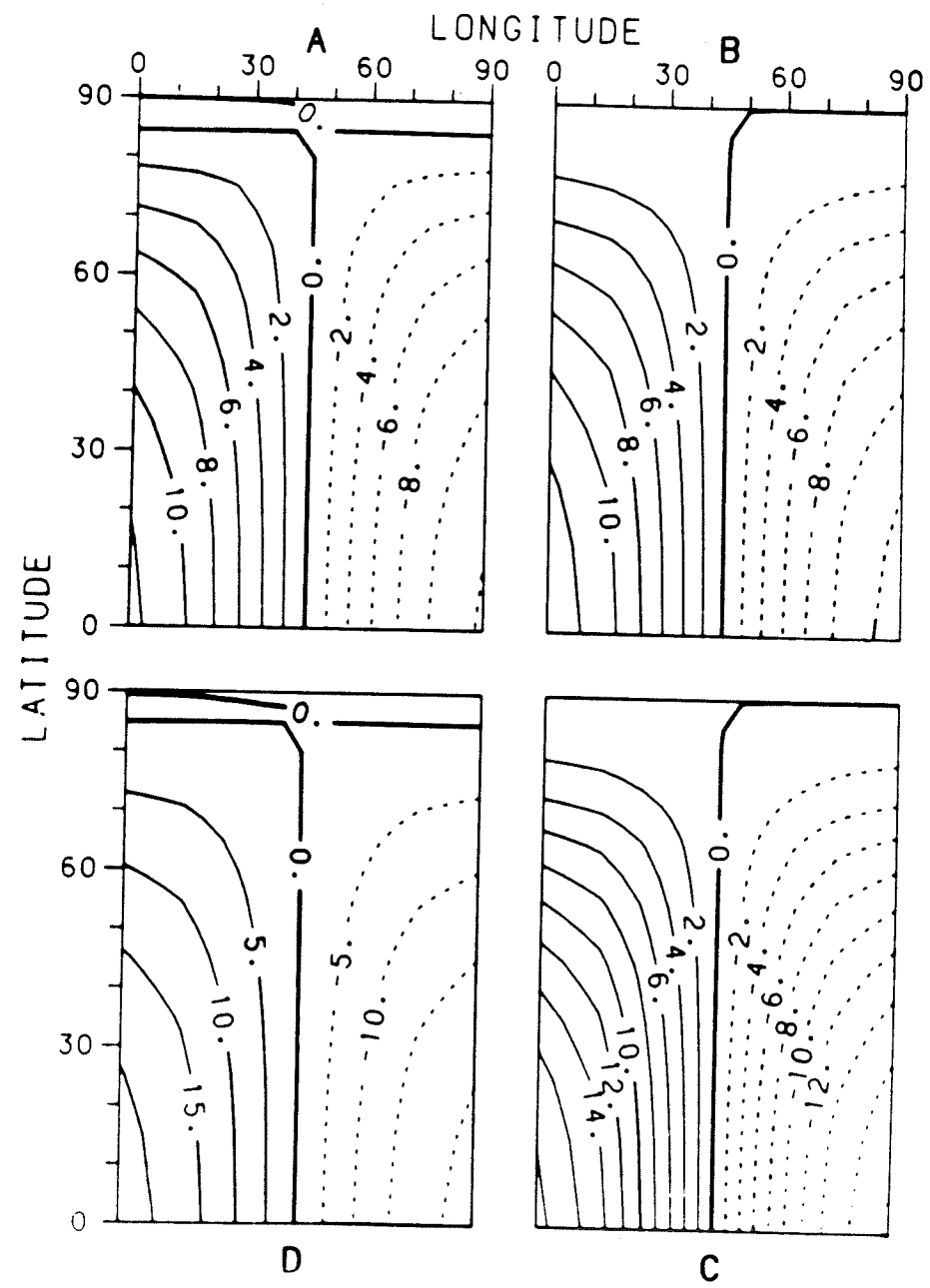
Figure 24. Elevation of geoid and reference surface (meters) due to the dipole effect on the same test planet as Fig. 23 - (A) Initial geoid. (B) Initial reference surface. (C) Final reference surface. (D) Final geoid.
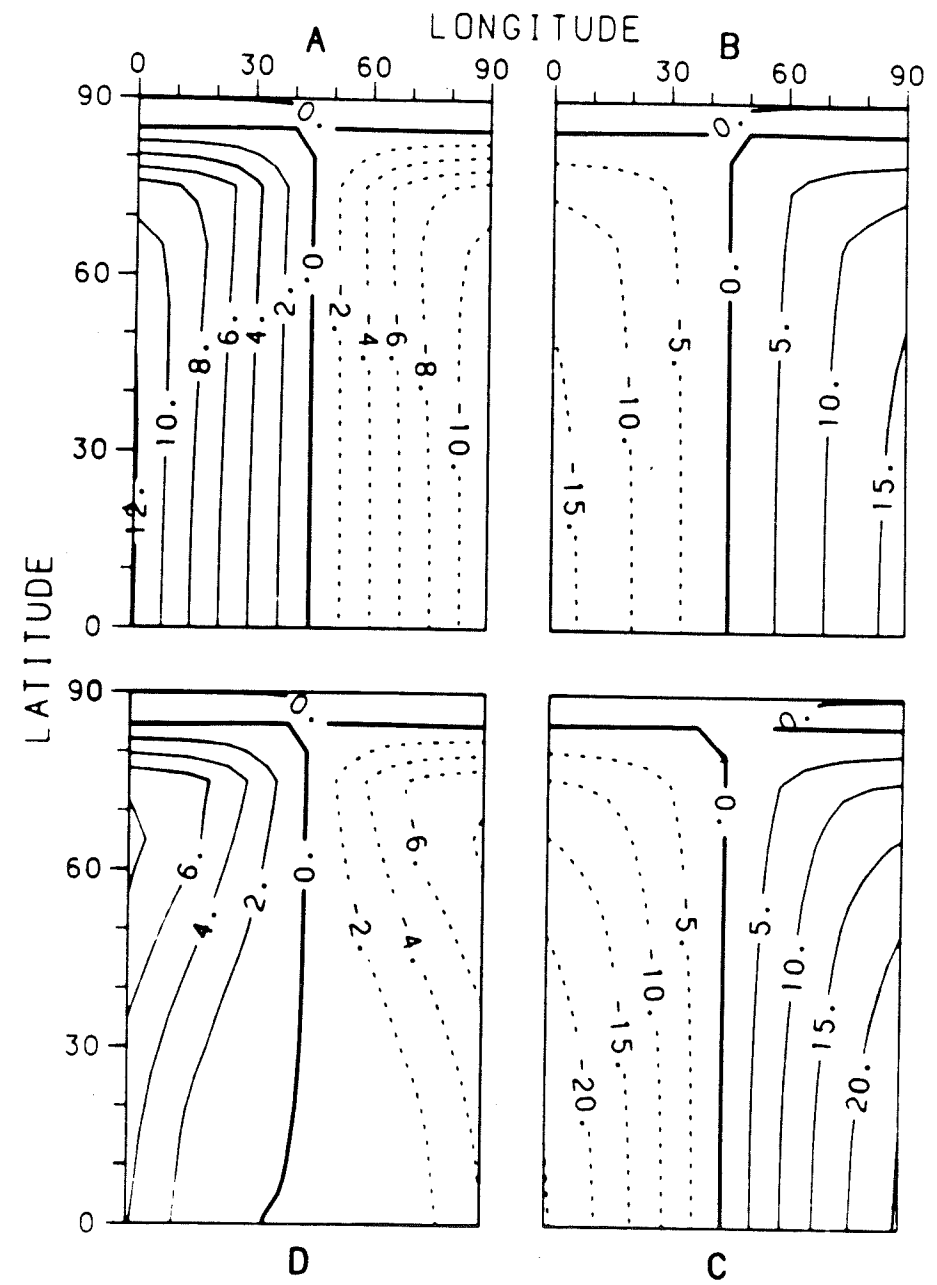
Figure 25. As Fig. 24 but for the combined dipole and mass effects on
the test planet with two ridges at 0° and 180° longitude
and two trenches at 90° and 270° longitude.
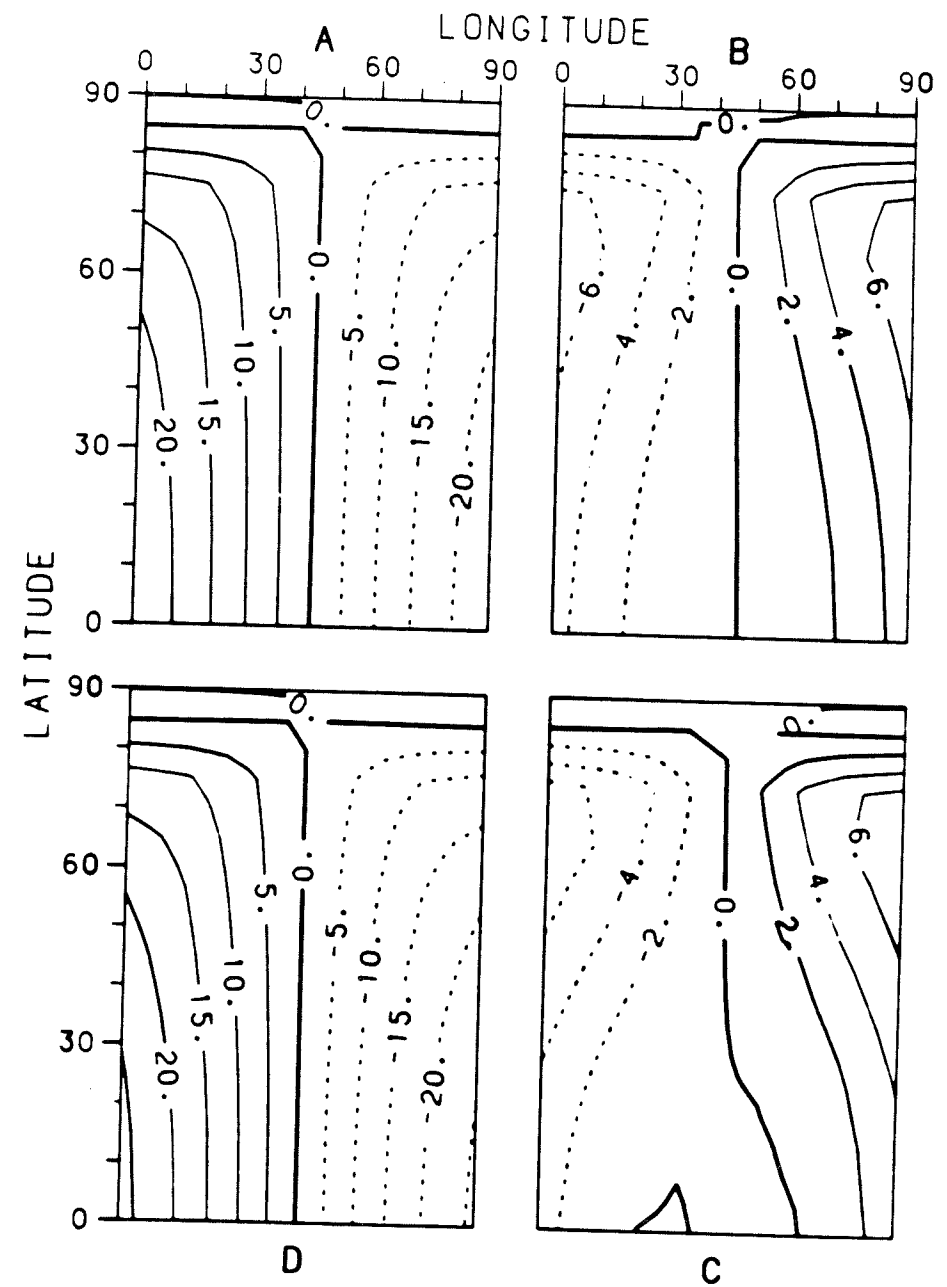
m/sec²), and r_{ij} is the distance between the i-th ring on the geoid to the j-th ring on the reference surface, given by Equation 1. In a similar way, one calculates the anomaly, Γ_{ij}^{sr}, observed at the i-th ring of the reference surface, due to a unit of mass at the j-th ring at the geoid, as

$$\Gamma_{ij}^{sr} = \frac{2G\rho_w}{g_r} \int_0^\pi \int_{\Theta_j'}^{\Theta_j''} \frac{R^2 \sin \Theta \, d\Theta \, d\Phi}{r_{ij}} \tag{19}$$

where r_{ij} is the distance between the observation point at the i-th ring on the reference surface and the j-th ring on the geoid, as given in Equation 1, g_r is the acceleration of gravity at the reference surface,

$$9.8 \left(1 + \frac{0.2d}{R}\right) ,$$

and ρ_w is the seawater density (1030 kg/m³).

7.5 THE FINAL SHAPE OF THE GEOID AND THE REFERENCE SURFACE

The final equations that give the anomalies over the geoid and the reference surface due the initial and self-deformation effects are

$$(s + s')\Gamma^{ss} + (r + r')\Gamma^{rs} = s' \tag{20}$$

for the geoid, and

$$(s + s')\Gamma^{sr} + (r + r')\Gamma^{rr} = r' \tag{21}$$

for the reference surface. The initial anomalies on the geoid and on the reference surface are s and r, respectively. In a similar fashion we define the change in the initial anomalies, due to the self-deformation effect, as s', and r'. The matrix Γ^{ss} was presented in Equation 4, and is the geoid anomaly observed at the i-th ring on the geoid, due to mass at the j-th ring on the geoid, using seawater density. Likewise, we can calculate a similar matrix Γ^{rr}, using the initial density, 3300 kg/m³, for the reference surface; matrices Γ^{rs} and Γ^{sr} were defined in Equations 18 and 19, respectively. The superscripts ss, rr, rs and sr refer to the influence of the first surface (s or r on the left side) on the second surface (s or r on the right side). Appendix C describes the solution of these equations.

The signals due to the mass effect over the geoid or over the reference surface are very similar in the shape and the magnitude, therefore only one is shown (see Fig. 23A). At the reference surface there is a high of up to 12m under the ridge, and a low of up to -12m under the trench; slightly smaller values are obtained for the geoid. At the geoidal surface there is a small change of the initial signal of up to 1m, due to the self-deformation effect where seawater density is 1030 kg/m^3. On the other hand, the same process causes a large change of up to 5m at the reference surface, because the density is 3300 kg/m^3 (see Fig. 23B and Fig. 23C). The final geoid signal due to the mass effect is illustrated in Fig. 23D; at the reference surface we observe a very similar pattern with slightly higher values. It is obvious that the multiple influences (geoid on the reference surface and back) yield final value along the ridge or the trench which is significantly different from the initial signal by up to 9m, but the pattern remains.

The geoid topography due to the dipole effect is opposite to that of the reference surface signal. Along the ridge there is a geoidal elevation of up to 12m, but at the the reference surface a low of up to -16m. Over the trench this effect produces a geoidal low of up to -11m, while a high of up to 16m at the reference surface (see Fig. 24A and Fig. 24B). Consequently, both the final geoid and the final reference surface are lowered down by up to 7m and lifted by up to 8m along the ridge and the trench, respectively (see Figs. 24C and 24D).

The source of the combined dipole and mass effects over the geoid and the reference surface is illustrated in Figs. 25A and 25B. Because

the dipole effect is larger than the mass effect at the reference surface we observe a depression under the ridge and an uplift under the trench. The final geoid surface is up to 6m higher and lower than the initial surface along the ridge and the trench, respectively. At the reference surface there are small changes of up to 2m relative to the initial surface and in the opposite direction to the final geoid.

7.6 CONCLUSION OF THE TEST MODEL

The test model was calculated for two reasons. The first one and the most important is to test the ring method, namely, to check if we get reasonable results, and to examine their validity. This is relatively easy in the test planet's case because it is highly symmetric unlike the real earth. The second reason is that the test model prepares us for the real earth's case. We need to have some modifications of the algorithm for the real earth's case.

CHAPTER EIGHT - APPLICATION OF THE REAL EARTH MODEL

8.1 MODEL CONSIDERATION

So far, we have checked and tested our algorithm on a test planet model. In this chapter we focus our attention on building a model that describes the geoid produced by lithospheric mass distributions over the earth. The case of the real earth is more complicated than the test planet for two major reasons. The first reason is the presence of continents; this means that there is a vast mass dipole covering about 39% (including continental shelves) of the surface of earth, and that varies in size as the height changes from continental shelves to mountain ranges. The second reason is the lack of symmetry. Unlike the previous model, there are more than four plates in the real earth, and the distribution of the continents and oceanic plates is irregular. In fact, the continental area to oceanic surface ratio in the northern hemisphere is higher than that of the southern hemisphere.

The final geoid and the deformation of the reference surface in the earth are caused primarily by two lithospheric components: the cooling oceanic lithosphere and the continents. Let us discuss first the contribution of the cooling lithosphere. The source of the age data is the bedrock geology map of the world (Larson et al., 1985).

This map illustrates the outcrop age in the ocean basins (see Figure 26). The ocean bottom is divided into 10°x10° spherical trapezoids between the longitudes 0°, 10°, ..., 180° (E and W) and latitudes 90°N, 80°N, ..., 0°, ..., 90°S. To each centroid of a spherical trapezoid or triangle we assign an age. An additional layer of basalt (thickness of 5 km and density of 3000 kg/m³; see Figure 27) overlays the oceanic lithosphere. The layer is assumed to be faulted enough (high permeability) to be cooled completely by hydrothermal circulation, with a negligible temperature drop compared to the conductive cooling of the oceanic lithosphere below (see Figure 27). Topography agrees remarkably well with the boundary-layer cooling model to an age of about 100 my (Davis and Lister, 1974), and seems to flatten thereafter over vast areas (see Figure 28). One of several possible explanations of the flattening of seafloor is contamination by hotspots (Crough, 1978; Heestand and Crough, 1981). We model the flattening by assigning an age of 100 my for all those areas which contain older rocks, so the maximum seafloor topography is less than 3.4 km below the oceanic ridge.

As in the test planet case, we are interested in the dipole density change, Δm, relative to the oceanic ridge, caused by the density change, $\Delta \rho$. The density difference between the seawater displacing shrinking lithosphere away from the oceanic ridge, ρ_w, and the oceanic crust at the ridge (the basaltic layer), ρ_B, is $\Delta \rho_1 = \rho_B - \rho_w$. The density difference between the oceanic crust away from the ridge

83

Figure 26. Age of ocean basins in my as obtained from Larson et al. (1985).
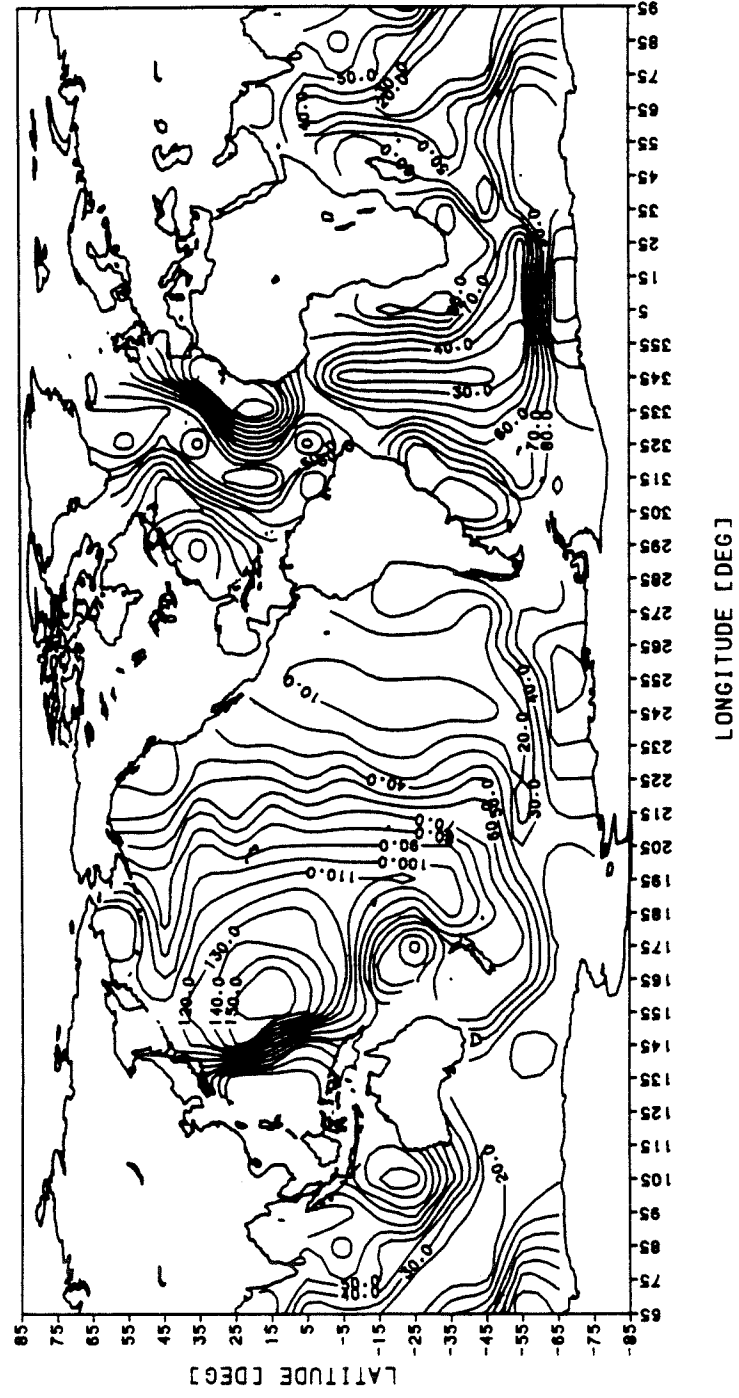
Figure 27. A density model of the real earth for isostatic geoid anomalies calculations, based on the boundary layer model (Davis and Lister, 1974), where ρ_c is the continental density 2800 kg/m³, d is the continental thickness, $(dt/dz)_c$ is the continental thermal gradient, ρ_1 is reference surface density under the continental lithosphere, 3300 kg/m³, ß is 202.5x10³ m, T! is the reference surface temperature, y is the continental elevation above the mean sea level, ρ_w is the seawater density, 1030 kg/m³, d_1 is the seawater layer thickness, 2500 m, h is seafloor topography relative to the oceanic ridge, d_B is the basaltic layer thickness, 5000 m, ρ_B is the basaltic layer density, 3000 kg/m³, ρ_0 is the reference surface density under the oceanic lithosphere, 3320 kg/m³, and z increases downwards .

85
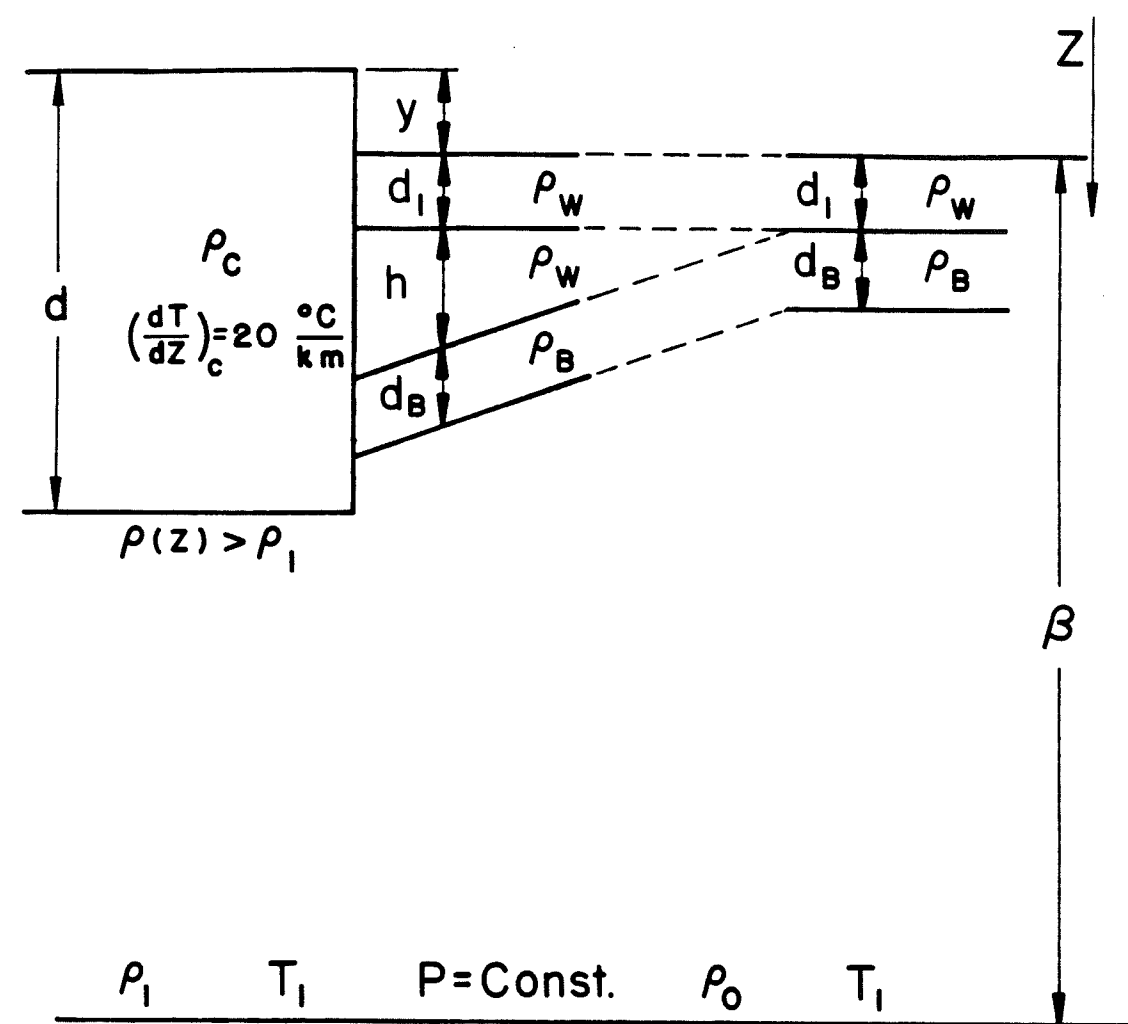
Figure 28. Depth of ocean basins in meters as obtained from Smith et al. (1966).
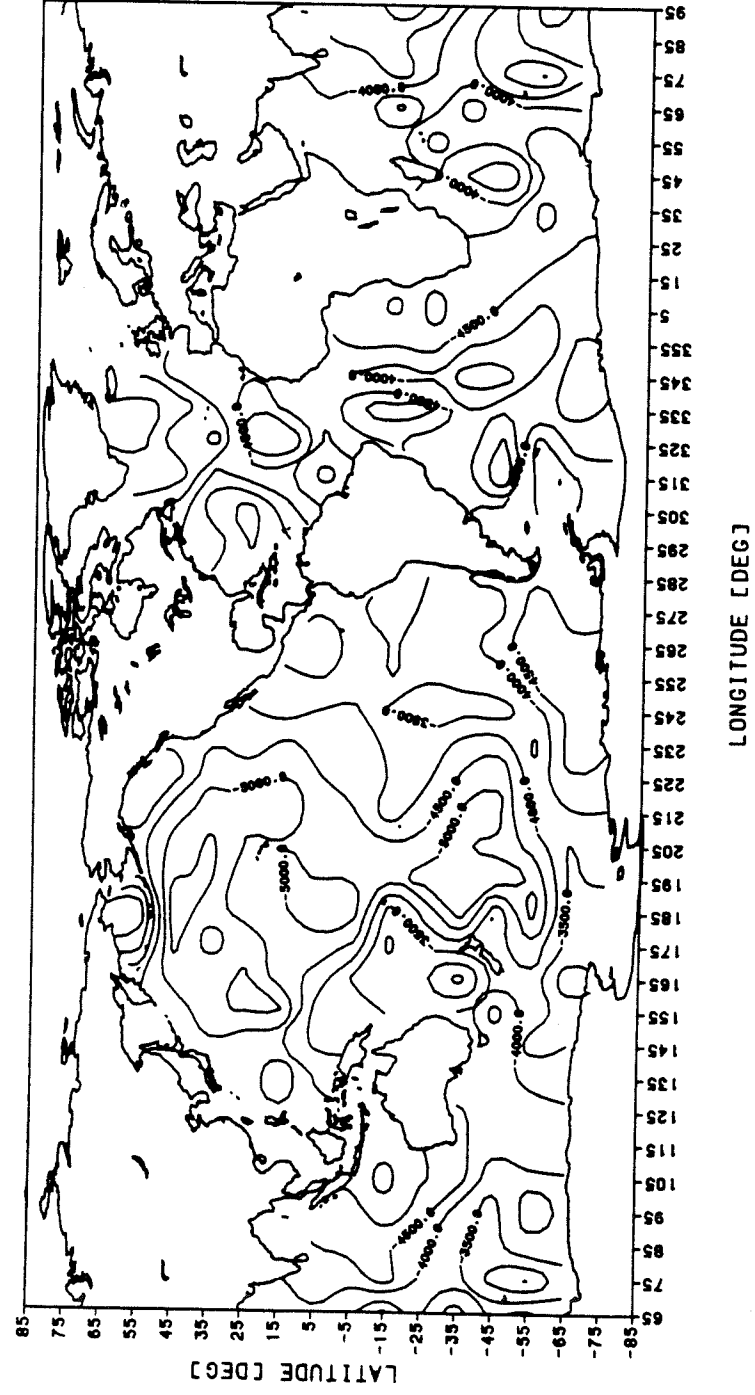
and the mantle material at the ridge, ρ_o, is $\Delta\rho_2 = \rho_o - \rho_B$ (see Figure 29). The overlapping part of the oceanic crust at the ridge and away from the ridge does not contribute because the density change is zero. The dipole density change due to the shrinking lithosphere and the lowered oceanic crust is

$$\Delta m = \int_0^h \Delta\rho_1 \, dz + \int_{d_2}^{d_2+h} \Delta\rho_2 \, dz = \int_o^h (\rho_B - \rho_w)dz + \int_{d_2}^{d_2+h} (\rho_o - \rho_B)dz$$

$$= (\rho_o - \rho_w)h$$

as in Equation 8, and the origin is set at the ridge crest. The dipole density for the rest of the column is obtained by using Equation 9.

The second component is the contribution of the continents. In this case instead of age, as for the ocean basin, we use the topographic height, which is assigned to each spherical trapezoid or triangle (Fig. 30; Smith et al.,1966). The density of the continent is assumed to be 2800 kg/m^3 everywhere (see Figure 27). The temperature at the reference surface is 1400 $^\circ$c, and the thermal gradient in the crust is 20 $^\circ$c/km, which are close to the values of Ringwood (1975). As partial melting starts at about 900 $^\circ$c, the thermal gradient at the upper mantle from a depth of 45 km downwards is adjusted to be substantially lower, to reach 1400 $^\circ$c at the reference surface. If the thickness of the continent is less than 45 km then the thermal

Figure 29. The dipole density change, m, and the density change, $\Delta\rho$, for a given column in the oceanic lithosphere (second left), relative to the reference ridge (left), with $d_1=2.5$ km, $\rho_w = 1030$ kg/m³, $d_2=5$ km $\rho_b=3000$ kg/m³, and $d_3=195$ km, $\rho_0=3320$ kg/m³, thickness and density of ocean, basaltic layer, and mantle under the ridge, respectively. T_1 is the reference surface temperature, 1400 °C, and h is the subsidence of the oceanic lithosphere.

88
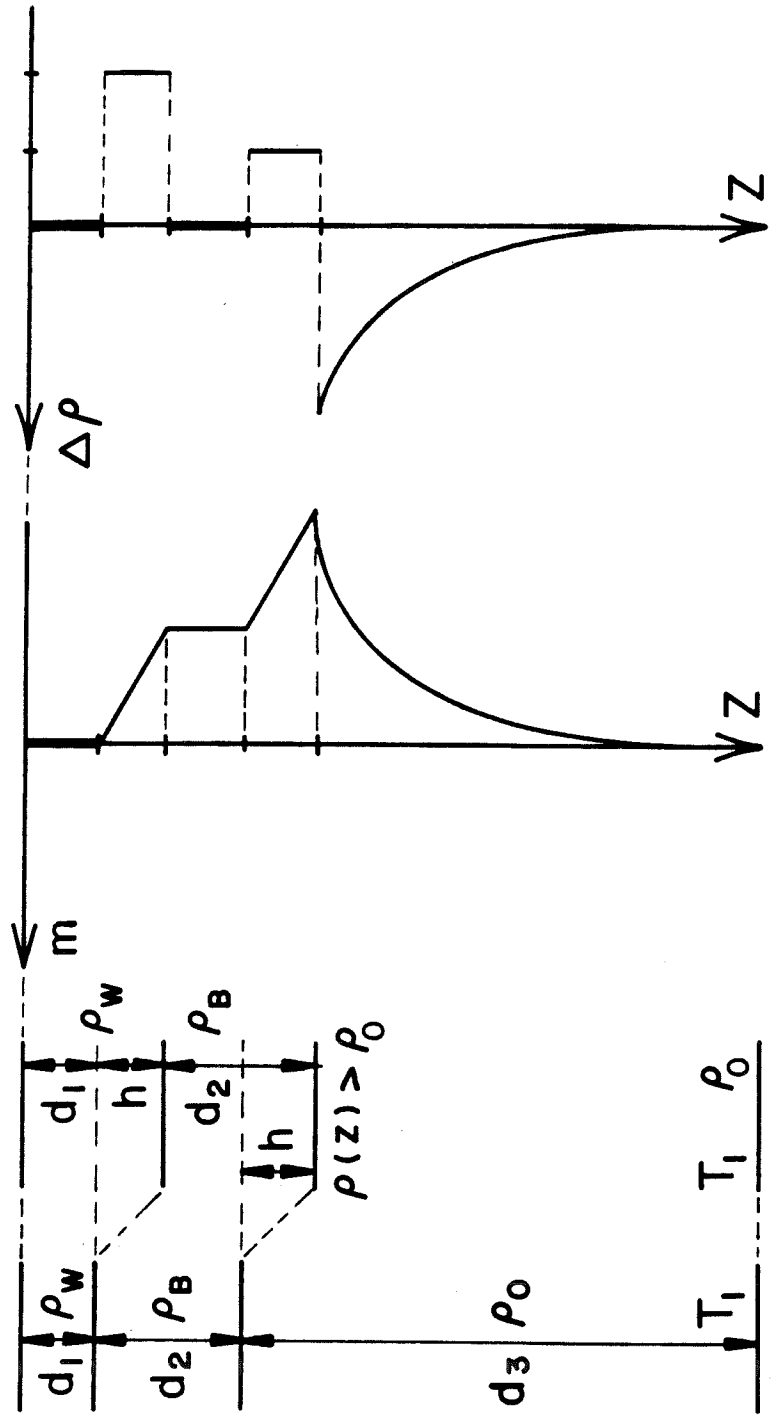
Figure 30. Topography of the continents in meters as obtained from Smith et al. (1966).
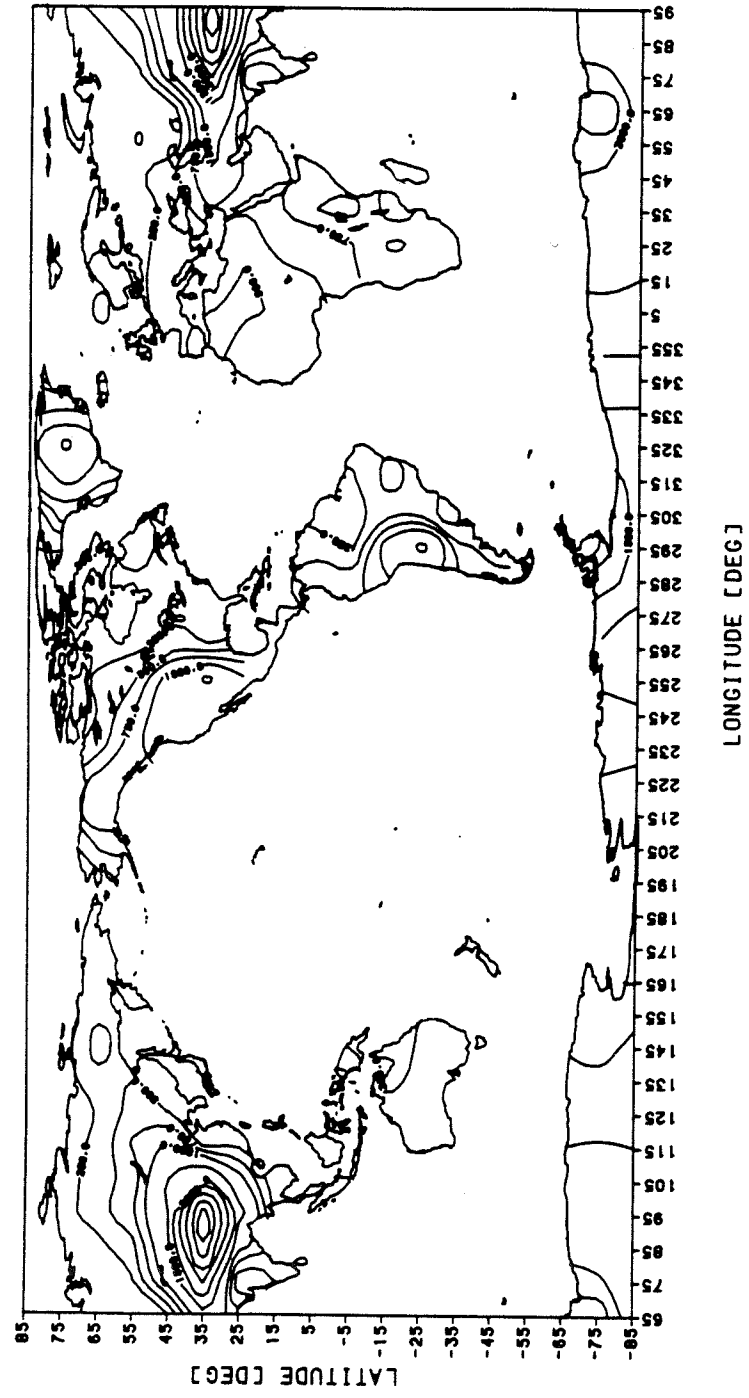
gradient is adjusted for the upper mantle only, with values of about ≈5 °c/km, which are close to values of Clark and Ringwood (1964), and Sclater et al. (1980). Knowing the thermal gradient, we can calculate the upper mantle density at any point along the mass column.

We use a combination of Pratt's and Airy's isostatic model to obtain the thickness of the continental crust, as this is a first-order calculation; second-order terms are fully accounted for by the methods detailed previously. Using the oceanic ridge as a reference, we need to solve the isostatic equation

$$\rho_c d + I_o = C \tag{22}$$

where I_o is the contribution of the mantle under the continent, and C is a constant

$$C = \rho_w d_1 + \rho_B d_2 + \rho_o d_3 \tag{23}$$

where ρ_c is continental density, 2800 kg/m³, d is continental thickness, d_1 is ridge-crest seawater thickness, 2500 m; d_2 is thickness of the basaltic layer, 5×10^3 m; and d_3 is the distance from the base of the basaltic layer to the reference surface, 195×10^3 m. The reference surface density under the continents is 3300 kg/m³ and under the oceanic lithosphere (or at the ridge) it is 3320 kg/m³. The reason for this difference is discussed in the next chapter which deals with the extraction of the other sources. Once we know the

continental thickness and the temperature along any given mass column we are able to estimate the dipole and the mass effects.

Before we proceed with the calculations of the above mentioned effects we also need to consider more complicated cases than just an oceanic column or a continental column. There are some spherical trapezoids or triangles that contain an ocean and a continent, a continent which is covered by ice (i.e. Antarctica or Greenland), a continent which is covered by a shallow sea (i.e. Hudson Bay or the Baltic Sea), or any combination of these. Appendix D describes the solution of Equation 22 for all the different cases. There are 10 different "mixtures" or cases which are considered by the algorithm. Each component in the "mixture" is assigned a normalized weight based on the percentage of its own area in the spherical trapezoid or triangle. Therefore, the total dipole or mass effect produced by any given spherical trapezoid is a weighted average of all the components.

The density change, $\Delta\rho$, between a given mass column in the continent and the reference column of the ridge is obtained by the subtraction of the densities assigned for the appropriate sections of the columns (see Figures 31-33). Again, we are interested in the change of the dipole density, Δm, relative to the oceanic ridge, that is expressed using the density change. The dipole density change of

Figure 31. As Fig. 29 but for continental lithosphere, where y is the topographic height, d is the continental thickness, ρ_c is the density of the continent, 2800 kg/m³, and ρ_1 is the reference surface density under the continent. Ridge's parameters are as in Figure 29.
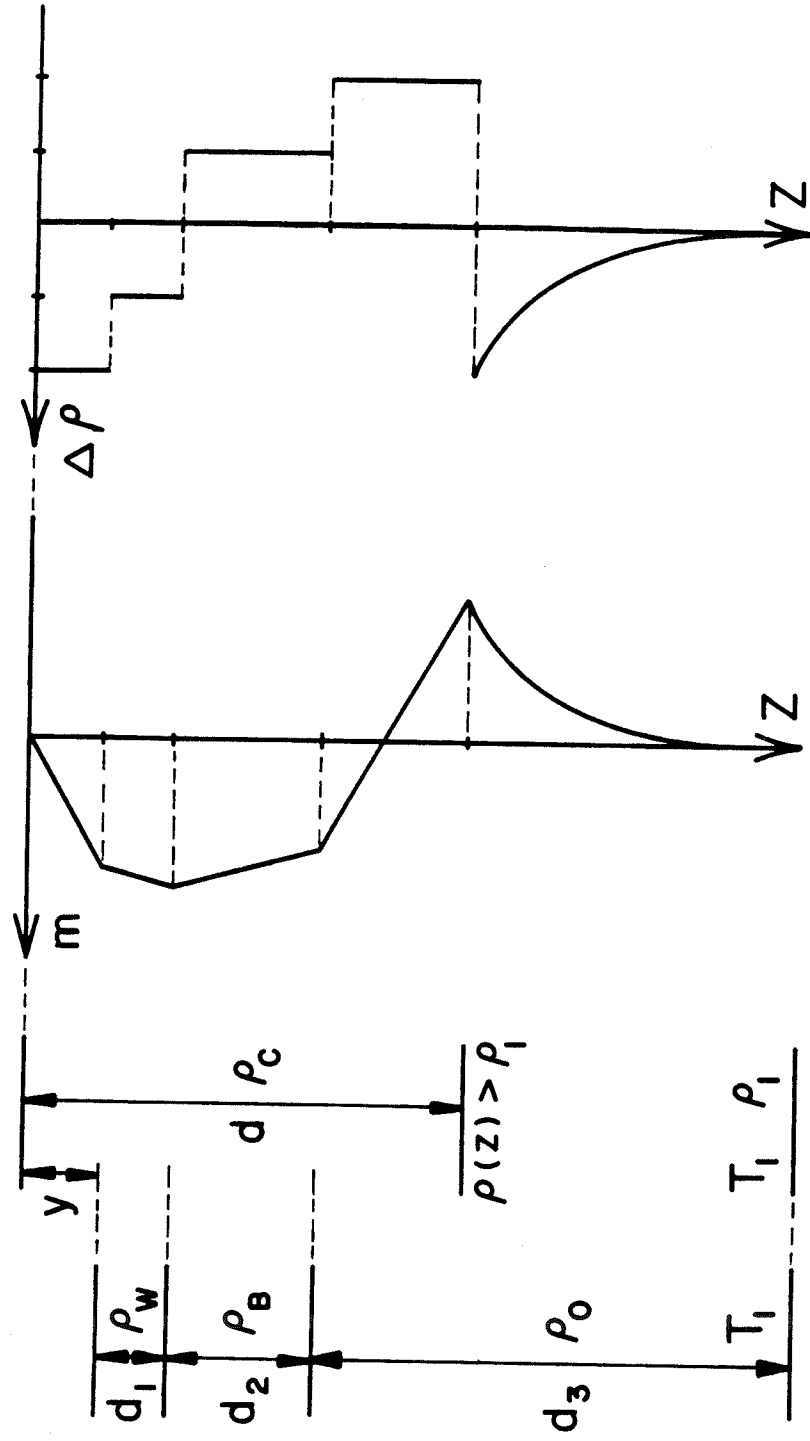
Figure 32. Ice over the continent, where f is the topographic height, y is the thickness of the ice layer and the other parameters as in Fig. 31.
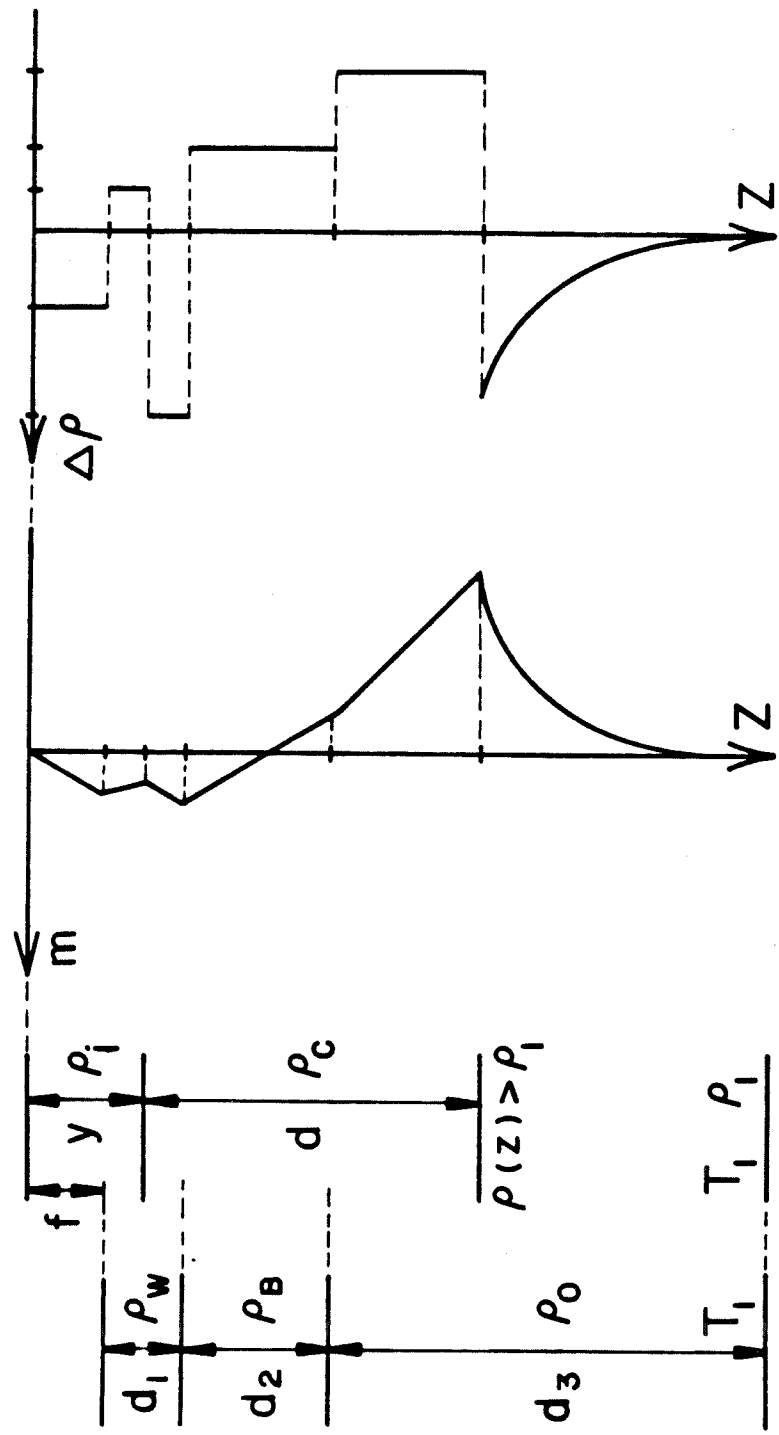
Figure 33. Shallow sea over the continent, where y is the depth of the shallow sea and the other parameters are as in Fig. 31.
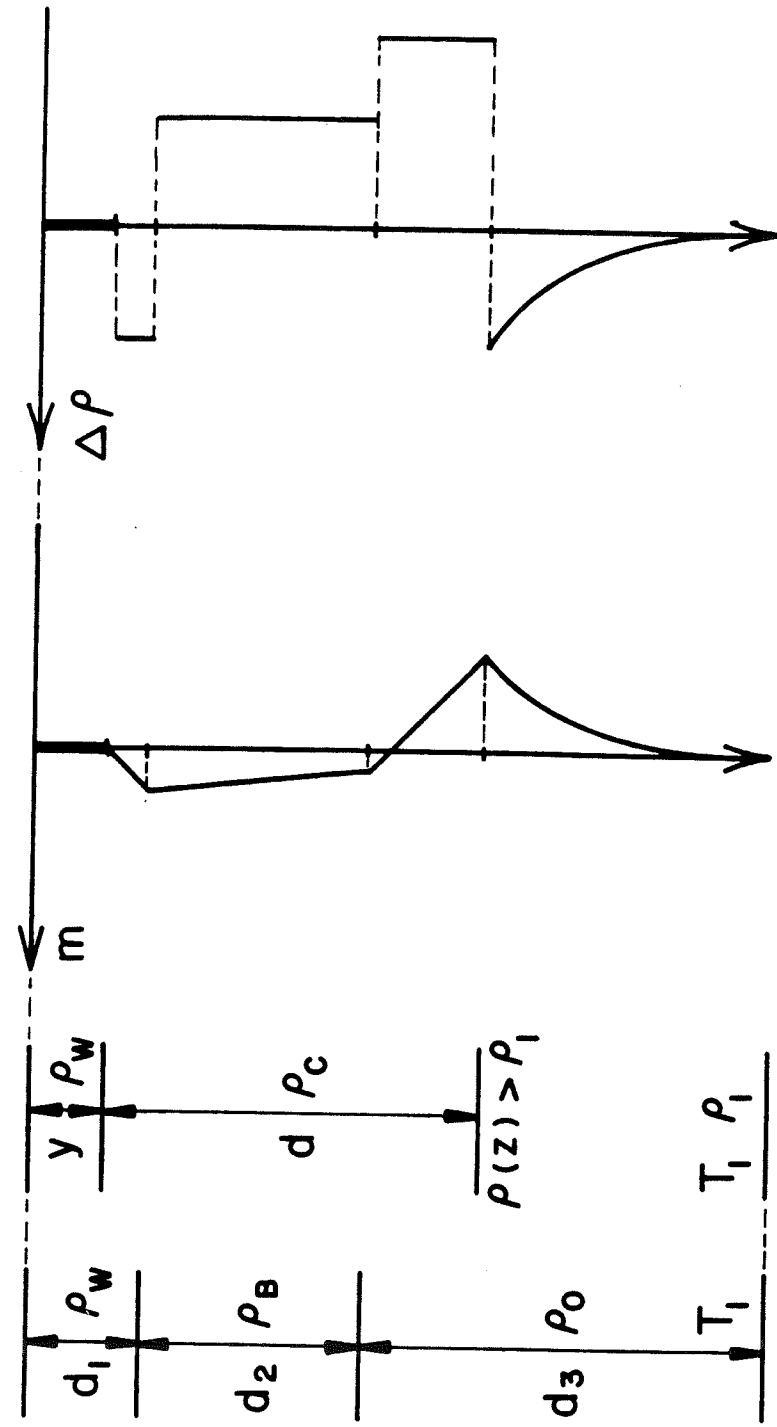
the first bin is

$$\Delta m = - \int_{-y}^{0} \rho_c dz + \int_{0}^{d_1} (\rho_w - \rho_c)dz + \int_{d_1}^{d_1+d_2} (\rho_B - \rho_c)dz + \int_{d_1+d_2}^{b} (\rho_0 - \rho_c)dz$$

$$= \rho_c(y - d) + \rho_w d_1 + \rho_B d_2 + \rho_0(b - d_1 - d_2)$$

where b=10 km, y is the topography, and the origin is at the oceanic ridge. In the case of a shallow sea over the continent, or a continent with ice cover, we need only to substitute the appropriate density for that part of the continent. The dipole density change is obtained similarly for the rest of the continental crust, using only the last term because the density difference is $\rho_0 - \rho_c$. The density change, $\Delta \rho$, at a given bin in the mantle under the continent is

$$\Delta \rho = \rho_1 \alpha \Delta T = \rho_1 \alpha [T_1 - T_m(z)]$$

where T_1 and ρ_1 are the reference surface temperature and density under the continental lithosphere, respectively. $T_m(z)$ is the temperature in the mantle under the continent, as expressed in Appendix D for the different cases. In general, $T_m(z)$ is a linear function of the depth, z

$$T_m(z) = e + lz$$

which implies that ρ is also a linear function of the depth

$$\Delta\rho = q + wz$$

where e, l, q, and w are constants. Thus, the dipole density change for the mantle below the crust, m, is

$$m = \int \Delta\rho \, dz = a + bz + vz^2$$

where a, b, and v are constants, and m has a parabolic shape. We can define $\bar{m}$, as in Equation 9, for a given bin in the mantle under the continent. As in the test planet case the dipole density change, Δm, and the density difference, $\Delta\rho$, are very small as z approaches the reference depth.

Once we have estimated the dipole density change, Δm, and the density difference, $\Delta\rho$, we can calculate the dipole and mass effects as we did for the test planet (Equations 11, 13, 15, and 17). The final geoid and reference surface are obtained by using Equations 20 and 21.

8.2 RESULTS OF THE REAL EARTH MODEL

The signals due to the mass effect over the geoid or over the reference surface are similar in shape and magnitude (see Figs. 34 and 35). The reason for is that the separation distance between the geoid and the reference surface of 200 km is small relative to masses which are several thousands of kilometers away. Continents are characterized by a positive geoid anomaly, while over ocean basins the geoid anomalies are mainly negative. This is caused by an excess mass in the elevated topography of the continent relative to ocean basin, which is a positive mass dipole. The final mass effect signal due to the self-deformation process has a larger absolute magnitude of each anomaly, but retains the main feature as before (see Figs. 36 and 37), with a geoid high of up to 25 m over north Asia and Europe and a geoid low of up to -25 m west of South America. The mid-Atlantic ridge is vaguely visible in the source or the final geoid, and east Pacific rise not visible at all.

The geoid topography due to the dipole effect appears to be a reflection of the reference surface, except to higher amplitudes at the latter (see Figs. 38 and 39). Each continent can be represented as a positive mass dipole, therefore the geoid over most of the continents is positive; on the other hand, over ocean basins we

Figure 34. Initial geoid (meters) over the earth assuming the mass

effect only, where the reference surface densities under

the continental lithosphere and the oceanic lithosphere are

3300 kg/m³ and 3320 kg/m³, respectively.
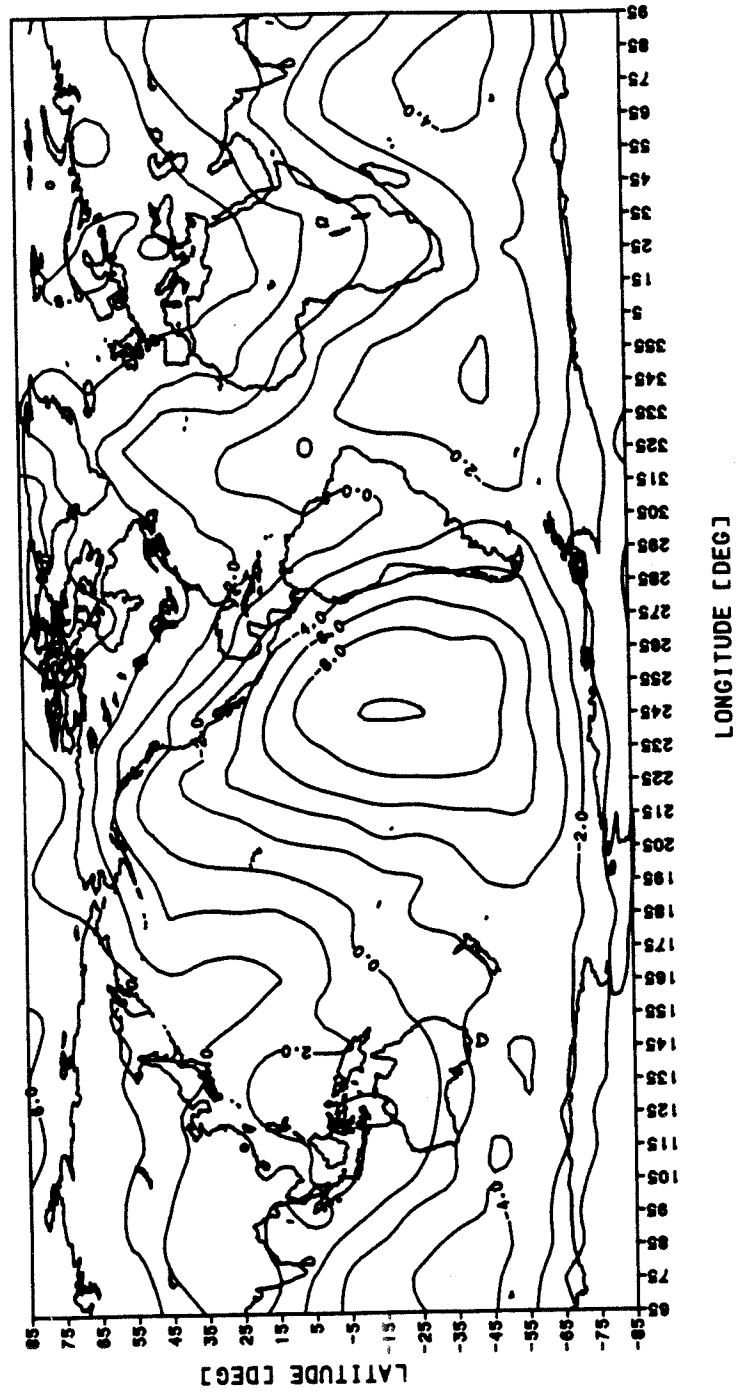
Figure 35. As Fig. 34 but for the reference surface.

Figure 36. Final geoid (meters) over the earth assuming the mass effect only.
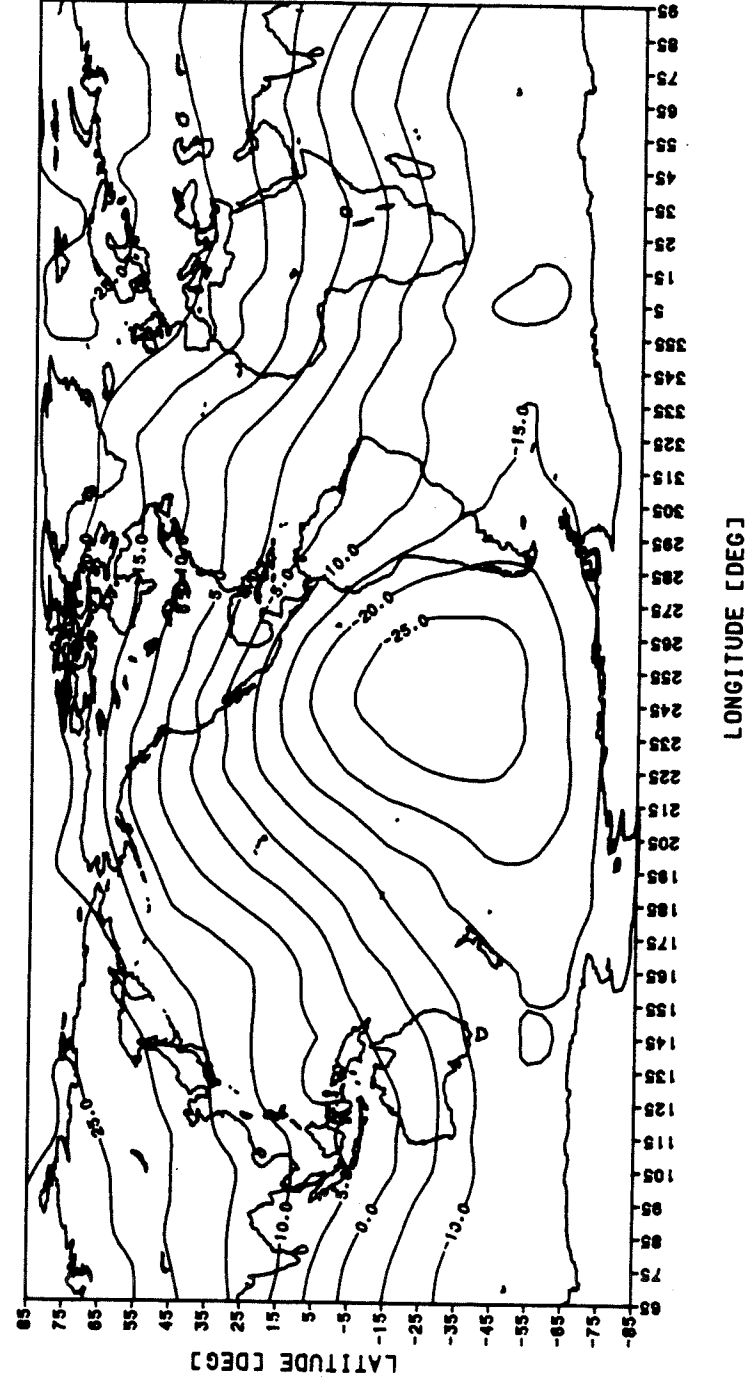
Figure 37. As Fig. 36 but for the reference surface.
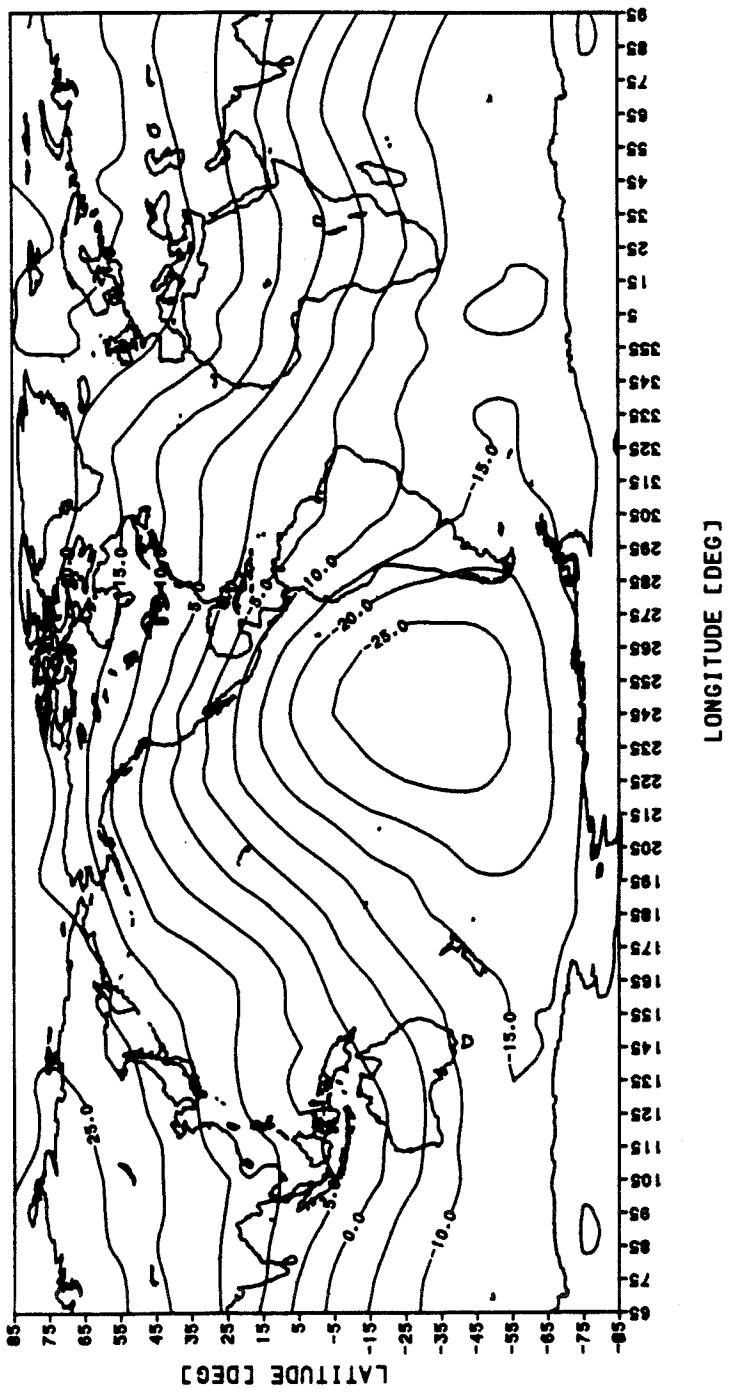
Figure 38. Initial geoid (meters) over the earth assuming the dipole effect only, where the reference surface densities under the continental lithosphere and the oceanic lithosphere are 3300 kg/m³ and 3320 kg/m³, respectively.

Figure 39. As Fig. 38 but for the reference surface.

103

Figure 40. Final geoid (meters) over the earth assuming the dipole effect only.
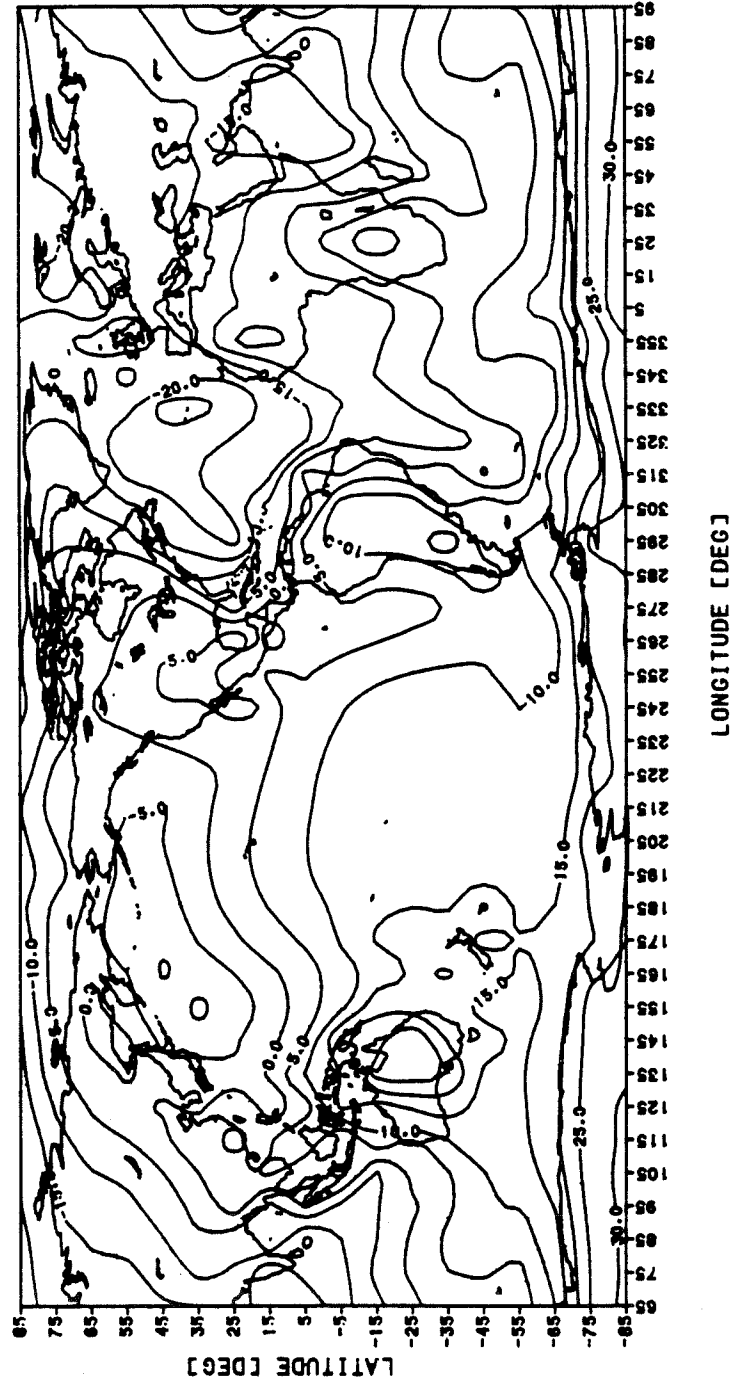
Figure 41. As Fig. 40 but for the reference surface.
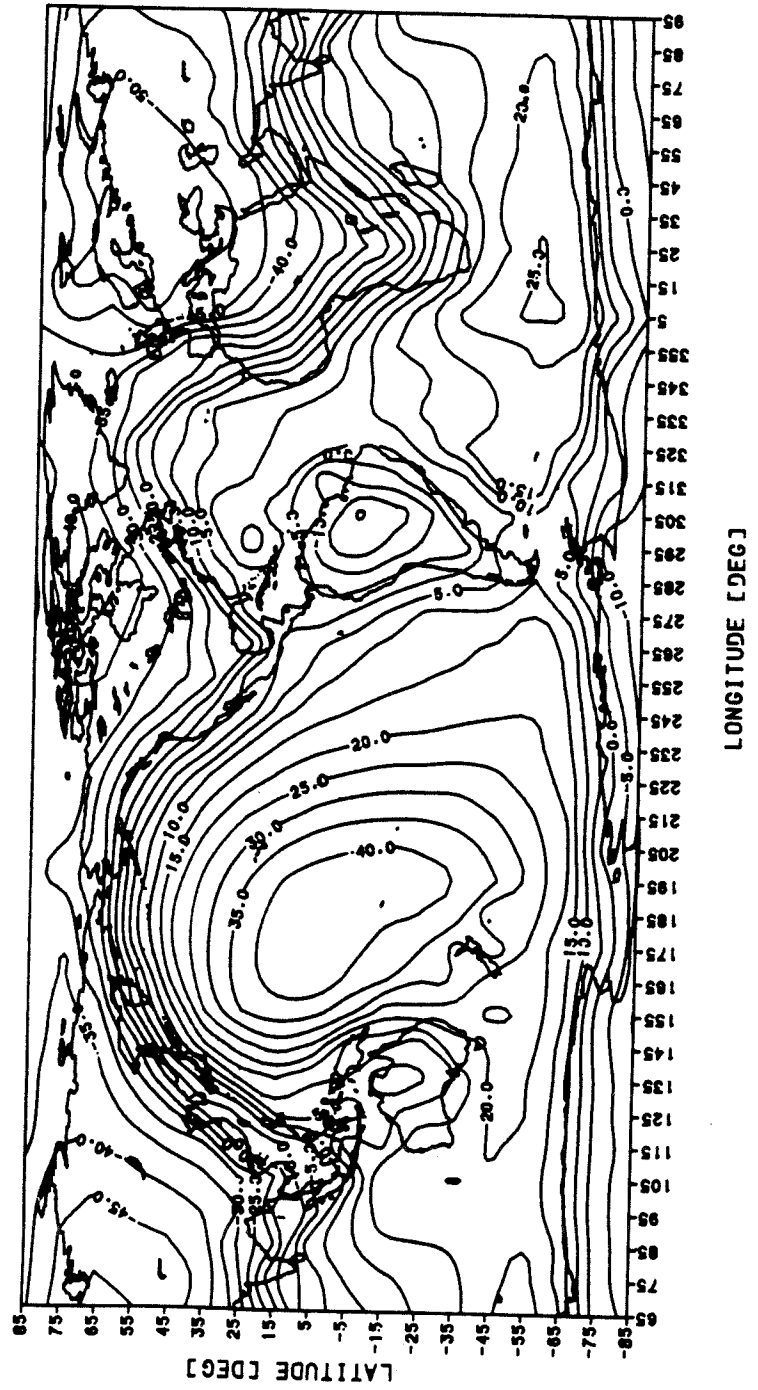
observe a geoid low, because of conservation of mass.

The final signals of the geoid and the reference surface due to the self-deformation effect are illustrated in Figs. 40 and 41; over the reference surface we observe larger absolute amplitudes for each anomaly. Over the geoid the situation is more complicated, for two reasons. The first is that the anomalies of the initial reference surface have usually larger absolute amplitudes than those of the initial geoid. The second reason has to do with the fact that the reference surface density is about 3.3 times larger than the seawater density. This fact increases dramatically the influence of the self-deformation effect. The reference surface's anomalies are large enough to cause a significant change in the geoid. The region over the west Pacific is characterized by a small geoid low due to the high anomaly below at the reference surface. Surprisingly enough, the final geoid over Africa and most of Euroasia and North America turns out to be either negative or barely positive, unlike the initial geoid. As in the mass effect case, the mid-Atlantic ridge can be faintly observed in the source and the final geoid, and the East Pacific rise is invisible.

The source influence of the combined dipole and mass effects over the geoid and the reference surface is illustrated in Figs. 42 and 43. The dipole effect is in general larger than the mass effect; therefore, the shape and the magnitude of the anomalies follow closely those of the dipole effect in most of the regions. The final reference surface (see Fig. 45) due to the self-deformation process retains the

106

Figure 42. Initial geoid (meters) over the earth assuming the combined dipole and mass effects, where the reference surface densities under the continental lithosphere and the oceanic lithosphere are 3300 kg/m³ and 3320 kg/m³, respectively.

107
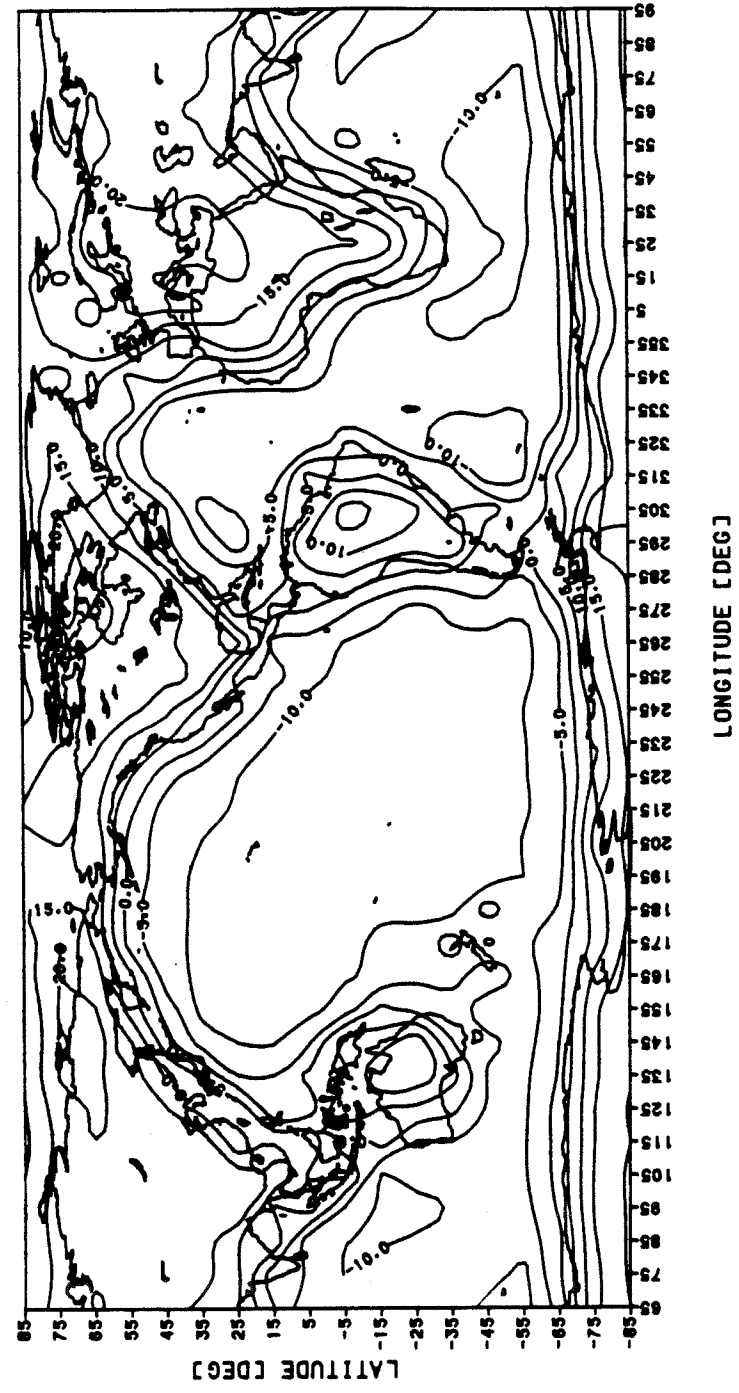
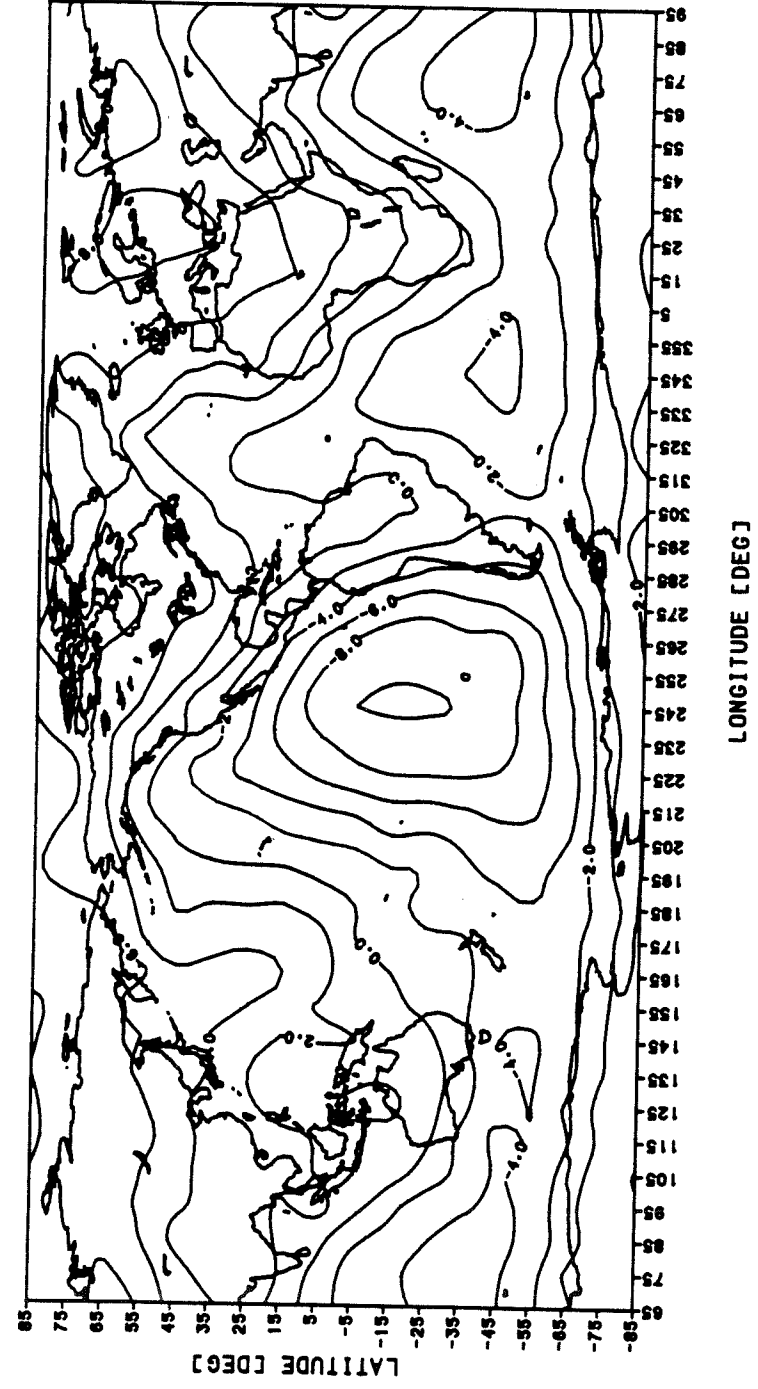Figure 43. As Fig. 42 but for the reference surface.

108
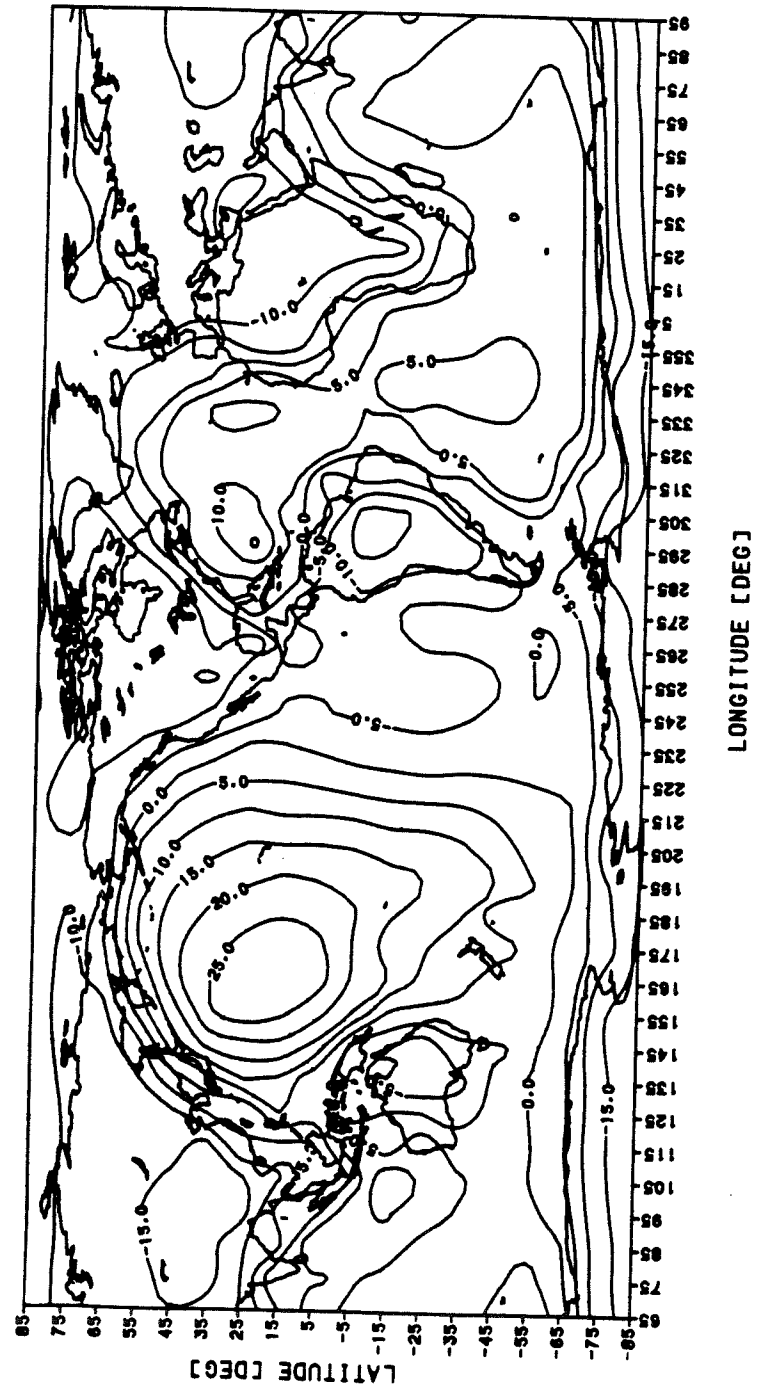
Figure 44. Final geoid (meters) over the earth produced by mass separations in the lithosphere.

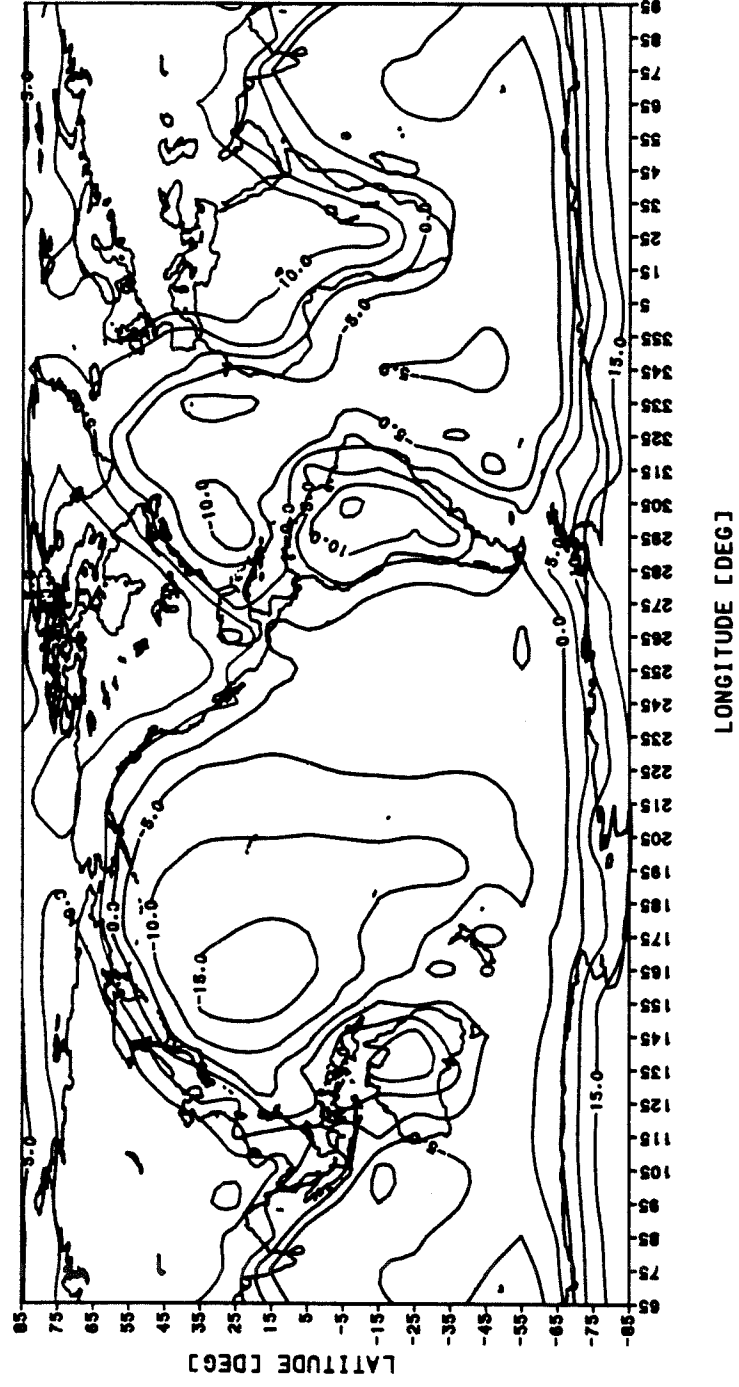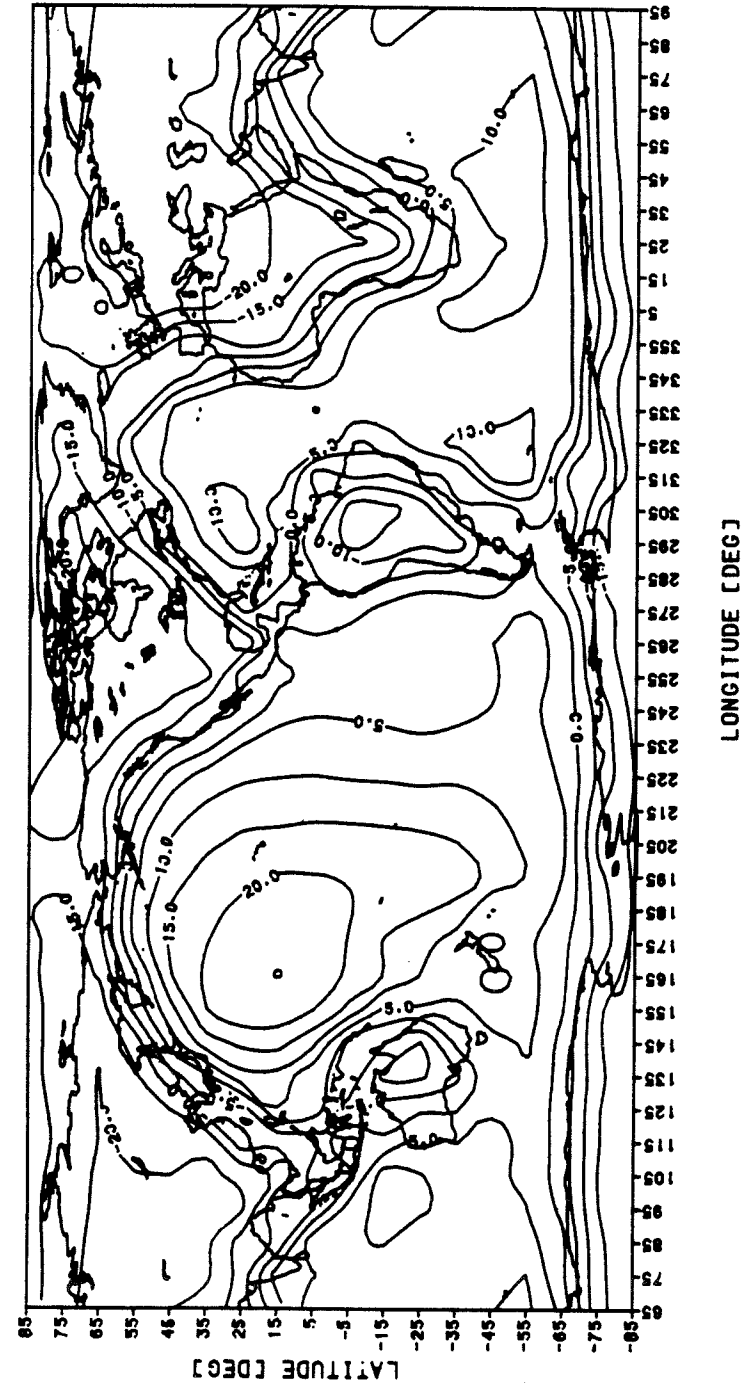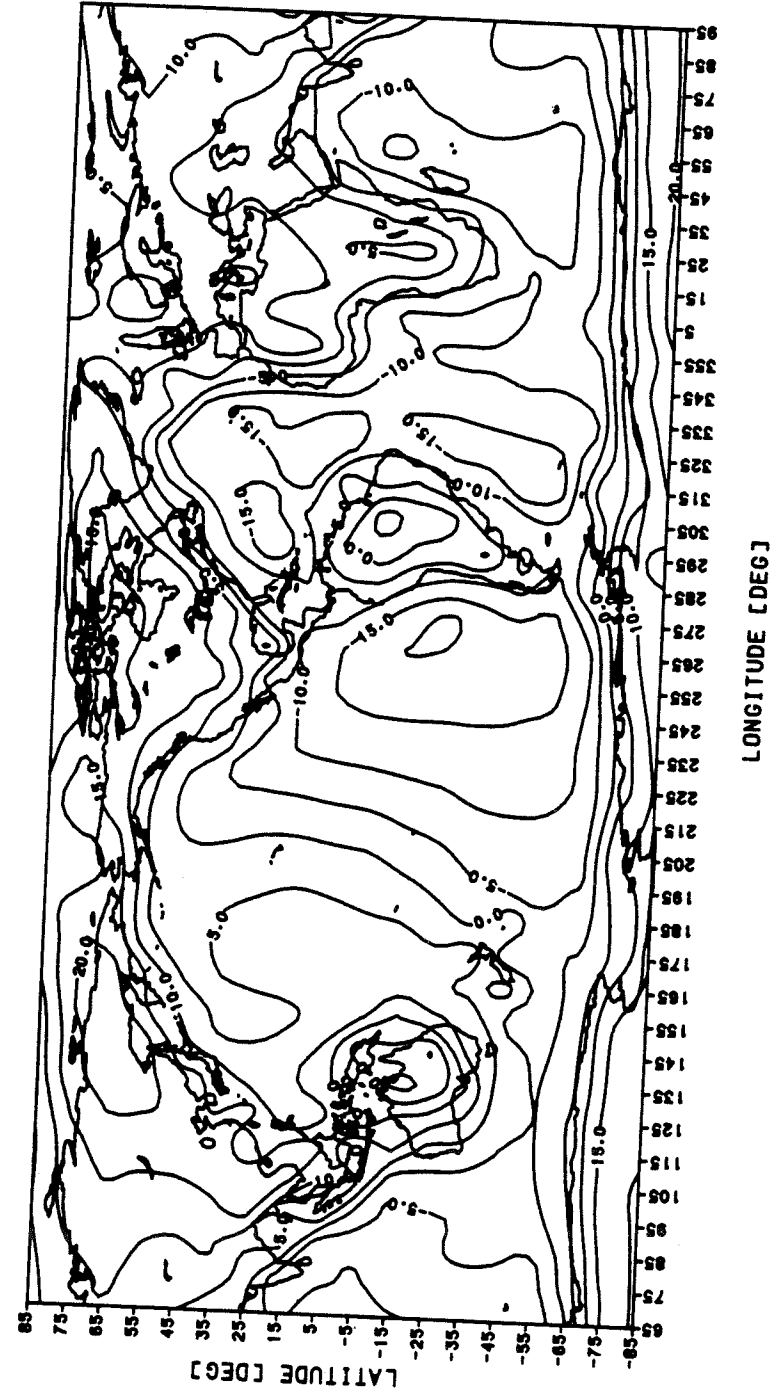Figure 45. As Fig. 44 but for the reference surface.
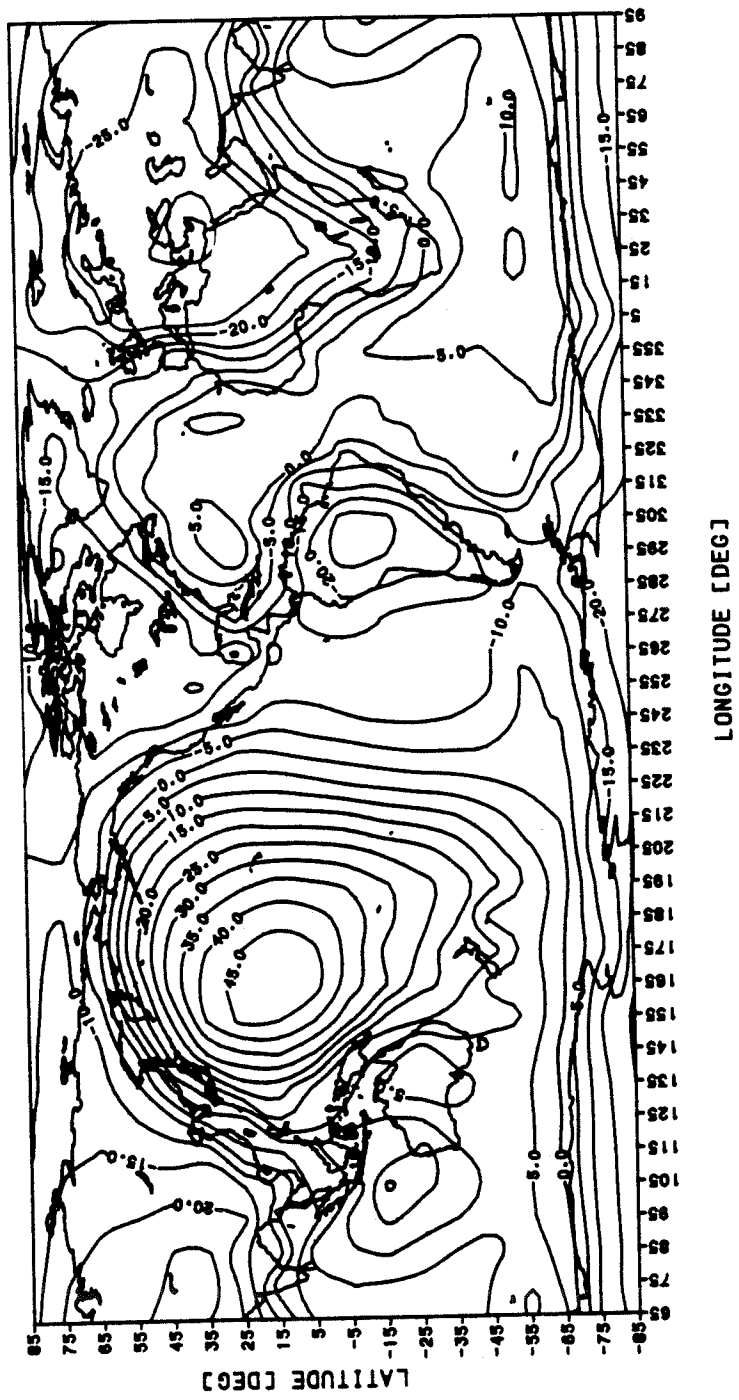
same shape but has larger amplitudes. Again, the surface under the continents is mainly characterized by geoid lows and the regions under the ocean basins usually have a positive geoid anomaly, with a significant high anomaly in the west Pacific region of up to 45 m. The anomalies over the geoid (see Fig. 44) are largely dominated by those of the reference surface, for the same reasons mentioned before. Continents are mainly characterized by a geoid high, while over ocean basins we observe a wide geoid low.

The source influence of the dipole effect, the mass effect, or the combined effect is not simply the sum of the dipole moment or mass anomaly, integrated vertically. The reason is that the values observed at each spherical trapezoid are due to all the rings that cover the whole earth, as was previously discussed. In the case of the dipole effect the geoid anomaly is a function of the dipole density, distance, and the "geometrical factor" (below or above the dipole equatorial plane). Let us focus our attention on the distribution of the dipole over the earth, which means that the observation point is located in the middle of a given spherical trapezoid and we take into account only the effects of the bins below in that column (see Figure 46). It can be shown (Appendix E) that the geoid anomaly due to the dipole effect is

Figure 46. Geometry of the dipole distribution case, where O is the observation point, N is the measuring point, z is the depth of the dipole layer, and C is the center of earth.
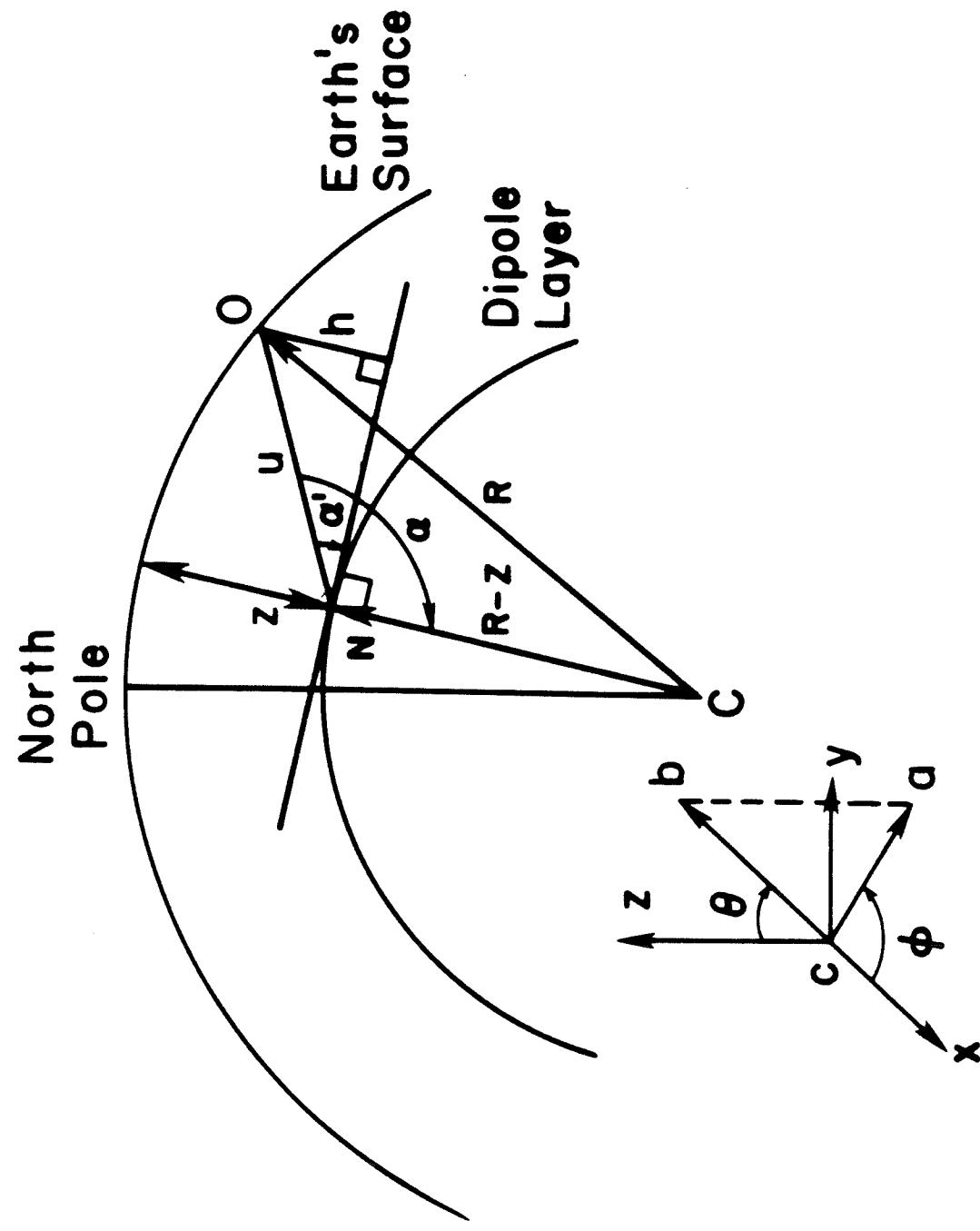
$$\gamma = \frac{G}{g} \int\limits_{z'}^{z''} \int\limits_{\phi'}^{\phi''} \int\limits_{\Theta'}^{\Theta''} \frac{m(R - z)^2 \sin \alpha' \sin \Theta \, d\Theta \, d\phi \, dz}{u^2} \qquad (24)$$

where u is the distance between the observation point, O, and the measuring point, N; α' is the smallest angle between $\underline{u}$ (a vector) and the dipole equatorial plane; z' and z", ϕ' and ϕ'', and Θ' and Θ'' are the boundaries of the depth, z, the longitude, ϕ, and the latitude, Θ, for a given bin, respectively.

The HOT equation of Haxby and Turcotte (1978) is

$$\gamma_{HOT} = \frac{-2\pi G}{g} \int\limits_{0}^{d} z \, \rho(x,z) \, dz$$

where d=d(x) is the depth, $\rho(x,z)$ is the density change and x is the horizontal axis. The HOT equation is simpler because it does not take into consideration the fact that columns are pie-shaped on a spherical earth. Equation 24 is actually a modified version of the HOT equation, suited for the spherical earth case. Figure 47 illustrates the results of the HOT equation. As the continents are positive mass dipole they are dominated by a geoid high with a sharp jump along the coastlines, while the ocean basins are mostly characterized by a wide geoid low.

The oceanic ridge serves as a reference point which means that the geoid should be almost zero there. Both the east Pacific rise and the mid-Atlantic ridge can be observed by a geoid ridge at about -1 m and

-4 m. The reason for drop below zero is that regardless of the fact that the observation point is exactly located over the ridge or not, there is some influence of the ridge sides within the bin, especially for younger ages as the slopes there fall off faster than those of older ages. We would need a much finer model to minimize the effect of the ridge sides. The final geoid due to the combined effect is obviously different in its shape and magnitude from that of the HOT formula. This means that the contribution of the self-deformation effect is significant to the calculated geoid.

114

Figure 47. The geoid anomaly due to the distribution of the dipole
over the earth in meters.
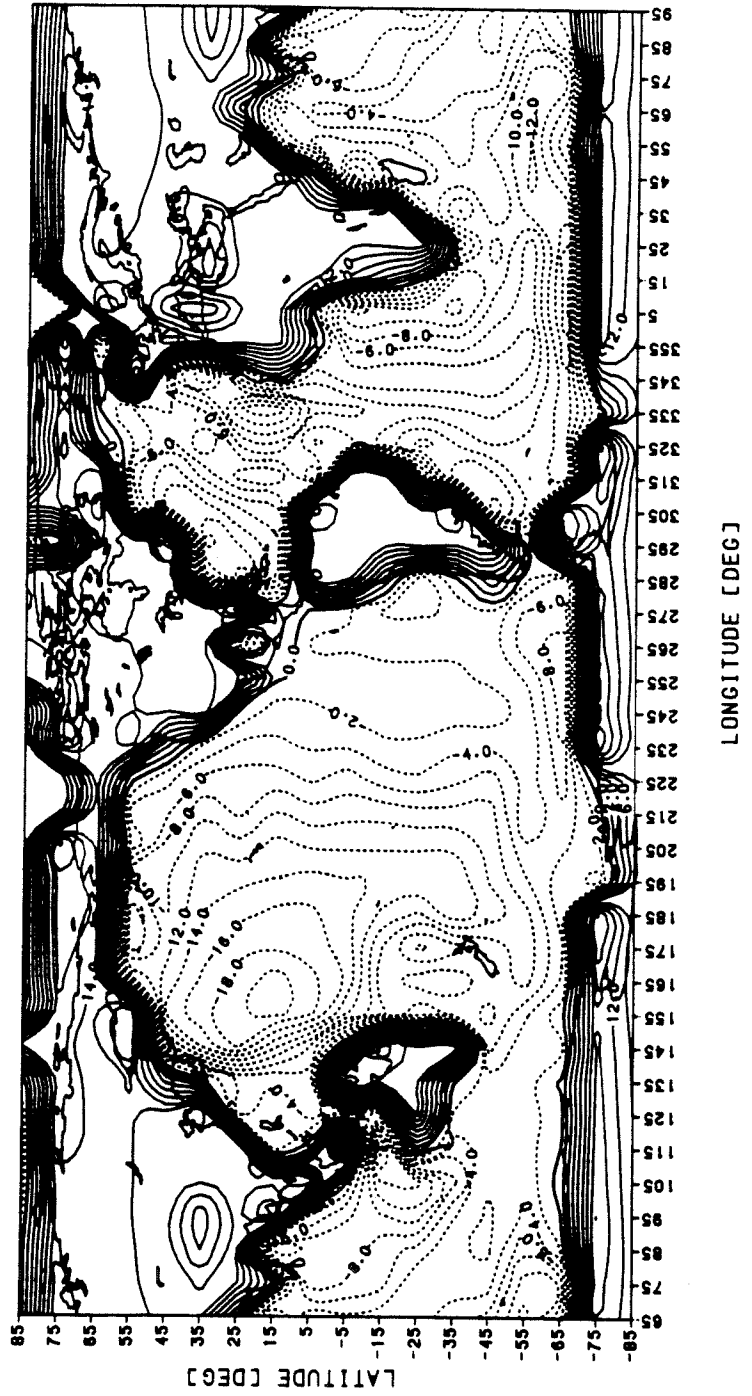
CHAPTER NINE - DISCUSSION

The global geoid over the earth (see Fig. 48), as derived from Geos-3 (Rapp, 1979a, b), is composed of two main components. The first source, known as the calculated geoid (see Fig. 45), is due to density changes in the continental and the cooling oceanic lithospheres; it is considered a shallow source. The second component, also called the residual geoid, is due to large mass anomalies in the deep mantle, and is obtained by subtraction of the calculated geoid from the global geoid (see Fig. 49).

The calculated geoid is dependent on the reference surface density, and this dependence, in turn, causes the residual geoid to be dependent on that reference surface density. This dependence was carefully checked by assigning two different values for the reference surface densities under the ocean and under the continents, and varying the densities in small steps. For each set of reference surface densities we get a value of the calculated geoid for each of the 36x18 spherical trapezoids. The calculated geoid variance is then computed and compared with those of the global geoid and the residual geoid. The residual geoid variance is minimized for reference surface densities of 3380 kg/m^3 and 3360 kg/m^3 under the oceanic and under the continental lithospheres, respectively (see Figure 50). There is an obvious trend of the results which indicates that a density difference

Figure 48. The observed geoid (meters) over the earth as derived from GEOS-3 altimetry data.
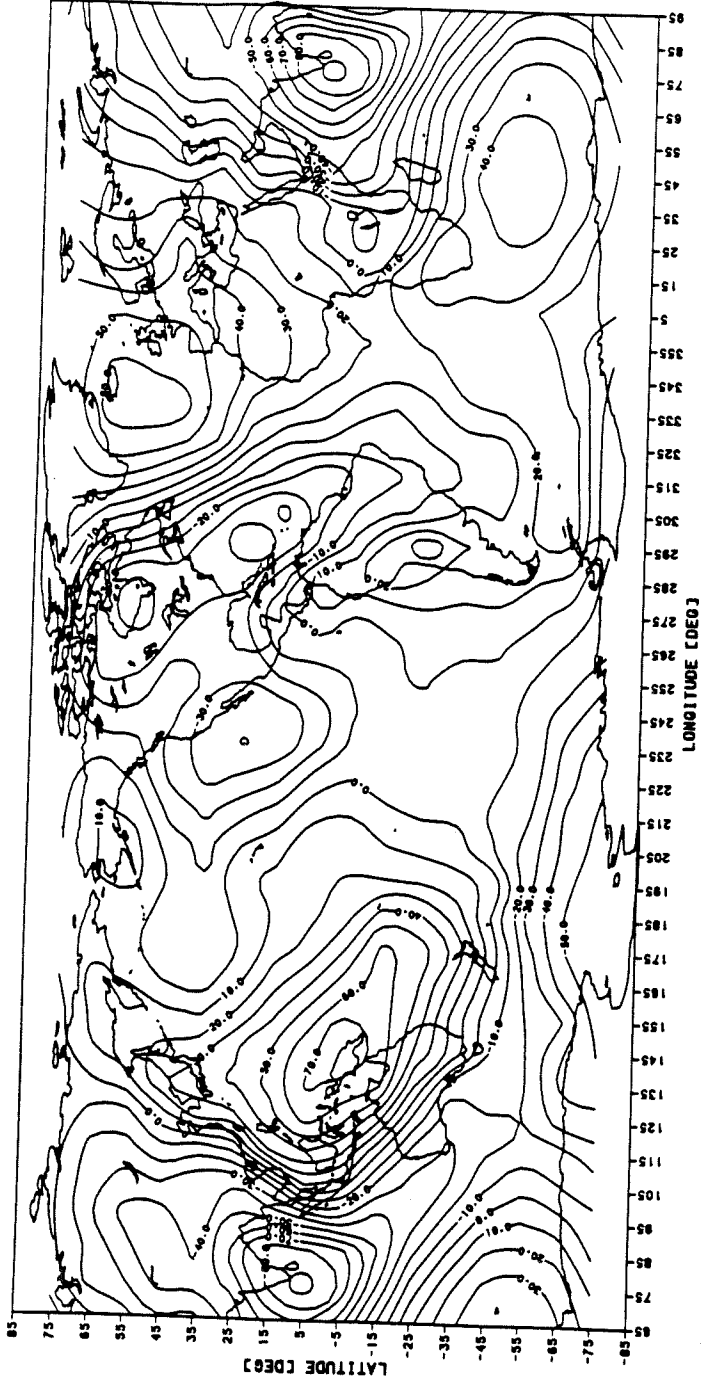
Figure 49. Residual geoid (meters) over the earth.
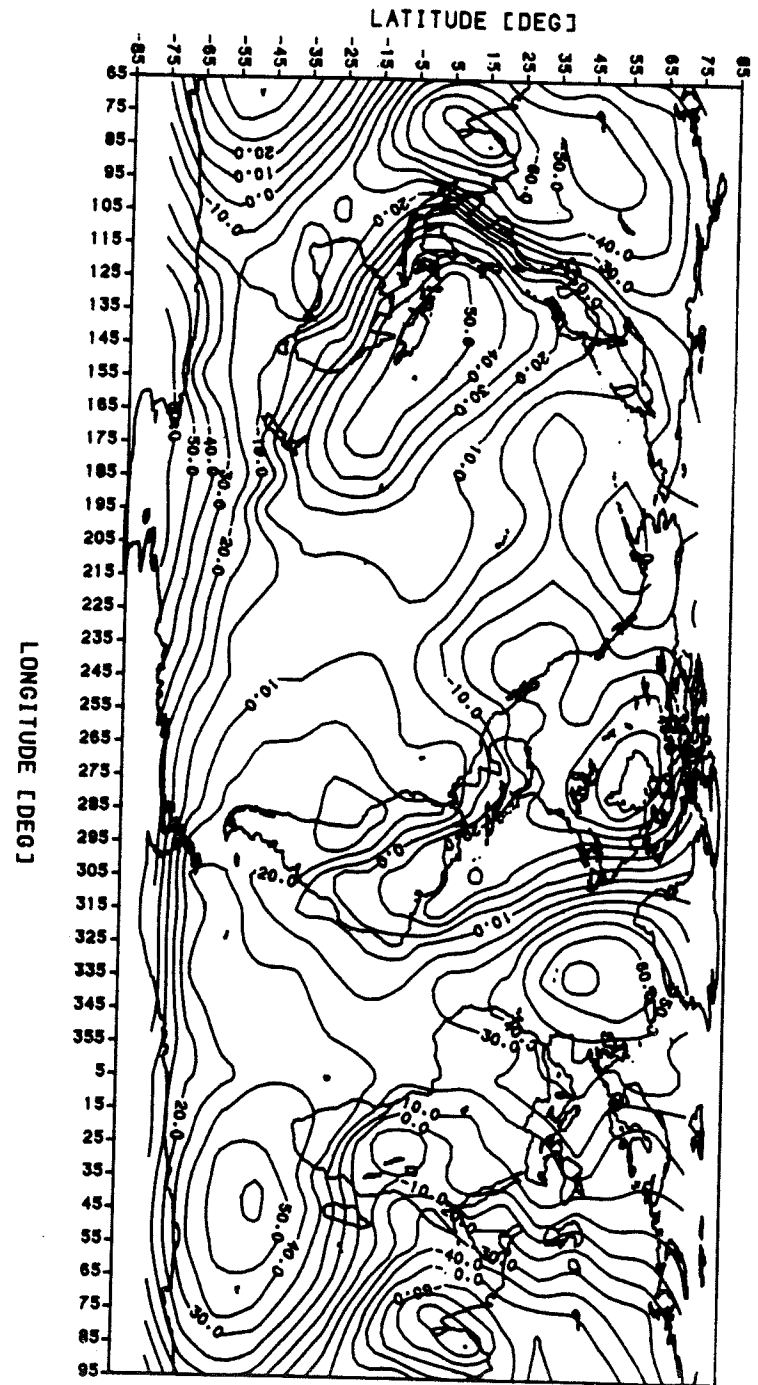
Figure 50. Contours of the residual geoid variance in m² as a function
of the reference surface density under the oceanic and
continental lithosphere in gr/cm³.
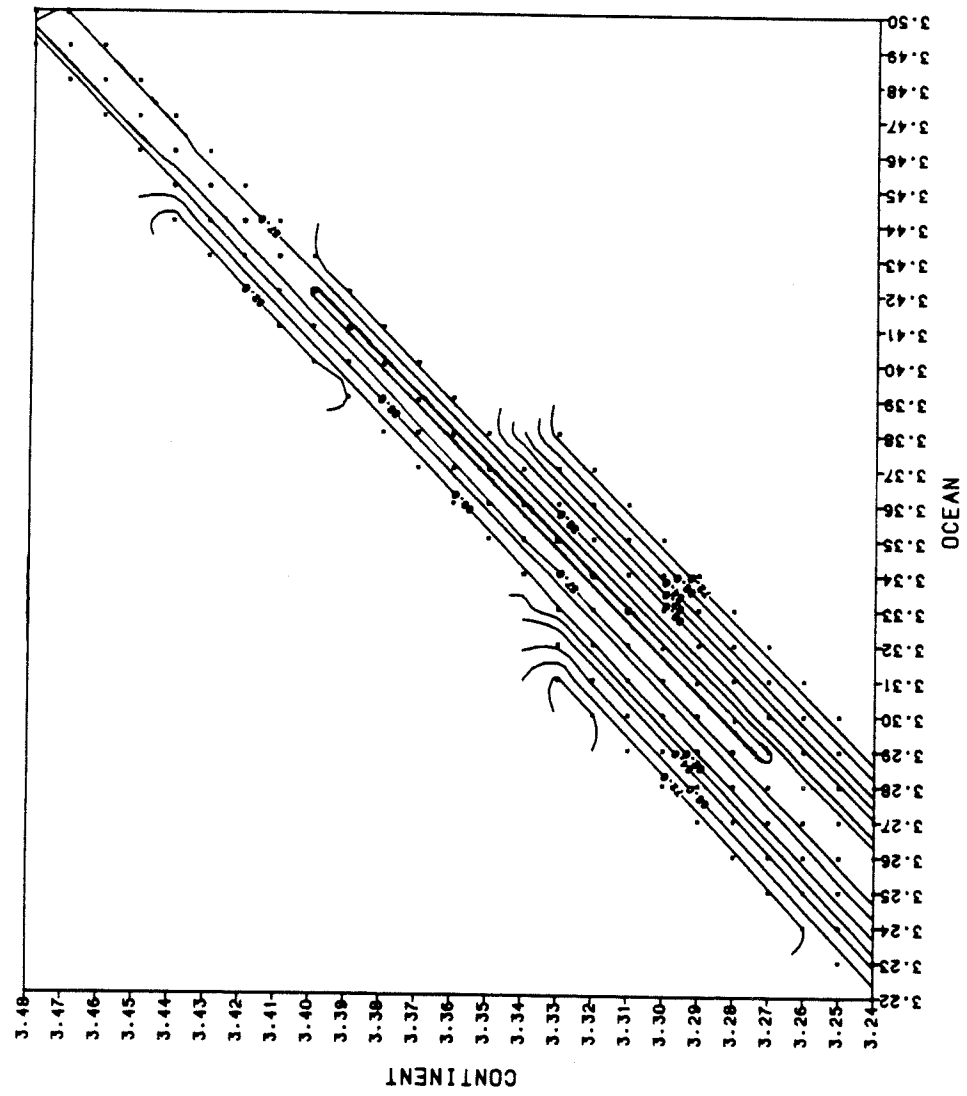
of about 20 kg/m³ minimizes the residual geoid variance. The detected minimum of the residual geoid variance is not a distinct one, which means that the results are not constrained along the axis of the "valley", unlike the the sides of the valley. This interesting result suggests that the density difference is probably real, although it is statistically insignificant; the reason is that the variance of the observed geoid is much larger than the variance of the calculated geoid. Therefore, the variance of the residual geoid is slightly reduced, but not enough to be statistically significant. Despite this discouraging result of only slightly reduced residual geoid variance, we would like to mention here an interesting observation.

Recently, diamonds and diamond-bearing rocks found in South Africa kimberlite pipes were studied. Kimberlite pipes are pipes that penetrate deep into the mantle and deliver debris and volcanic material from down below. The formation of the diamonds occurs at depths between 150 to 200 km. The formation temperature has a wide range of 900 °c to 1400 °c (Boyd and Finnerty, 1980), and the age is about 3.2 to 3.3 billion years ago (Richardson et al., 1984). This temperature at the base of the craton is surprisingly low compared to calculated values, although the Archean heat flow is considered to be twice today's heat flow value (Jordan, 1979; Boyd and Gurney, 1986). This means that somehow a cold root has been formed beneath the craton. If the root is denser than the ambient material it should sink down, while if it is made of lighter material than the surroundings, then it floats and the effect of the temperature is to make it even lighter (Jordan, 1979). Richardson et al. (1984) and Boyd and Gurney

(1986) pointed out that rocks at the base of the craton are slightly lighter than those of the oceanic lithosphere, as they contain more magnesium than iron. A possible explanation is that during the Archean age, large volumes of basaltic magma were extracted from the mantle to form the new crust, leaving a magnesium-rich mantle. Our results show a very good agreement with these observations.

There are regions where the calculated geoid (see Fig. 45) follows closely the global geoid (see Fig. 48), such as south of India, the western Pacific ocean, and east of Puerto Rico. On the other hand, there are also regions where there is a negative correlation between the observed and calculated geoids, such as over the Andes, Iceland, west of Mexico, southeast of Africa, and the Hudson Bay region. These structures are presumably caused by flow in the mantle or by some mass anomalies in the deep mantle, and have nothing to do with the lithospheric geoid. Usually they have more power than the calculated geoid; correlation between the the observed and calculated geoid is poor.

The goals of this study were twofold: to show the importance of the self-deformation effect, and to compute the lithospheric geoid over the earth, using the static model. The next step, which is beyond the scope of this study, is to solve the dynamic model, which is more complicated as it involves mantle flow. However, one may obtain some insight, even before solving the dynamic problem just by carefully examining the residual geoid (see Fig. 49). In the next section we briefly discuss the residual geoid close to oceanic trenches and

ridges, as the mantle flow close to them might produce a significant geoidal contribution.

Mass accumulation is sometimes associated with an oceanic trench, such as the regions of the Bonin and Mariana trenches, where there is a good correlation with the residual geoid high. However, it is absent close to the Kuril, Aleutians, Costa Rica, and Puerto Rico trenches, where the residual geoid is relatively small. Although there is no mass accumulation close to the west coast of South America, we observe a residual geoid high mainly over the Andes and over some of the Chile trench. The residual geoid high can be attributed to both the Andes (mass excess) above and the subducting slab below that is colder and denser than the ambient material. The causes of the phenomenal vast mass accumulation in the west Pacific are not clear. It can be argued that, unlike in other regions, there is probably more resistance of the mantle to the sinking slab in this region, which significantly slows down the subduction process, or yields little return flow (Hager and O'Connell, 1979). In addition, it seems that mass accumulation is not a fundamental result of subducting plates, and the regions close to trenches, such as the areas near the Kuril and Aleutians trenches, are not characterized by an elevated seafloor topography. If this is the case, then the subducting plate does not contribute a significant portion to the global geoid, although it is colder and denser than the ambient mantle.

The effect of the oceanic ridges was accounted for in the previous chapter. Over the Icelandic region there is a residual geoid high which decreases to about 20 m to 30 m in the south Atlantic ocean.

Over the east Pacific rise we observe both negative and positive residual geoid. All these anomalies seem to be influenced by the "near-by" anomalies, such as over the Andes, Iceland swell, and south east of Africa. The width of these anomalies suggests that they are probably located in the deep mantle, and have nothing to do with ridge processes. Over the Indian Ocean we observe mostly negative residual geoid, i.e. over Carlsberg ridge, mid-Indian ridge, and Ninety East rise, which are heavily influenced by the global low in south of India. This huge geoid low cannot be related to any special topography structure, and it can be only explained by a huge mass deficiency created as the sub-continent slid north towards Asia (LePichon, 1968).

The qualitative arguments which were brought here lead to an important conclusion: the contribution of "plate tectonic" related processes is of a minor nature, and major mass anomalies in the deep mantle or even in the core-mantle boundary are what actually shape the global geoid. If this is indeed so, an attempt should be made in the future to account for these sources. While a small number of questions have been studied and solved (mostly the basic features of lithospheric geoid), there are still many important open questions, i.e., the deep mantle sources and their causes. Further studies of deep mantle geoid are therefore warranted, as they would give a better understanding of the mantle processes.

LIST OF REFERENCES

Anderson, D. L., Chemical stratification of the mantle, J. Geophys. Res., 84, 6297-6298, 1979.

Airy, G. B., On the computation of the effect of the attraction of the mountain masses as disturbing the apparent astronomical latitude of stations in geodetic surveys, Phil. Trans. Roy. Soc. Lond., 145, 101-104, 1855.

Bauer, F. L., H. Rutishauer, and E. Stiefel, New aspects in numerical quadrature, Proc. of Symposia in Appl. Math., XV, 199-218, Am. Math. Soc., Providence, R.I., 1963.

Benioff, H., Orogenesis and deep crustal structure: additional evidence from seismology, Bull. Geol. Soc. Amer., 65, 385-400, 1954.

Boyd, F. R., and J. J. Gurney, Diamonds and the African lithosphere, Science, 232, 472-477, 1986.

Boyd, F. R., and A. A. Finnerty, Conditions of origin of natural diamonds of peridotite affinity, J. Geophys. Res., 85, 6911-6918, 1980.

Bullard, E. C., Continental drift, Quat. J. Geol. Soc. Lond., 120, 1-34, 1964.

Bullard, E. C., J. E. Everett, and A. G. Smith, The fit of the continents around the Atlantic, Phil. Trans. Roy. Soc., A, 258, 41, 1965.

Busse, F. H., On the ratios of two-layer mantle convection, Phys. Earth Plan. Int., 24, 320-324, 1981.

Busse, F. H., Quadrupole convection in the lower mantle?, Geophys. Res. Lett., 10, 285-288, 1983.

Carslaw, H. S., and J. C. Jaeger, Conduction of heat in solids, 2nd edition, Oxford University Press, 1959.

Cathles, L. M., III, The viscosity of the earth's mantle, Ph.D. Thesis, Princeton University, N. J., 1971.

Chapman, M. E., and Bodine, J. H., Considerations of the indirect effect in marine gravity modelling, J. Geophys. Res., 84, 3889-3892, 1979.

Chase, C. G., Subduction, the geoid, and lower mantle convection, Nature, 282, 464-468, 1979.

Chase, C. G., and M. K. McNutt, The geoid: effect of compensated topography and uncompensated oceanic trenches, Geophys. Res. Lett., 9, 29-32, 1982.

Clark, S. P., and A. E. Ringwood, Density distribution and constitution of the mantle, Rev. Geophys. Space Phys., 2, 35-88, 1964.

Crough, S. T., Thermal origin of mid-plate hot-spot swells, Geophys. J. Roy. Astron. Soc., 55, 451-469, 1978.

Crough, S. T., and D. M. Jurdy, Subducted lithosphere, hotspots, and the geoid, Earth Planet. Sci. Lett., 48, 15-22, 1980.

Cox, A., Geomagnetic reversals, Science, 163, 237-245, 1969.

Creager, K. C., and T. H. Jordan, Slab penetration into the lower mantle, J. Geophys. Res., 89, 3031-3049, 1984.

Dahlen, F. A., Isostasy and the ambient state of stress in the oceanic lithosphere, J. Geophys. Res., 86, 7801-7807, 1981.

Dahlen, F.A., Isostatic geoid anomalies on a sphere, J. Geophys. Res., 87, 3943-3947, 1982.

Davies, G. F., Whole mantle convection and plate tectonics, Geophys. J. Roy. Astr. Soc., 49, 459-486, 1977.

Davies, G. F., Geophysical and isotopic constraints on mantle convection: An interim synthesis, J. Geophys. Res., 89, 6017-6040, 1984.

Davis, E. E., and C. R. B. Lister, Fundamentals of ridge crest topography, Earth & Plan. Sci. Lett., 21, 405-413, 1974.

Dewey, J. F., and J. M. Bird, Mountain belts and the new global tectonics, J. Geophys. Res., 75, 2625-2647, 1970.

Dietz, R. S., Continent and ocean basin evolution by spreading of the sea floor, Nature, 190, 854-857, 1961.

Dutton, C. E., On some of the greater problems of physical geology, Bull. Phil. Soc. Wash., 11, 51-64, 1889.

Dziewonski, A. M., Mapping the lower mantle: Determination of lateral heterogeneity in P velocity up to degree and order 6, J. Geophys. Res., 89, 5929-5952, 1984.

Dziewonsi, A. M., B. H. Hager, and R. J. O'Connell, Large scale heterogeneities in the lower mantle, J. Geophys. Res., 82, 239-255, 1977.

Forsyth, D. W., The evolution of the upper mantle beneath mid-ocean ridges, Tectonophysics, 38, 89-118, 1977.

Elsasser, W. M., P. Olson, and B. D. Marsh, The depth of mantle convection, J. Geophys. Res., 84, 147-155, 1979.

Hager, B. H., Global isostatic geoid anomalies for plate and boundary layer models of the lithosphere, Earth Planet. Sci. Let, 63, 97-109., 1983.

Hager, B. H., Subducted slabs and the geoid: Constraints on mantle rheology and flow, J. Geophys. Res., 89, 6003-6015, 1984.

Hager, B. H., and R. J. O'Connell, Kinematic models of large-scale flow in the earth's mantle, J. Geophys. Res., 84, 1031-1048, 1979.

Hager, B. H., R. W. Clayton, M. A. Richards, R. P. Comer, and A. M. Dziewonski, Lower mantle heterogeneity, dynamic topography and the geoid, Nature, 313, 541-545, 1985.

Haskell, N. A., The motion of a viscous fluid under a surface load, Physics, 6, 265-269, 1935.

Haxby, W. F., On the amplification of long wavelength gravity anomalies, unpublished, 1983.

Haxby, W. F., and D. L. Turcotte, On isostatic geoid anomalies, J. Geophys. Res., 83, 5473-5478, 1978.

Hayford, J. F., and W. Bowie, The effect of topography and isostatic compensation upon the intensity of gravity, U.S. Coast and Geod. Surv., spec. pub. 10, 1912.

Heestand, R. L., and S. T. Crough, The effect of hotspots on oceanic depth-age relation, J. Geophys. Res., 86, 6107-6114, 1981.

Heirtzler, J. R., G. O. Dickson, E. M. Herron, W. C. Pitman, and X. LePichon, Marine magnetic anomalies, geomagnetic field reversals and motions of the ocean floor and continents, J. Geophys. Res., 73, 2119-2136, 1968.

Heiskanen, W. A., Investigations on the gravity formula, Publ. Isost. Inst., Int. Ass. Geod., No. 1, Helsinki, 1938.

Heiskanen, W. A., and F. A. Vening Meinesz, The earth and its gravity field, Mc-Graw Hill, New York, 1958.

Hess, H. H., History of the ocean basins, in Petrologic Studies: Buddington Memorial Volume, 599-620, Geol. Soc. Amer., 1962.

Isacks, B., J. Oliver, and L. R. Sykes, Seismology and the new global tectonics, J. Geophys. Res., 73, 5855-5899, 1968.

Jacobsen, S. B., and G. J. Wasserburg, A two-reservoir recycling model for mantle-crust evolution, Proc. Natl. Acad. Sci. U.S.A., 77, 6298-6302, 1980.

Jarvis, G. T., and W. R. Peltier, Lateral heterogeneity in the convecting mantle, J. Geophys. Res., 91, 435-451, 1986.

Jordan, T. H., Lithosphere slab penetration into the lower mantle beneath the Sea of Okhotsk, J. Geophys. Res., 82, 473-496, 1977.

Jordan, T. H., The deep structure of the continents, Scientific American, 240, 92-107, 1979.

Kaula, W. M., Earth's gravity field: relation to global tectonics, Science, 169, 982-984, 1970.

Kenyon, P. M., and D. L. Turcotte, Convection in a two-layer with strongly temperature dependent viscosity, J. Geophys. Res., 88, 6403-6414, 1983.

Lambert, W. D., The reduction of observed values of gravity to sea level, Bull. Geod., 26, 107-181, 1930.

Lambert, W. D., and W. F. Darling, Tables for determining the form of the geoid and its indirect effect on gravity, U.S. Coast and Geod. Surv., Spec. Pub., 199, 1936.

Langseth, M. G., X. LePichon and M. Ewing, Crustal structure of the mid-ocean ridges, 5. Heat flow through the Atlantic Ocean floor and convection currents, J. Geophys. Res., 71, 5321-5355, 1966.

Larson, R. L., W. C. Pitman, X. Golovchenko, S. C. Cande, J. F. Dewey, W. F. Haxby, and J. L. LaBrecque, The bedrock geology of the world, W. H. Freeman, New York, New York, 1985.

LePichon, X., Sea-floor spreading and continental drift, J. Geophys. Res., 73, 3661-3697, 1968.

Lister, C. R. B., Geoid anomalies over cooling lithosphere: source for a third kernel of upper mantle thermal parameters and thus an inversion, Geophys. J. Roy. Astr. Soc., 68, 219-240, 1982.

Masters, G., T. H. Jordan, P. G. Silver, and F. Gilbert, Aspherical earth structure from fundamental spheroidal-mode data, Nature, 298, 609-613, 1982.

McKenzie, D. P., Some remarks on heat flow and gravity anomalies, J. Geophys. Res., 72, 6261-6273, 1967.

McKenzie, D. P., Speculations on the consequences and causes of plate motions, Geophys. J. Roy. Astr. Soc., 18, 1-32, 1969.

McKenzie, D. P., Surface deformation, gravity anomalies and
convection, Geophys. J. Roy. Astr. Soc., 48, 211-238, 1977.

McKenzie, D. P., J. M. Roberts, and N. O. Weiss, Convection in the
earth's mantle: Towards a numerical simulation, J. Fluid
Mech., 62, 465-538, 1974.

Morgan, W. J., Gravity anomalies and convection currents, 1. A sphere
and cylinder sinking beneath the surface of viscous fluid, J.
Geophys. Res., 70, 6175-6187, 1965a.

Morgan, W. J., Gravity anomalies and convection currents, 2. The
Puerto Rico trench and the Mid-Atlantic rise, J. Geophys.
Res., 70, 6189-6204, 1965b.

Nakanishi, I., and D. L. Anderson, Measurements of mantle wave
velocities and inversion of lateral heterogeneities and
anisotropy. 1. Analysis of great circle phase velocities, J.
Geophys. Res., 88, 10267-10283, 1983.

Nakanishi, I., and D. L. Anderson, Aspherical heterogeneity of the
mantle from phase velocities of mantle waves, Nature, 307,
117-121, 1984.

Nataf, H., I. Nakanishi, and D. L. Anderson, Anisotropy and shear-
velocity heterogeneities in the upper mantle, Geophys. Res.
Lett., 11, 109-112, 1984.

Ockendon, J. R., and D. L. Turcotte, On the gravitational potential
and field anomalies due to thin mass layers, Geophys. J. Roy.
Astron. Soc., 48, 479-492, 1977.

Oliver, J. and B. Isacks, Deep earthquake zones, anomalous structures in the upper mantle, and the lithosphere, J. Geophys. Res., 72, 4259-4275, 1967.

Oxburgh, E. R. and D. L. Turcotte, Mid-ocean ridges and geotherm distribution during mantle convection, J. Geophys. Res., 73, 2643-2661, 1966.

Parker, R. L., and D. W. Oldenburg, Thermal model of ocean ridges, Nature, Phys. Sci., 242, 137-139, 1973.

Parsons, B., and J. G. Sclater, An analysis of the variation of ocean floor bathymetry and heat flow with age, J. Geophys. Res., 82, 803-827, 1977.

Parsons, B., and D. McKenzie, Mantle convection and the thermal structures of the plates, J. Geophys. Res., 83, 4485-4496, 1978.

Parsons, B., and S. Daly, The relationship between surface topography, gravity anomalies, and the temperature structure of convection, J. Geophys. Res., 88, 1129-1144, 1983.

Pekeris, C. L., Thermal convection in the interior of the earth, Mon. Not. R. Astron. Soc., Geophys. Suppl., 3, 343-367, 1935.

Peltier, W. R., Mantle convection and viscoelasticity, Annu. Rev. Fluid Mech., 17, 561-608, 1985.

Pratt, J. H., On the attraction of the Himalaya Mountains and of elevated regions beyond them, upon the plumb-line in India, Phil. Trans. Roy. Soc. Lond., 145, 53-100, 1855.

Pratt, J. H., On the deflection of the plumb-line in India, caused by the attraction of the Himmalaya Mountains and the elevated regions beyond; and its modifications by the compensating

effect of a deficiency of matter below the mountain mass, Phil. Trans. Roy. Soc. Lond., 149, 745-778, 1859a.

Pratt, J. H., On the influence of the ocean on the plumb-line in India, Phil. Trans. Roy. Soc. Lond., 149, 779-796, 1859b.

Rapp, R. H., GEOS-3 data processing for the recovery of geoid undulations and gravity anomalies, J. Geophys. Res., 84, 3784-3792, 1979a.

Rapp, R. H., Global anomaly and undulation recovery using GEOS-3 altimetric data, Dept. of Geod. Sci. Rep. No. 285, Ohio State Univ., Columbus, Ohio, 1979b.

Renkin, M., and J. G. Sclater, Age, depth and residual depth anomalies in the North Pacific: Implications for thermal models of the lithosphere and upper mantle, in press, 1986.

Ricard, Y., L. Fleitout, and C. Froidevaux, Geoid heights and lithospheric stresses for a dynamical earth, Ann. Geophys., 2, 267-286, 1984.

Richards, M. A., and B. H. Hager, Geoid anomalies in a dynamic earth, J. Geophys. Res., 89, 5987-6002, 1984.

Richardson, S. H., J. J. Gurney, A. J. Erlank, and J. W. Harris, Origin of diamonds in old enriched mantle, Nature, 310, 198-202, 1984.

Richter, F. M., Dynamical models of sea floor spreading, Rev. Geophys. Space Phys., 11, 223-287, 1973.

Richter, F. M., Mantle convection models, Ann. Rev. Earth Planet. Sci., 6, 9-19, 1978.

Richter, F. M., and B. Parsons, On the interactions of two scales of convection in the mantle, J. Geophys. Res., 80, 2529-2541, 1975.

Richter, F. M., and D. P. McKenzie, On some consequences and possible causes of layered convection, J. Geophys. Res, 86, 6133-6142, 1981.

Ringwood, A. E., Composition and petrology of the earth's mantle, McGraw Hill, New York, 1975.

Runcorn, S. K., Satellite gravity measurements and a laminar viscous flow model of the earth's mantle, J. Geophys. Res., 69, 4389-4394, 1964.

Runcorn, S. K., Flow in the mantle inferred from the low degree harmonics of the geopotential, Geophys. J. Roy. Astr. Soc., 14, 375-384, 1967.

Sandwell, D., and G. Schubert, Geoid height versus age for symmetric spreading ridges, J. Geophys. Res., 85, 7235-7241, 1980.

Schubert, G., C. Froidevaux, and D. A. Yuen, Oceanic lithosphere and asthenosphere: Thermal and mechanical structure, J. Geophys. Res., 81, 3525-3540, 1976.

Schubert, G., D. A. Yuen, C. Froidevaux, L. Fleitout, and M. Souriau, Mantle circulation with partial shallow return flow: Effects on stresses in oceanic plates and topography of the sea floor, J. Geophys. Res., 83, 745-758, 1978.

Sclater, J. G., and J. Francheteau, The implications of terrestrial heat flow observations on current tectonics and geochemical

models of the crust and upper mantle of earth, Geophys. J. R. Astron. Soc., 20, 509-542, 1970.

Sclater, J. G., R. N. Anderson, and M. L. Bell, Elevation of ridges and evolution of the central Eastern Pacific, J. Geophys. Res., 76, 7888-7915, 1971.

Sclater, J. G., C. Jupart, and D. Galson, The heat flow through oceanic and continental crust and the heat loss of the earth,Rev. Geophys. Space Phys., 18, 269-311, 1980.

Sclater, J. G., L. A. Lawver, and B. Parsons, Comparisons of long wavelength residual elevation and free air gravity anomalies in the North Atlantic and possible implications for the thickness of the lithospheric plate, J. Geophys. Res., 80, 1031-1052, 1975.

Smith, S. M., H. W. Menard, and G. Sharman, World-wide ocean depths and continental elevations averaged for areas approximately one degree squares of latitude and longitude, SIO reference 65-8, Scripps Inst. of Oceanography, Univ. California, 1966.

Stokes, G. G., On the variation of gravity and the surface of the earth, Trans. Camb. Phil. Soc., 8, 672-695, 1849.

Sykes, L. R., The seismicity and deep structure of island arcs, J. Geophys. Res., 71, 2981-3006, 1966.

Sykes, L. R., Mechanism of earthquakes and nature of faulting on the mid-ocean ridges, J. Geophys. Res., 72, 2131-2153, 1967.

Turcotte, D. L., and D. C. McAdoo, Geoid anomalies and the thickness of the lithosphere, J. Geophys. Res., 84, 2381-2387, 1979.

Vening Meinesz, F. A., The indirect isostatic or Bowie reduction and the equilibrium figure of the earth, Bull. Geodesique, N. Ser., 1, 33-107, 1946.

Vine, F. J., Spreading of the ocean floor: New evidence, Science, 154, 1405-1415, 1966.

Vine, F. J., and D. H. Matthews, Magnetic anomalies over oceanic ridges, Nature, 199, 947-949, 1963.

Watts, A. B., D. P. McKenzie, B. E. Parsons, and M. Roufosse, The relationship between gravity and bathymetry in the Pacific Ocean, Geophys. J. Roy. Astron. Soc., 83, 263-298, 1985.

Wilson, J. T., A new class of faults and their bearing on continental drift, Nature, 207, 343-347, 1965.

Woodhouse, J. H., and A. M. Dziewonski, Mapping the upper mantle: Three dimensional modeling of earth structure by inversion of seismic waveform, J. Geophys. Res., 89, 5953-5986, 1984.

APPENDIX A - ROMBERG'S METHOD

We briefly review here a method proposed by Romberg (Bauer et al., 1963) to evaluate definite integrals. We define $T_{0,j}$ as the estimate for the integral

$$y = \int_a^b f(x)dx$$

computed by using the trapezoidal rule

$$T_{0,j} = u_j \left[\frac{1}{2}f(a) + \frac{1}{2}f(b) + \sum_{i=1}^{n-1} f(a + iu_j) \right]$$

where $n = 2^j$, $u_j = (b-a)/n$ and the full interval is divided into $j = 1, 2, 4, 8, \ldots$ equal parts. Then we can write

$$T_{0,j} = y + \sum_{r=1}^{\infty} C_{0,2r} \cdot u_j^{2r}$$

where the $C_{0,2r}$ are unknown coeficients which do not depend on j.

Thus, there is a truncation error of the order u_j^2.

Romberg arranged successive approximations $T_{i,j}$ in a triangular array

$$T_{0,0}$$

$$T_{0,1} \quad T_{1,0}$$

$$T_{0,2} \quad T_{1,1} \quad T_{2,0}$$

$$T_{0,3} \quad T_{1,2} \quad T_{2,1} \quad T_{3,0}$$

(A.1)

$$
\begin{array}{ccccccc}
\cdot & \cdot & \cdot & \cdot & \cdot & & \\
\cdot & \cdot & \cdot & \cdot & \cdot & \cdot & \\
\cdot & \cdot & \cdot & \cdot & \cdot & \cdot & \cdot \\
\end{array}
$$

$$T_{0,j} \quad T_{1,j-1} \quad T_{2,j-2} \quad \cdot \quad \cdot \quad \cdot \quad T_{j,0}$$

where every entry $T_{N,j}$ $(N \neq 0)$ is computed using the general extrapolation equation

$$T_{N,j} = T_{N-1,j+1} + \frac{T_{N-1,j+1} - T_{N-1,j}}{2^{2N} - 1} . \qquad (A.2)$$

The value $T_{N,j}$ is calculated using the values in the following positions relative to it

$$T_{N-1,j}$$

$$T_{N-1,j+1} \longrightarrow T_{N,j}$$

Taking N=1 we get a better approximation to y because

$$T_{1,j} = y + \frac{1}{2^2 - 1} \sum_{r=1}^{\infty} C_{0,2r} (2^2 u_{j+1}^{2r} - u_j^{2r}) .$$

Noting that $2^2 u_{j+1}^2 - u_j^2 = 0$ and setting

$$C_{1,2r} = \frac{1}{2^2 - 1} (2^2 - 2^{2r}) \cdot C_{0,2r} ,$$

and $T_{1,j}$ becomes

$$T_{1,j} = y + \sum_{r=2}^{\infty} C_{1,2r} \cdot u_{j+1}^{2r} .$$

This gives a truncation error of the order u_{j+1}^4. Since $T_{0,j+2}$ is also

known, $T_{1,j+1}$ and $T_{2,j}$ can be generated using Equation A.2. The value

$T_{2,j}$ is

$$T_{2,j} = T_{1,j+1} + \frac{T_{1,j+1} - T_{1,j}}{2^4 - 1} .$$

Thus

$$T_{2,j} = y + \sum_{r=3}^{\infty} C_{2,2r} \cdot u_{j+2}^{2r}$$

with

$$C_{2,2r} = \frac{1}{2^4 - 1} (2^4 - 2^{2r}) \cdot C_{1,2r}$$

with a truncation error of the order u_{j+2}^6. The order of the truncation

error increases by 2 at each new extrapolation step, so that we can

continue the process and minimize the associated error until it is

smaller than any given value.

The values in each line of Table A.1, i.e.

$$T_{0,j}, \ T_{1,j-1}, \ T_{2,j-2}, \ \ldots, \ T_{j-1,1}, \ T_{j,0}$$

are obtained from the same subdivision of the full interval, which is equal to 2^j parts. Romberg showed that the sequence $T_{N,j}$ (j=1,2,3...) converges to the true integral for increasing N. In addition, the sequence $T_{0,j}$ converges to the true integral for increasing j. The calculation of the values, $T_{N,j}$, is continued until the difference between two successive values is less than a given tolerance; the absolute value of this difference is an upper bound on the error.

APPENDIX B - THE AGE AT THE CENTROID OF A TRAPEZOID

A spherical trapezoid may be approximated by a planar trapezoid

(see Figure B.1). The area A of the trapezoid OPQS is

$$A = \frac{(a + b)h}{2}$$

where

$$a = \frac{\pi R \sin\left[\frac{\pi(j-1)}{18}\right]}{18}$$

$$b = \frac{\pi R \sin\left[\frac{\pi j}{18}\right]}{18}$$

$$h = \frac{\pi R}{18}$$

and j is the ring number, j=1,2,3...18. Due to symmetry it is obvious

Figure B.1 Geometry of a spherical trapezoid.
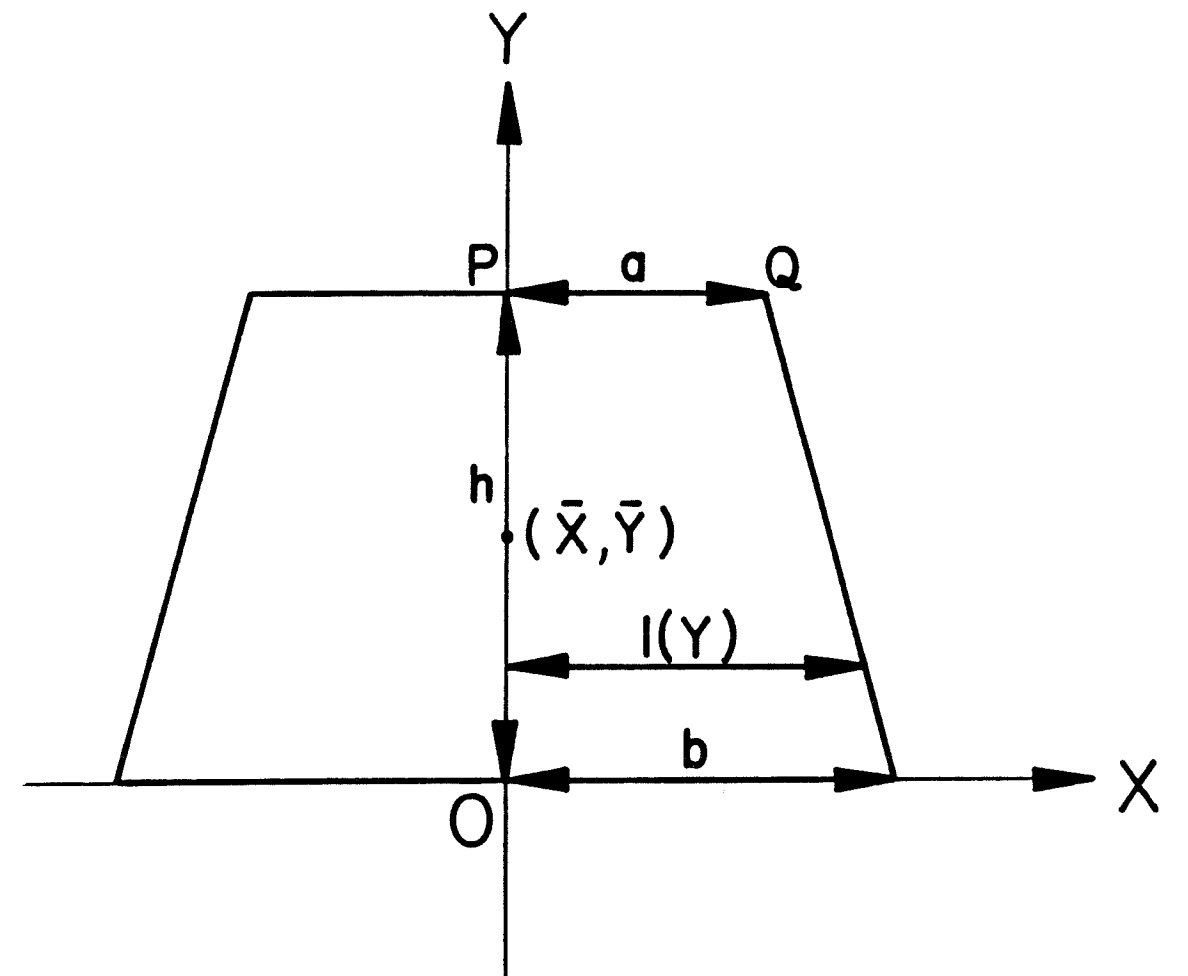
that the $\bar{x}$ axis of the center of mass is $\bar{x}=0$. The width opposite a point, y, is

$$l(y) = (b - a) - \frac{b - a}{h}y + a = b - \frac{b - a}{h}y \; ;$$

if y=0 then l(0)=b, whereas if y=h then l(h)=a. The y axis of the center of mass, $\bar{y}$, is

$$\bar{y} = \frac{1}{A} \int_0^h yl(y) \, dy = \frac{1}{A} \int_0^h y(b - \frac{b - a}{h}y) \, dy = \frac{h(2a + b)}{3(a + b)}$$

If a=0 then $\bar{y}$ = h/3; this is the case for a spherical triangle (rings 1 and 18). Close to the equator one gets (a,b)—>h, so that $A=h^2$ and $\bar{y}=h/2$.

The distance, u, from the observation point to the centroid of a given trapezoid on a ring, j, is

$$u = \frac{\pi j}{18} - \bar{y} \qquad , 1 \leq j \leq 9$$

for the northern hemisphere, and

$$u = \frac{\pi j}{18} + \bar{y} \qquad , 10 \leq j \leq 18$$

for the southern hemisphere.

Figure B.2 illustrates a spherical triangle where N is the north pole of the test planet, P is the observation point, and Q is the centroid of a given trapezoid. The sides of the triangle a, b and u, and the different angles are expressed using angular units. The coordinates of point P are known. We start increasing the angle α, moving clockwise from the point closest to the north pole on the meridian of the observation point. The angle increment is 10° each time. The side of the triangle a is obtained by using the law of cosines

$$\cos a = \cos b \cos u + \sin b \sin u \cos \alpha .$$

The relationship between two angles and three sides is

$$\sin u \cos \alpha = \cos a \sin b - \cos b \sin a \cos \zeta ,$$

and ζ is

$$\zeta = \cos^{-1} \left\{ \frac{\cos a \sin b - \sin u \cos \alpha}{\cos b \sin a} \right\} .$$

Figure B.2 Geometry of a spherical triangle. N - North pole, P - Observation Point, Q - Centroid of a given spherical triangle or trapezoid, O - Center of the planet, r - radius vector.
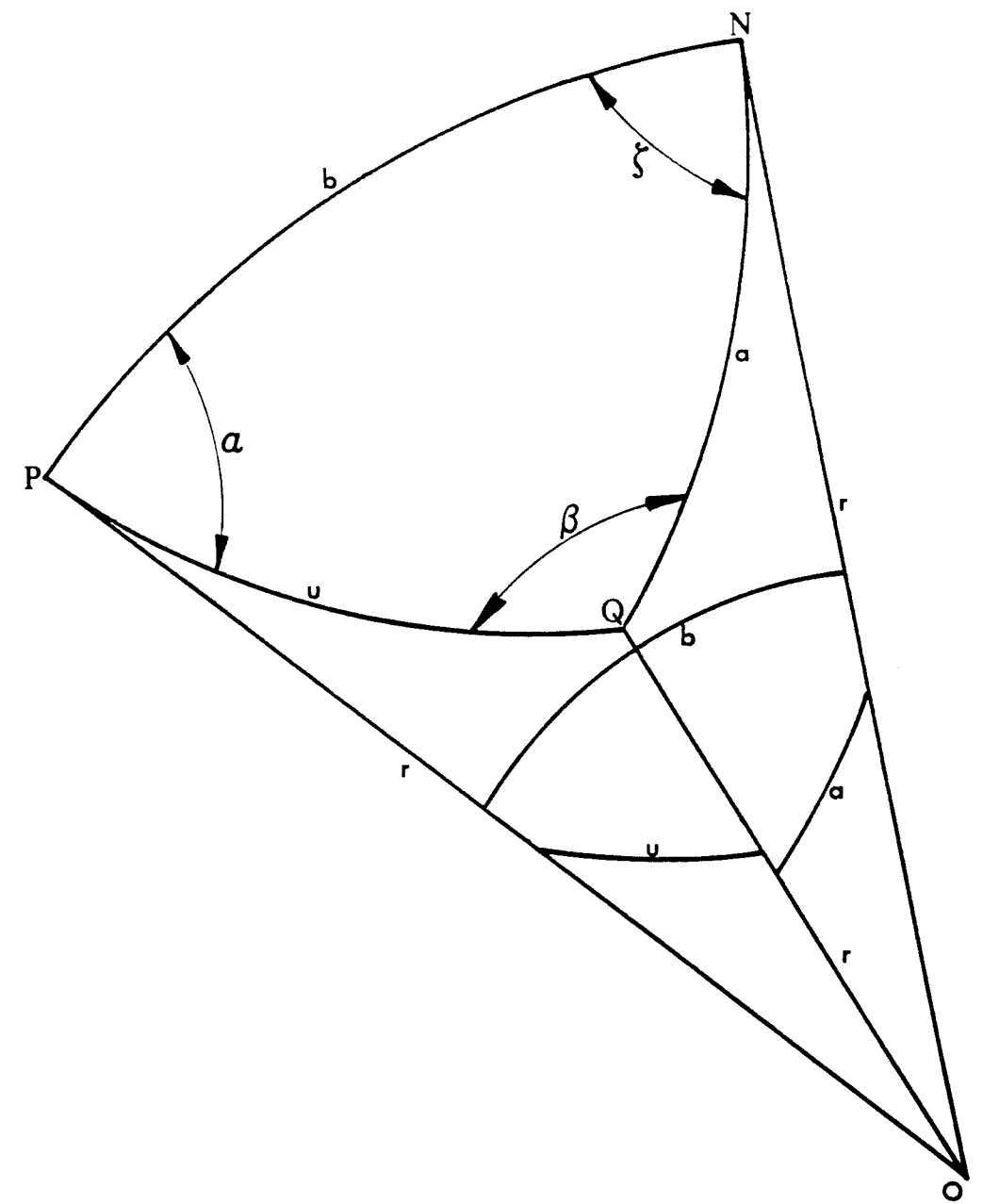
We find that the longitude angle at point Q, ϕ_Q, is

$$\phi_Q = \phi_P - \zeta \qquad\qquad , 0 \leq \alpha \leq \pi$$

or

$$\phi_Q = \phi_P + \zeta \qquad\qquad , \pi \leq \alpha \leq 2\pi \ .$$

The age, t, is

$$t = \frac{\phi_Q}{\omega}$$

where ω is the angular velocity of the sea-floor spreading on this hypothetical test planet.

APPENDIX C - THE SOLUTION OF THE FINAL EQUATIONS OF THE MODEL

The final equations that give the anomalies over the geoid and the reference surface, due to the initial and self-deformation effects, are

$$(s + s')\Gamma^{ss} + (r + r')\Gamma^{rs} = s' \qquad (C.1)$$

for the geoid, and

$$(s + s')\Gamma^{sr} + (r + r')\Gamma^{rr} = r' \qquad (C.2)$$

for the reference surface (see Equations 20 and 21).

We extract s' from Equation C.1

$$s\Gamma^{ss} + s'\Gamma^{ss} + (r + r')\Gamma^{rs} = s'$$

leads to

$$s\Gamma^{ss}(1 - \Gamma^{ss})^{-1} + (r + r')\Gamma^{rs}(1 - \Gamma^{ss})^{-1} = s'$$

or

$$s' = sQ + (r + r')P \qquad \text{(C.3)}$$

where $Q=\Gamma^{ss}(1-\Gamma^{ss})^{-1}$ and $P=\Gamma^{rs}(1-\Gamma^{ss})^{-1}$. Substitution of the above equation in Equation C.2 yields

$$r' = s\Gamma^{sr} + sA + (r + r')(B + \Gamma^{rr})$$

where $A=Q\Gamma^{sr}$ and $B=P\Gamma^{sr}$. Extracting r' from the right side of the above equation gives

$$r' = sD + rC + r'C$$

whence

$$r' = sD(1 - C)^{-1} + rC(1 - C)^{-1}$$

where $C=B+\Gamma^{rr}$ and $D=A+\Gamma^{sr}$ and r' is given by

$$r' = sE + rF \qquad \text{(C.4)}$$

where $E=D(1-C)^{-1}$ and $F=C(1-C)^{-1}$. The computer program calculates r' using Equation C.4 and then it substitutes r' into Equation C.3 to calculate s'.

APPENDIX D - SOLUTION OF THE ISOSTATIC EQUATION

The isostatic equation, using a combination of Airy's and Pratt's model and the oceanic ridge as a reference, as defined above is (see Figure 27 and Equation 22)

$$\rho_c d + I_0 = C \qquad\qquad (D.1)$$

where C is a constant, I_0 is the contribution of the mantle under the continent, d is continental thickness and ρ_c is continental density.

The thermal gradient in the continent is 20 °c/km until we reach a temperature of 900 °c at depth of 45 km, and hereafter the thermal gradient is adjusted so we get 1400 °c at the reference surface. If the continental thickness is less than 45 km we adjust the thermal gradient for the upper mantle only. Besides the above mentioned cases of crustal thickness less or larger then 45 km, two more will be discussed below which are 1) ice over the continent, i.e. Antarctica, and 2) shallow sea over the continent, i.e. Hudson bay or Baltic sea.

D.1 - Thickness of the continent is less than 45 km

Figure 31 illustrates the model. The temperature in the mantle under the continent (measuring from the mean sea level) is

$$T_m(z) = dA + (z - d + y)B = d(A - B) + Bz + By$$

where A is the thermal gradient in the continent, B is the thermal gradient in the mantle under the continent

$$B = \frac{T_1 - Ad}{\beta + y - d} \qquad (D.2)$$

where β is the distance from mean sea level to the reference surface, 202.5 km, y is the continental height, and T_1 is the temperature at the reference surface.

The density at any point in the mantle is

$$\rho = \rho_1(1 + \alpha\Delta T) = \rho_1 + \rho_1\alpha[T_1 - T_m(z)]$$

$$= \rho_1 + \rho_1\alpha T_1 - \rho_1\alpha(A - B)d - \rho_1\alpha Bz - \rho_1\alpha yB$$

$$= D - E(A - B)d - EBz - EyB$$

here ρ_0 is the reference surface density under the continent, $E=\rho_1\alpha$, and $D=\rho_1+\rho_1\alpha T_1$.

The contribution of the mantle under the continent is

$$I_0 = \int_{d_1}^{\beta} \rho \; dz = \int_{d_1}^{\beta} \left[D - E(A - B)d - EBz - EyB \right]dz$$

where $d_1=d-y$. The above integral is a simple one and after some algebra we find that I_0 is

$$I_0 = F - dG + BdH + EAd^2 - Bd^2\frac{E}{2} + BJ$$

where

$$F = D\beta + Dy \qquad ,$$

$$G = D + EA\beta + EAy \qquad ,$$

$$H = E(\beta + y) \qquad ,$$

and

$$J = \frac{-E(\beta + y)^2}{2} \qquad .$$

Substitution of I_0 in the isostatic equation (Equation D.1) yields

$$C = \rho_c d + F - dG + BdH + EAd^2 - \frac{EBd^2}{2} + BJ \qquad .$$

Substitution of B (Equation D.2) in the above equation yields

$$N + dP + Qd^2 - \frac{Md^3}{2} = 0 \qquad\qquad (D.3)$$

where

$$N = K(\beta + y) + JT_1 \qquad ,$$

$$P = \left[L(\beta + y) - K + HT_1 - JA \right] \qquad ,$$

$$Q = M(\beta + y) - L - HA - \frac{ET_1}{2}$$

where $K = F - C$, $L = \rho_c - G$, and $M = EA$. We get three solutions of which two are complex and only one is real. The real solution is later used for the computations of the dipole and mass effects.

D.2 - Thickness of the continent is larger than 45 km

Figure 31 illustrates the model. The temperature in the mantle under the continent is (measuring from mean sea level)

$$T_m(z) = T_c + B(z + y + u) = D + Bz$$

where $u=45 \times 10^3$ m, $T_c=900$ °c, y is topographic height, β is the distance from the mean sea level to reference surface, 202.5×10^3 m, and B is the thermal gradient in the mantle under the continent

$$B = \frac{1400 - T_c}{\beta + y - u} = \frac{500}{\beta + y - u} \quad ,$$

and

$$D = T_c + B(y - u).$$

The density at any point in the mantle under the continent is

$$\rho = \rho_1 (1 + \alpha \Delta T)$$

$$= \rho_1 + \rho_1 \alpha \left[T_1 - T_m(z) \right]$$

$$= E - FD - FBz = G - Hz$$

where ρ is the reference surface density under the continent, $F = \rho_1 \alpha$,

$$E = \rho_1 (1 + \alpha T_1) \quad ,$$

$$G = E - FD \quad ,$$

and $H = FB$.

The contribution of the mantle under the continent is

$$I_0 = \int_{d_1}^{\beta} \rho \, dz = \int_{d_1}^{\beta} (G - Hz) dz$$

and after some algebra we get

$$= J + Kd + Ld^2$$

where

$$J = G(\beta + y) + \frac{H(y^2 + \beta^2)}{2} \quad ,$$

$$K = -G - Hy \quad ,$$

and L=H/2.

Substitution of I_0 in the isostatic equation (Equation D.1) yields

$$0 = J - C + (K + \rho_c)d + Ld^2 \quad ,$$

and we choose the positive solution as our solution.

D.3 - Ice over the continent

Two regions belong to this category which are Antarctica and Greenland with uniform ice cover of 2.5 km and 1.3 km, respectively. This case is similar to case I because the density of ice is 900 kg/m^3 and the maximum topographic height is less than 3500 m, which implies that the thickness of the continent is less than 45 km. Figure 32 illustrates the model. The Equation of Isostasy is

$$\rho_i y + \rho_c d + I_0 = C \qquad (D.4)$$

where ρ_i is ice density 900 kg/m^3, y is thickness of ice layer, ρ_c is crustal density 2800 kg/m^3, and d is crustal thickness. The temperature in the mantle under the continent is

$$T_m(z) = Ad + [z - (d + y - f)]B = Ad + Bz - Bd + B(f - y) \qquad (D.5)$$

where z is measured from mean sea level, A is the geothermal gradient in the continental crust 20 °c/km, and B is the geothermal gradient in the mantle under the continent

$$B = \frac{T_1 - Ad}{\beta + f - d - y} = \frac{T_1 - Ad}{u - d} \qquad (D.6)$$

where β is the distance from mean sea level to reference surface, f is topographic height, and u=β+f-y. The density in the mantle under the continent is

$$\rho = \rho_1(1 + \alpha\Delta T) = \rho_1 + \rho_1\alpha T_1 - \rho_1\alpha T_m(z)$$

$$= D - Fd + EB(d - z) - GB \qquad (D.7)$$

where ρ_1 is the reference surface density under the continent, D=ρ_1+$\rho_1\alpha T_1$, E=$\rho_1\alpha$, F=EA, and G=E(f-y).

The contribution of the mantle under the continent is

$$I_0 = \int_v^\beta \rho \, dz = \int_v^\beta (D - Fd - EBz + EBd - GB)dz$$

$$= \left[D - Fd + EBd - GB\right](\beta - v) + EB\left[\frac{v^2 - \beta^2}{2}\right] \qquad (D.8)$$

where v=d+y-f. Substitution of Equation D.8 in the Isostatic Equation (D.4) yields

$$C = \rho_i y + \rho_c d + I_o$$

$$= \rho_i y + \rho_c d + [D - Fd - GB](\beta - v) + EB\left[\frac{v^2 - \beta^2}{2}\right] \quad ,$$

or

$$0 = H + dJ + Fd^2 + BK + BdL - \frac{EBd^2}{2} \tag{D.9}$$

where

$$H = \rho_i y - C + D\beta - D(y - f) \quad ,$$

$$J = \rho_c - D - F\beta + F(y - f) \quad ,$$

$$K = E\frac{(y - f)^2 - \beta^2}{2} + G(y - f - \beta) \quad ,$$

and

$$L = E\beta + G \quad .$$

Substitution of Equation D.6 in Equation D.9 gives

$$0 = M + Nd + Pd^2 + Qd^3 \qquad \text{(D.10)}$$

where

$$M = Hu + KT_1 \qquad ,$$

$$N = Ju - H - KA + LT_1 \qquad ,$$

$$P = Fu - J - LA - \frac{ET_1}{2} \qquad ,$$

and

$$Q = \frac{EA}{2} - F \qquad .$$

We get three solutions from Equation D.10 of which two are complex, and we choose the third which is real for later computations.

D.4 - Continent with shallow sea above

Several regions belong to this category, i.e. Hudson bay or Baltic sea. This case is similar to case I because we replace the part of the continental crust which is below mean sea level by seawater and the

topographic height is 0 m, so the thickness of the continent is less than 45 km. Figure 33 illustrates the model. The Equation of Isostasy is

$$\rho_w y + \rho_c d + I_0 = C \quad , \tag{D.11}$$

where ρ_w is seawater density 1030 kg/m³, y is depth of seawater (less than 2500 m), ρ_c is density of the crust 2800 kg/m³ and d is thickness of the continent. The temperature in the mantle under the continent is

$$T_m(z) = Ad + B(z - d - y) \quad , \tag{D.12}$$

where A is the geothermal gradient in the continent 20 °c/km, z is measured from the mean sea level, and B is

$$B = \frac{T_1 - Ad}{\beta - y - d} \tag{D.13}$$

where β is the distance from mean sea level to reference surface. The density of the mantle under the continent is

$$\rho = \rho_1(1 + \alpha\Delta T) = \rho_1\left[1 + \alpha\Delta T_0 - \alpha\Delta T_m(z)\right]$$

$$= \rho_1 + E - DB(z - y) - Dd(A - B) \tag{D.14}$$

where ρ is the reference surface density under the continent, $D=\rho_1\alpha$, and $E=DT_1$. The contribution of the mantle under the continent is, using Equation D.14

$$I_0 = \int_{d+y}^{\beta} \left[\rho_1 + E - DB(z - y) - Dd(A - B)\right]dz$$

$$= F + dG + BH + d^2J + dBK - \frac{DBd^2}{2} \qquad (D.15)$$

where $J=DA$, $K=D(\beta - y)$,

$$F = E(\beta - y) + \rho_0(\beta - y) \qquad ,$$

$$G = - E - DA(\beta - y) - \rho_0 \qquad ,$$

$$H = Dy(\beta - y) + D\frac{y^2 + \beta^2}{2} \qquad .$$

Substitution of Equation D.15 in Equation D.11 (Equation of Isostasy) yields

$$C = \rho_w y + \rho_\psi \phi + I_0$$

$$= \rho_w y + \rho_c d + F + dG + BH + d^2J + dBK - \frac{DBd^2}{2} \qquad ,$$

and using Equation D.13

$$0 = N + Pd + Qd^2 + Rd^3 \qquad\qquad (D.16)$$

where

$$N = L(\beta - y) + HT_1 \qquad ,$$

$$P = M(\beta - y) + KT_1 - HA - L \qquad ,$$

$$Q = J(\beta - y) - M - KA - \frac{DT_1}{2} \qquad ,$$

$$R = \frac{DA}{2} - J \qquad ,$$

$$L = F + \rho_w y - C \qquad ,$$

and $M = G + \rho_c$. We get three solutions of which two are complex and only one is real. The real solution is later used for the computations of the dipole and mass effects.

APPENDIX E - THE DISTRIBUTION OF THE DIPOLE OVER THE EARTH

Figure 46 illustrates the geometry. The distance u is

$$u = \left[(x_1 - x_0)^2 + (y_1 - y_0)^2 + (z_1 - z_0)^2 \right]^{1/2}$$

where the coordinates of the observation and measuring points are

$$x_1 = R \sin \Theta_1 \cos \Phi_1$$

$$y_1 = R \sin \Theta_1 \sin \Phi_1$$

$$z_1 = R \cos R_1$$

$$x_0 = (R - z) \sin \Theta_0 \cos \Phi_0$$

$$y_0 = (R - z) \sin \Theta_0 \sin \Phi_0$$

$$z_0 = (R - z) \cos \Theta_0$$

respectively. A surface element, dA, is

$$dA = (R - z)^2 \sin \Theta \, d\Theta \, d\Phi$$

and the observed geoid due to this element is

$$dY = \frac{Gmh \, dA}{u^3} = \frac{Gmh(R - z)^2 \sin \Theta \, d\Theta \, d\Phi}{u^3}$$

where h is the height of the observation point above the dipole equatorial plane.

Using the cosine theorem we obtain the angle α', which is the smallest angle between u and the dipole equatorial plane

$$R^2 = (R - z)^2 + u^2 - 2(R - z)u \cos \alpha \implies$$

$$\alpha = \arccos \left\{ \frac{(R - z)^2 + u^2 - R^2}{2(R - z)u} \right\}$$

so $\alpha' = \alpha - 90°$ and $h = \sin \alpha'$.

The observed geoid anomaly is

$$Y = \frac{G}{g} \int_{z'}^{z''} \int_{\Theta'}^{\Theta''} \int_{\Phi'}^{\Phi''} \frac{mh(R - z)^2 \sin \Theta \, d\Theta \, d\Phi \, dz}{u^3}$$

$$= \frac{G}{g} \int_{z'}^{z''} \int_{\Theta'}^{\Theta''} \int_{\Phi'}^{\Phi''} \frac{m(R - z)^2 \sin \alpha' \sin \Theta \, d\Theta \, d\Phi \, dz}{u^2} .$$

Birth Date: 8/4/53

Birth Place: Kfar-Saba, Israel

Maritual Status: Married + 2 children

Education:

B.Sc., Physics, Tel-Aviv University, 1978.

M.Sc., Geophysics, University of Washington, 1984.

Ph.D., Geophysics, University of Washington, 1986.